Direct Numerical Simulation of Wall-Bounded Compressible Turbulent Flow

by

Shinji Tamano

A Dissertation
Submitted to
Nagoya Institute of Technology
in Partial Fulfillment of the
Requirements for the Degree of
Doctor of Engineering

Department of Mechanical Engineering
Nagoya Institute of Technology
JAPAN

January 2002

Abstract

The purpose of the present study is to investigate the detailed mechanism of the wall-bounded compressible turbulent flow. In particular, the wall-bounded flow with an adiabatic wall is not still understood in spite of its engineering importance. To clarify the flow near the adiabatic wall and the difference between those near isothermal and adiabatic walls for the compressible turbulent flow, the compressible turbulent channel flow between adiabatic and isothermal walls is investigated. This flow can be a very useful framework for the present objective, since it is the simplest turbulent channel flow with an adiabatic wall and provides ideal information for modeling the compressible turbulent flow near the adiabatic wall. Note that the mean flow in the compressible channel flow between adiabatic walls does not approach a stationary state if there is no artificial heat sink.

A new Direct Numerical Simulation (DNS) algorithm based on B-spline collocation method is proposed to perform the DNS of the compressible turbulent channel flow between adiabatic and isothermal walls, since it is difficult to simulate the flow accurately and efficiently using the existing DNS algorithm for the wall-bounded compressible turbulent flow. The reliability of the present DNS algorithm is confirmed by comparing our result with that of Coleman *et al.* (1995) for the compressible turbulent channel flow between isothermal walls.

The DNS of the compressible turbulent channel flow between adiabatic and isothermal walls is stably performed by using the constructed DNS algorithm, and then the first DNS data of this flow is obtained. This is the novel result of the present study. Mean profiles, turbulence statistics and energy transfers are investigated by using the present DNS results.

To compare compressible and incompressible turbulent channel flows, the DNS of the incompressible turbulent channel flow with passive scalar transport between adiabatic and isothermal walls is also carried out. This flow is one of three specific situations between which Teitel & Antonia (1993) distinguished. The DNS of the incompressible turbulent flow between isothermal walls, which corresponds to that of Kim & Moin (1989), is performed for comparison.

The main results obtained in this study may be stated as follows. We propose the DNS algorithm which can simulate the turbulent channel flow between adiabatic and isothermal walls accurately and efficiently. The reliable results of this flow are firstly obtained by the present DNS. The mean velocity and temperature near adiabatic and isothermal walls for the compressible turbulent channel flow can be explained using the non-dimensional heat flux and the friction Mach number. Morkovin's hypothesis is not applicable to the near-wall asymptotic behavior of the wall-normal turbulence intensity even if the variable property effect is taken into account. Although the compressibility terms of the turbulent kinetic energy equation have slight contribution to the energy transfer, the dominant term of them transfers the turbulent kinetic energy to the mean flow near the isothermal wall and transfers the energy from the mean flow to the turbulent flow near the adiabatic wall. The pressure work which is dominant in the compressibility term of the mean kinetic energy equation exchanges the internal energy for mean kinetic energy near the isothermal wall and exchanges the mean kinetic energy for internal energy near the adiabatic wall. The thermodynamic dissipation term which is dominant in the compressible part of the turbulent energy dissipation is not negligible in the region very close to the isothermal wall. The near-wall streak structures of compressible and incompressible turbulent flows are comparable and are independent of the thermal wall boundary condition, when the variable property effect is taken into consideration. Morkovin's hypothesis is not applicable to the correlation coefficient between velocity and temperature fluctuations near the adiabatic wall.

Acknowledgements

This dissertation is a summary of the author's doctoral study in Nagoya Institute of Technology. At the end of this work, the author wishes to express his great appreciate to *Prof. Koichi Nakabayashi* for his kind instruction and guidance throughout the course of this study. The author has benefited a lot from his rich knowledge, the cute insight in science and technology, and the rigorous scientific approach on research.

The author wishes to express his sincere thanks and gratitude to the examining committee members, *Prof. Koichi Nakabayashi*, *Prof. Yasutaka Nagano* and *Prof. Motoyuki Ito*, for reading the dissertation carefully and making appropriate suggestions for improvement.

The author is grateful to *Associate Prof. Youhei Morinishi* for his direct help and valuable advice. As the associate advisor and cooperator, he provided great expertise in the domain of numerical simulation and theoretical analysis. His insight and advice have helped the author formulate the current work fluently.

Particular thanks go to the staff and graduate students of the Fluid Mechanics Laboratory at NIT for their support in many areas. Special thanks go to *Mr. Masaya Tanizawa*, *Mr. Takashi Okumura* and *Mr. Eisuke Nakamura* for their important help. The author would also like to thank *Dr. Shuiqiang Ren*, *Mr. Shigehiro Hashimoto*, *Mr. Hitoshi Sobue*, *Mr. Kazunari Kimura* and *Mr. Norikazu Okude* for their kind assistance.

The author would like to thank *Dr. G. N. Coleman* for providing the referenced data. The computations performed on a FUJITSU VPP300 at the Center for Promotion of Computational Science and Engineering, Japan Atomic Energy

Research Institute, are gratefully acknowledged.

Finally, the author would like to thank his family for their continuing encouragement.

Contents

List of Figures

List of Tables

Nomenclature

Roman Symbols

A	$A = B_q/[(\gamma - 1)M_\tau^2]$
a	Speed of sound; $a = (\gamma RT)^{1/2}$
AC	Acoustic Courant number; see (2.37)
B	Additive constant for log-law of mean velocity
$\mathbf{B}$	Matrix of B-spline
b_j	Expansion coefficient of B-spline for integration
B_j^k	j-th B-spline of k-th order
B_q	Non-dimensional heat flux; $B_q = q_w/(\rho_w c_p u_\tau T_w)$
C	Additive constant for log-law of mean temperature
C_k	Compressibility term of turbulent kinetic energy equation; $C_k = -C_{k1} + C_{k2} + C_{k3}$
C_K	Compressibility term of mean kinetic energy equation; $C_K = C_{k1} - C_{k2} + C_{K1}$
C_{k1}	$C_{k1} = \langle u_2'' \rangle \partial \langle p \rangle / \partial x_2$
C_{k2}	$C_{k2} = \langle u_i'' \rangle \partial \langle \tau_{i2} \rangle / \partial x_2$
C_1^n	Mass at time t_n
C_2^n	Momentum at time t_n

C_{k3}	Pressure-dilatation correlation term; $C_{k3} = \langle p' \partial u_k' / \partial x_k \rangle$
C_{K1}	Pressure work; $C_{K1} = \langle p \rangle \, \partial \langle u_2 \rangle / \partial x_2$
C_f	Skin friction coefficient; $C_f = 2\tau_w / (\rho_m U_m^2)$
c_p	Specific heat at constant pressure
c_v	Specific heat at constant volume
d	Dilatation; $d = \partial u_j / \partial x_j$
D	$D = (A^2 + E)^{1/2}$
D_e	Diffusion term of internal energy equation; $D_e = D_{e1} + D_{e2}$
D_{e1}	$D_{e1} = \partial \left(\langle \rho \rangle \, c_v \{u_2'' T''\} \right) / \partial x_2$
D_{e2}	$D_{e2} = \partial \langle q_2 \rangle / \partial x_2$
D_k	Diffusion term of turbulent kinetic equation; $D_k = \partial \left[\langle \tau_{i2}' u_i' \rangle - \langle \rho \rangle \{u_2'' k''\} - \langle p' u_2' \rangle \right] / \partial x_2$
D_K	Diffusion term of mean kinetic equation; $D_K = \partial \left[\langle \tau_{i2} \rangle \langle u_i \rangle - \langle \rho \rangle \{u_2'' K''\} - \langle p \rangle \langle u_2 \rangle \right] / \partial x_2$
E	$E = 2/[Pr_t M_\tau^2 (\gamma - 1)]$
$E_{\phi\phi}(k_1, x_2)$	1D streamwise energy spectrum; see (2.38)
$E_{\phi\phi}(k_3, x_2)$	1D spanwise energy spectrum; see (2.39)
f_i	Body force; $f_i = -\tau_{w_{av}} \delta_{i1} / (H \rho_m)$
F_K	Force term of mean kinetic energy equation; $F_K = \langle \rho \rangle \, f_1 \{u_1\}$
G	Criterion for Reynolds analogy; see (4.16)
H	Channel half-width
L_1, L_2, L_3	Computational region in the x_1, x_2 and x_3 directions, respectively
$\langle k \rangle$	Reynolds-averaged turbulent kinetic energy; $\langle k \rangle \equiv \langle u_i' u_i' \rangle / 2$

$\{k\}$	Favre-averaged turbulent kinetic energy; $\{k\} \equiv \{u_i'' u_i''\}/2$
$\{K\}$	Favre-averaged mean-flow kinetic energy $\{K\} \equiv \{u_i\}^2/2$
k''	Favre-fluctuation turbulent kinetic energy; $k'' \equiv u_i'' u_i''/2 - \{k\}$
K''	Favre-fluctuation mean-flow kinetic energy; $K'' \equiv \{u_i\} u_i''$
k_1, k_3	Modal indices in the x_1 and x_3 directions
M	Mach number based on bulk velocity and isothermal wall temperature; $M = U_m / \left(\gamma R T_{iw}\right)^{1/2}$
$\langle M \rangle$	Mach number based on bulk velocity and isothermal wall temperature; $\langle M \rangle = \langle u_1 \rangle / \left((\gamma - 1) c_p \langle T \rangle\right)^{1/2}$
M_c	Mach number based on velocity and sound speed at center of channel; $M_c = u_{1c}/a_c$
M_t	Turbulent Mach number; $M_t = \langle u_i' u_i' \rangle^{1/2} / \langle a \rangle$
M_τ	Friction Mach number based on friction velocity and wall sound speed; $M_\tau = u_\tau / a_w$
n_{ilmn}	Elements of nonlinear matrix on B-spline Galerkin method
N_1, N_2, N_3	Number of grid points in the x_1, x_2 and x_3 directions, respectively
Nu	Nusselt number; $Nu = 2H q_w / \kappa_w (T_w - T_m)$
p	Pressure
P_k	Production term of turbulent kinetic energy; $P_k = - \langle \rho \rangle \{u_1'' u_2''\} \partial \{u_1\} / \partial x_2$
Pr	Prandtl number; $Pr = \mu c_p / \kappa$
Pr_t	Turbulent Prandtl number; $Pr_t = \{u_1'' u_2''\} \, \partial\{T\}/\partial y / \left[\{T'' u_2''\} \, \partial\{u_1\}/\partial y\right]$ or $Pr_t = \kappa_u / \kappa_T$

Q	Heat source of energy equation for incompressible turbulent flow; $Q = -q_{w_{av}} / (\rho c_p H)$
q_j	Heat flux; $q_j = -\kappa \partial T / \partial x_j$, or Knot points
q_w	Wall heat flux
$q_{w_{av}}$	$q_{w_{av}} = \left(\langle q_2 \rangle |_{x_2=H} - \langle q_2 \rangle |_{x_2=-H} \right) /2$
R	Gas constant; $R = (\gamma - 1) c_p / \gamma$
$R_{\phi\phi}(r_1, x_2)$	Streamwise two-point correlation; see (2.40)
$R_{\phi\phi}(r_3, x_2)$	Spanwise two-point correlation; see (2.41)
r_1, r_3	Separations in the x_1 and x_3 directions
Re	Reynolds number based on bulk density, bulk velocity, channel half-width, and viscosity at isothermal wall ; $Re = \rho_m U_m H / \mu_{iw}$
Re_c	Reynolds number based on variables at center of channel; $Re_c = \rho_c u_{1_c} H / \mu_c$
Re_τ	Reynolds number based on wall density, friction velocity, channel half-width and wall viscosity; $Re_\tau = \rho_w u_\tau H / \mu_w$
Re_τ^*	Reynolds number based on local density, semi-local friction velocity, channel half-width, and local viscosity; $Re_\tau^* = \langle \rho \rangle u_{\tau *} H / \langle \mu \rangle$
$R_{u_1' T'}$	Correlation coefficient between velocity and temperature fluctuations; see (6.1)
S_1	Constant in the Sutherland's law
t	Time
T	Temperature
$\langle T \rangle^+$	Mean temperature scaled by friction temperature; $\langle T \rangle^+ = (T_w - \langle T \rangle) / T_\tau$

T_m	Bulk temperature; $T_m = \int_{-H}^{H} \langle \rho c_p u_1 T \rangle \, dx_2 \; / \int_{-H}^{H} \langle \rho c_p u_1 \rangle \, dx_2$
T_t	Total temperature; $T_t = T + u_i^2/(2c_p)$
T_τ	Friction temperature; $T_\tau = B_q T_w$
u_1, u_2, u_3	Velocity component in the x_1, x_2 and x_3 directions, respectively
U	U represents $\langle u_1 \rangle^+$, $\langle u_1 \rangle^+_{VD}$ and $\langle u_1 \rangle^*$
$\langle u_1 \rangle^+$	Mean streamwise velocity scaled by friction velocity; $\langle u_1 \rangle^+ = \langle u_1 \rangle / u_\tau$
$\langle u_1 \rangle^+_{VD}$	Van Driest transformed mean streamwise velocity; $\langle u_1 \rangle^+_{VD} = \int_0^{\langle u_1 \rangle^+} (\langle \rho \rangle / \rho_w)^{1/2} \; d \langle u_1 \rangle^+$
$\langle u_1 \rangle^*$	Mean streamwise velocity scaled by semi-local friction velocity; $\langle u_1 \rangle^* = \langle u_1 \rangle / u_{\tau *}$
U_m	Bulk velocity; $U_m = \int_{-H}^{H} \langle \rho u_1 \rangle \, dx_2 / (2H \rho_m)$
$(u'_\alpha)_{rms}$	RMS velocity fluctuation; $(u'_\alpha)_{rms} = \langle u'_\alpha u'_\alpha \rangle^{1/2}$ ($\alpha = 1, 2, 3$, no summation for α)
u_τ	Friction velocity; $u_\tau = (\tau_w / \rho_w)^{1/2}$
$u_{\tau *}$	Semi-local friction velocity; $u_{\tau *} = (\tau_w / \langle \rho \rangle)^{1/2}$
$\mathbf{x}$	Position vector; $\mathbf{x} = (x_1, x_2, x_3)$
x_1, x_2, x_3	Streamwise, wall-normal and spanwise directions, respectively
x_2^i	Collocation points
y	Distance from wall
y^+	Wall unit; $y^+ = \rho_w u_\tau y / \mu_w$
y^*	Semi-local wall unit; $y^* = \langle \rho \rangle \, u_{\tau *} y / \langle \mu \rangle$
y_0^+	$y_0^+ = \exp(-\kappa_u B)$

Greek Symbols

α_{k_1}	Wave number in the x_1 direction; $\alpha_{k_1} = 2\pi k_1/L_1$
α'_{k_1}	Modified wave number for the first derivative
β_{k_3}	Wave number in the x_3 direction; $\beta_{k_3} = 2\pi k_3/L_3$
δ_{ij}	Kronecker delta
δ_v	Visous length scale; $\delta_v = \mu_w / (\rho_w u_\tau)$
δ_{v*}	Semi-local visous length scale; $\delta_{v*} = \langle\mu\rangle / (\langle\rho\rangle u_{\tau*})$
Δt	Time increment
$\Delta x_1, \Delta x_2, \Delta x_3$	Grid spacing in the x_1, x_2 and x_3 directions, respectively
$\Delta x_i^+ (i = 1, 2, 3)$	Grid spacing scaled by wall variables in the $x_i (i = 1, 2, 3)$ directions; $\Delta x_i^+ = \rho_w u_\tau \Delta x_i / \mu_w$
$\Delta x_i^* (i = 1, 2, 3)$	Grid spacing scaled by local variables in the $x_i (i = 1, 2, 3)$ directions; $\Delta x_i^* = \langle\rho\rangle u_{\tau*} \Delta x_i / \langle\mu\rangle$
$\delta(x_2)$	Delta function
ϵ_{ijk}	Eddington's epsilon
γ	Ratio of specific heats; $\gamma = c_p/c_v$
κ	Thermal conductivity
κ_u	Von Kármán constant
κ_T	Constant in terms of wall law of temperature; $\kappa_T = \kappa_u/Pr_t$
μ	Molecular viscosity
ν	Kinematic viscosity
ρ	Density

ρ_m	Bulk density; $\rho_m = \int_{-H}^{H} \langle\rho\rangle \, dx_2/(2H)$
τ_{ij}	Viscous stress tensor; see (A.4)
τ_w	Wall stress
$\tau_{w_{av}}$	$\tau_{w_{av}} = (\langle\tau_{12}\rangle_{x_1-x_3}\big\vert_{x_2=H} - \langle\tau_{12}\rangle_{x_1-x_3}\big\vert_{x_2=-H})/2$
$\phi_{jk_1k_3}$	Expansion coefficient of B-spline
ϕ_j^ℓ	Expansion coefficient of B-spline for the ℓ-th derivative
Ψ_i	Weight function
$\omega_i' \quad (i=1,2,3)$	Vorticity fluctuation in the x_i directions; $\omega_i' = \epsilon_{ijk}\partial u_k/\partial x_j$
ε_c	Dissipation per unit mass; $\varepsilon_c = \varepsilon_k/\langle\rho\rangle$
ε_{cc}	Compressible part of ε_c; $\varepsilon_{cc} = \varepsilon_c - \varepsilon_{ci}$
ε_{ci}	Incompressible part of ε_c; $\varepsilon_{ci} = (\langle\mu\rangle / \langle\rho\rangle) \langle(\partial u_i'/\partial x_j)^2\rangle$
ε_k	Dissipation of turbulent kinetic energy equation per unit volume; $\varepsilon_k = \langle\tau_{ij}'\partial u_i'/\partial x_j\rangle$
ε_{k1}	Enstropy dissipation term; $\varepsilon_{k1} = \langle\mu\rangle \langle\omega_i'\omega_i'\rangle$
ε_{k2}	Dilatational dissipation term; $\varepsilon_{k2} = -2/3 \langle\mu\rangle \langle d'd'\rangle$
ε_{k3}	Dissipation term with respect to viscosity fluctuation; $\varepsilon_{k3} = \partial\langle u_i\rangle/\partial x_j \langle\mu'\partial u_i'/\partial x_j\rangle$
ε_{TK}	Turbulent dissipation of mean kinetic energy equation per unit volume; $\varepsilon_{TK} = -\langle\rho\rangle \{u_1''u_2''\}\partial\{u_1\}/\partial x_2$
ε_{VK}	Viscous dissipation of mean kinetic energy equation per unit volume; $\varepsilon_{VK} = \langle\tau_{i2}\rangle \partial\langle u_i\rangle/\partial x_2$
ε_{VKc}	Compressible part of ε_{VK}; $\varepsilon_{VKc} = \varepsilon_{VK} - \varepsilon_{VKi}$
ε_{VKi}	Incompressible part of ε_{VK}; $\varepsilon_{VKi} = \langle\mu\rangle (\partial\langle u_1\rangle/\partial x_2)^2$

Abbreviations

CPU	Central Processing Unit
DNS	Direct Numerical Simulation
ENO	Essentially Non-Oscillatory
FDM	Finite Difference Method
LES	Large Eddy Simulation
LHS	Left Hand Side
RHS	Right Hand Side
RMS	Root Mean Square
SRA	Strong Reynolds Analogy
TVD	Total Variation Diminishing
1D	One-Dimensional
$(Cont.) = 0$	Continuity equation
$(Div.)_\phi$	Divergence form of convection for ϕ
$(Adv.)_\phi$	Advective form of convection for ϕ
$(Skew.)_\phi$	Skew-symmetric form of convection for ϕ
$(Skew.B)_\phi$	Skew-symmetric form proposed by Blaisdell *et al.* (1993)
$(Skew.M)_\phi$	Skew-symmetric form proposed by Morinishi *et al.* (2001)

Other Symbols

$\overline{(\ )}$	Complex conjugate
$\widehat{(\ )}$	Fourier coefficient, or Spline interpolation function
$\vec{(\ )}$	Vector variable
$\langle\ \rangle$	Reynolds average over time and x_1 and x_3 directions
$\{\ \}$	Favre average over time and x_1 and x_3 directions
$\langle\ \rangle_{x_1-x_3}$	Spatial average over x_1 and x_3 directions
$\langle\ \rangle_{x_1-t}$	Average over time and x_1 direction
$\langle\ \rangle_{x_3-t}$	Average over time and x_3 direction
$(\ )^+$	Value scaled by wall variables
$(\ )^\dagger$	Non-dimensional value scaled by H, ρ_m, U_m and values at isothermal wall
$(\ )^*$	Non-dimensional value scaled by semi-local friction velocity $u_{\tau *}$, e.g. Re_τ^*, $\langle u_1 \rangle^*$ and y^*
$(\ )'$	Turbulent fluctuation with respect to Reynolds average
$(\ )''$	Turbulent fluctuation with respect to Favre average
$(\ )_c$	Value at center of channel
$(\ )_{aw}$	Value at adiabatic wall
$(\ )_{iw}$	Value at isothermal wall
$(\ )_{rms}$	RMS value
$(\ )_w$	Wall value
$\Leftarrow$	Modification done in the direction

Chapter 1.

Introduction

1.1 Background

It is considerably important to clarify the detailed mechanism of wall-bounded compressible turbulent flow for engineering and industrial applications. Since the 1950's, many experimental studies have provided valuable knowledge about the friction coefficient, the mean velocity profiles and so on (e.g., see Bradshaw 1977; Fernholz & Finley 1977, 1980; Spina *et al.* 1994; Smits & Dussauge 1996). The compressibility effects are commonly distinguished into two types: a mean variable property effect due to the variations in mean properties such as density and viscosity, and an intrinsic compressibility effect due to fluctuations of thermodynamic quantities, mean dilatation and its fluctuation. Morkovin (1962) proposed the hypothesis that the compressibility effect was mainly due to the variable property effect and that the turbulence structures of compressible boundary layers were comparable with those of incompressible ones when the variable property effect was taken into account (see Morkovin 1962; Bradshaw 1977; Smits & Dussauge 1996). This hypothesis has long been widely acknowledged to be correct in the study of the wall-bounded compressible turbulent flow, and is referred to as 'Morkovin's hypothesis'. In the analysis of wall-bounded compressible turbulent flow, the Van Driest transformation (see Van Driest 1951; Rotta 1960), which is supported by Morkovin's hypothesis, is well known. A Reynolds analogy which relates the mass transfer to the heat transfer is known in the incompressible

turbulent shear flow (see White 1991). Morkovin (1962) also reported that the Reynolds analogy could be applied to the wall-bounded compressible turbulent flow. This concept is referred to as 'Strong Reynolds Analogy (SRA)'. The SRA is applicable to the adiabatic wall for the compressible turbulent flow. Recently, some modified Reynolds analogies applicable to the isothermal wall have been proposed by Gaviglio (1987), Rubesin (1990) and Huang *et al.* (1995).

Fernholz & Finley (1980) observed in the compressible turbulent zero-pressure-gradient boundary layer flows on isothermal and adiabatic walls that the Van Driest transformed velocity profile agreed well with the data of the incompressible turbulent flow. On the other hand, Zhang *et al.* (1993) reported that the untransformed velocity profile near the adiabatic wall agreed well with the data of the incompressible turbulent flow. Huang & Coleman (1994) pointed out that the Van Driest transformation did not work well for low Reynolds number flow, while it was useful for high Reynolds number flow (see also Fernholz & Finley 1980; Spina 1994). In spite of many experimental efforts, the mean velocity profile of the wall-bounded compressible flows remains unclear. Other statistics have not been understood enough, because experimental measurements of such as thermodynamic state quantities in high speed flow are very difficult (see Spina *et al.* 1994; Smits & Dussauge 1996). Actually, the mean temperature profile in the wall-normal direction has been often estimated by using the mean velocity in the experimental study.

In the last decade, with the rapid growth of the computational resources, the direct numerical simulation (DNS) has been performed to investigate the wall-bounded compressible turbulent flow as an alternative method (e.g., Coleman *et al.* 1995; Guarini *et al.* 2000; Maeder *et al.* 2001). DNS of the wall-bounded compressible turbulent flow is considerably appealing because it provides entirely three-dimensional and time-dependent data which are very difficult or even impossible to obtain experimentally. However, reliable DNS results are lacking despite their engineering importance. As typical DNS results, Coleman *et al.* (1995) performed the DNS of the turbulent channel flow between isothermal

walls. And Guarini *et al.* (2000) performed the DNS of the boundary layer flow on the adiabatic wall. They reported that the Van Driest transformed velocity agrees well with the data on the wall-bounded incompressible turbulent flow. However, the influence of different wall boundary conditions (isothermal and adiabatic conditions) on the mean velocity and temperature profiles has not been investigated. Comparison of compressible and incompressible turbulent flows in terms of the temperature field in addition to the velocity field is also very important for accurate understanding of the compressible turbulent flow. However, there have been no studies to date in which the statistics relative to the temperature of compressible turbulent flow are compared to those of incompressible turbulent flow.

In terms of turbulence statistics, Coleman *et al.* (1995) and Guarini *et al.* (2000) reported that the variable property effect should be taken into account in the scaling. However, thermodynamic fluctuations such as density and temperature have not been sufficiently examined. So *et al.* (1998) reported that Morkovin's hypothesis was applicable to the near-wall asymptotic behaviors of turbulence statistics not shown in logarithmic coordinates. Huang *et al.* (1995) showed that their modified Reynolds analogy agreed well with the DNS data of Coleman *et al.* (1995) for compressible turbulent channel flow between isothermal walls. Guarini *et al.* (2000) showed that the modified Reynolds analogy proposed by Huang *et al.* (1995) was effective for boundary layer flow on the adiabatic wall. However, the applicability and usefulness for other flows strongly affected by the opposite wall (e.g., the turbulent channel flow between adiabatic and isothermal walls) have not been examined.

A detailed understanding of the energy transfer in wall-bounded compressible turbulent flow requires reliable data on the turbulent kinetic, mean kinetic and internal energy budgets, because the energy is exchanged among the internal energy, mean and turbulent kinetic energies (see Lele 1994; Huang *et al.* 1995). However, reliable DNS data on the energy budgets for the wall-bounded compressible turbulent flow are less available than on the wall-bounded incom-

pressible turbulent flow. Huang *et al.* (1995) investigated the energy transfer near the isothermal wall using the DNS data on compressible turbulent channel flow presented by Coleman *et al.* (1995). Guarini *et al.* (2000) reported that the turbulent kinetic energy budget near the adiabatic wall in the compressible turbulent boundary layer flow was almost the same as that of the wall-bounded incompressible turbulent flow. However, the knowledge of the difference and similarity between energy transfers near isothermal and adiabatic walls remains insufficient. In addition, compressible and incompressible flows have not been sufficiently compared.

In order to understand the wall-bounded compressible turbulent flow, it is very important to clarify near-wall turbulence structures in addition to mean velocity and temperature profiles, turbulence statistics and energy transfers. The knowledge on the near-wall turbulence structure for the incompressible turbulent flow was summarized by Robinson (1991). On the other hand, there have only been a few studies of near-wall turbulence structure for the compressible turbulent flow. Coleman *et al.* (1995) reported that streak structures near the isothermal wall became more coherent in the streamwise direction as the Mach number increased. Guo & Adams (1995) performed DNS of a compressible boundary layer flow developing on the isothermal wall in the adiabatic boundary condition, and showed that streak structures near the wall were larger than those of incompressible turbulent flow. Wang & Pletcher (1996) performed a large eddy simulation (LES) of the isothermal channel flow between hot and cold walls for the almost zero Mach number, and reported that the cold wall side exhibited stronger coherence of the near-wall streak structure. The LES of the turbulent channel flow with constant heat flux for the almost zero Mach number was also performed by Dailey & Pletcher (1999) who showed that the turbulent structures appeared to be more coherent on the cold wall side and less coherent on the heating wall side. However, why the modification of the near-wall streak structures occurs is still not sufficiently understood. In particular, the detailed turbulence structures near the adiabatic wall have not been found so far. It is also uncer-

tain whether or not Morkovin's hypothesis relative to turbulence structures near adiabatic and isothermal walls is successful.

1.2 Numerical Algorithm

DNS offers useful information about the understanding and modeling of turbulent flow. However, the sufficient DNS data of wall-bounded compressible turbulent flow has not been provided because of the lack of the useful DNS algorithm for the wall-bounded compressible turbulent flow. The typical DNS algorithms are as follows.

Coleman *et al.* (1995) performed the DNS of compressible turbulent channel flow between isothermal walls. The simulation was carried out using the DNS algorithm based on the Legendre Galerkin method (developed by Buell 1990, 1991). Although the DNS algorithm based on the Galerkin method which is expensive to calculate the nonlinear term is applicable to the Dirichlet boundary condition, it is difficult to apply the Neumam boundary condition and, therefore, to treat the adiabatic wall. However, the study of compressible turbulent flow near the adiabatic boundary is important for engineering applications.

Guarini *et al.* (2000) performed the DNS of compressible boundary layer flow at an adiabatic wall using the DNS algorithm based on the B-spline Galerkin method first developed for the incompressible flow (see Loulou *et al.* 1997; Kravchenko *et al.* 1996, 1999). Loulou *et al.* (1997) and Kravchenko *et al.* (1999) reported that, respectively, 85% and more than 50% of central processing unit (CPU) time was spent on the evaluation of the nonlinear terms. The B-spline Galerkin method for the compressible turbulent flow with variable fluid properties might be extremely expensive even if one could provide the adiabatic boundary condition accurately. Note that Guarini *et al.* (2000) treated the adiabatic boundary condition through weak formation (see Guarini 1998 in detail). Although a collocation method can be used instead of the Galerkin method in order to reduce the cost of evaluating nonlinear terms, the B-spline collocation method has not been previously applied to wall-bounded compressible turbu-

lent flows. On the other hand, Bottela (2000, 2001) has attempted to simulate incompressible turbulent flow using the B-spline collocation method.

Recently, Maeder *et al.* (2001) and Lechner *et al.* (2001) simulated a compressible boundary layer developing on the laminar adiabatic wall (constant temperature wall) and the turbulent supersonic isothermal-wall channel flow, respectively, using the DNS algorithm based on a Padé (compact) finite-difference method (FDM) (see Lele 1992). While the Padé FDM is also an economical alternative, the wall boundary treatment cannot be determined uniquely because the higher order FDM generally requires a wall scheme.

1.3 Objectives

The purpose of the present study is to investigate the detailed mechanism of the wall-bounded compressible turbulent flow. In particular, the wall-bounded flow with the adiabatic wall is still not understood in spite of its engineering importance. In order to clarify the compressible turbulent flows near isothermal and adiabatic walls, we perform DNS of the compressible turbulent channel flow between adiabatic and isothermal walls that has not been previously performed by the DNS. The present study of the compressible turbulent channel flow between adiabatic and isothermal walls is also very important for complementing studies of Coleman *et al.* (1995) and Guarini *et al.* (2000). However, it is difficult to simulate the flow accurately and efficiently using the existing DNS algorithm for the wall-bounded compressible turbulent flow as mentioned in section 1.2.

There is still no universal theory for wall-bounded compressible turbulent flow. Consequently, understanding of the wall-bounded compressible turbulent flow has been usually obtained from comparison with the incompressible one, for instance, the Van Driest transformation. Therefore, the understanding of the wall-bounded incompressible turbulent flow is also very important for that of the wall-bounded compressible turbulent flow. We focus on the similarity and difference between compressible and incompressible turbulent channel flows, as well as the effects of the different boundary conditions on the compressible

turbulent flow.

The objective of the present study is achieved according to the following procedures:

1. To perform the DNS for the compressible turbulent channel flow between adiabatic and isothermal walls, a new DNS algorithm is proposed in which B-spline collocation method is used in the wall-normal direction and the skew-symmetric form for convection term is adapted for the stable numerical simulation. To show the reliability of the present algorithm, the DNS of compressible turbulent flow between isothermal walls, which corresponds to the DNS of Coleman *et al* (1995), is performed. Note that the present algorithm does not aim at simulating flow with strong discontinuities like shock waves. The shock-capturing method, like essentially non-oscillatory (ENO) and total variation diminishing (TVD) schemes, may be coupled with to simulate such a flow (see Adams *et al.* 1996; Adams 2000).

2. To investigate the difference and similarity between flows near adiabatic and isothermal walls for the wall-bounded compressible turbulent flow, the DNS of the compressible turbulent channel flow between adiabatic and isothermal walls is performed using the constructed DNS algorithm.

3. To clarify the difference and similarity between compressible and incompressible turbulent channel flows, the DNS of the incompressible turbulent channel flow with passive scalar transport between adiabatic and isothermal walls is carried out. This flow has not been previously performed by DNS. DNS of incompressible turbulent flow between isothermal walls, which corresponds to that of Kim & Moin (1989), is performed by the way of comparison.

1.4 Organization of Dissertation

This dissertation is arranged as follows.

Chapter 2 proposes a new DNS algorithm based on the B-spline collocation method to simulate compressible turbulent flow between adiabatic and isothermal walls. The skew-symmetric form which is suitable for a wall-bounded compressible flow is presented for the convection term to maintain numerical stability.

In chapter 3, the effects of the different thermal wall boundary conditions on mean velocity and temperature profiles are explained through the dependence of the non-dimensional heat flux and the friction Mach number. The scaling laws of mean velocity and temperature profiles are also discussed.

In Chapter 4, the profiles of turbulence statistics and the near-wall asymptotic behaviors are discussed for compressible turbulent flow. Moreover, the applicability and usefulness of the Reynolds analogy and the modified Reynolds analogy are examined using the present simulation results.

In chapter 5, the turbulent kinetic, mean kinetic and internal energy budgets are calculated and the mechanism of the energy transfer near isothermal and adiabatic walls is investigated.

In chapter 6, the near-wall turbulence structures, in particular, the streak structures near adiabatic and isothermal walls, are investigated for compressible turbulent flow. In addition, the difference in turbulence structures between compressible and incompressible turbulent flows is explored.

Key results are summarized and a conclusion is given in chapter 7, which ends with a brief discussion of the future work.

The equations governing compressible and incompressible flows are given in Appendix A.

Appendix B gives a short summary of B-splines and their properties.

Chapter 2.

Numerical Methods

2.1 Outline

In this chapter, the numerical algorithm that can simulate the compressible turbulent channel flow between adiabatic and isothermal walls is introduced. The skew-symmetric form for convection term which is used in the DNS algorithm to maintain numerical stability is proposed. Next, the discrete method in space and time is explained in detail. To confirm that the present DNS data has the sufficient resolution and domain size, the one-dimensional energy spectrum and two-point correlation are also examined.

2.2 Basic Equations

The x_1-, x_2- and x_3-directions are the streamwise, wall-normal and spanwise directions, respectively. The variables u_i $(i = 1, 2, 3)$, ρ, p, t, T, μ and κ are the velocity component in the x_i $(i = 1, 2, 3)$ direction, the density, the pressure, the time, the temperature, the molecular viscosity and the thermal conductivity, respectively. The variables in the continuity, momentum and energy equations (see (A.1)–(A.3)) are non-dimensionalized by the channel half-width H, the bulk velocity U_m, the bulk density ρ_m, the temperature at the isothermal wall T_{iw}, the molecular viscosity at the isothermal wall μ_{iw} and the thermal conductivity at the isothermal wall κ_{iw}, where $x_i^\dagger = x_i/H$ $(i = 1, 2, 3)$, $u_i^\dagger = u_i/U_m$ $(i = 1, 2, 3)$, $\rho^\dagger = \rho/\rho_m$, $p^\dagger = p/(\rho_m U_m^2)$, $t^\dagger = t/(H/U_m)$, $T^\dagger = T/T_{iw}$, $\mu^\dagger = \mu/\mu_{iw}$ and

$\kappa^\dagger = \kappa/\kappa_{iw}$. Note that $\mu^\dagger = \kappa^\dagger$ because the specific heat at constant pressure c_p and the Prandtl number $Pr = \mu c_p/\kappa$ are constants in the present study. The ratio of specific heats is $\gamma = c_p/c_v$, where c_v is specific heat at constant volume. The Mach number based on bulk velocity and isothermal wall temperature is $M = U_m/\left(\gamma R T_{iw}\right)^{1/2}$, and the Reynolds number based on the bulk density, bulk velocity, channel half-width, and viscosity at the isothermal wall is $Re = \rho_m U_m H/\mu_{iw}$. The non-dimensional continuity, momentum and energy equations are

$$\frac{\partial \rho^\dagger}{\partial t^\dagger} = -\frac{\partial(\rho^\dagger u_j^\dagger)}{\partial x_j^\dagger}, \tag{2.1}$$

$$\frac{\partial u_i^\dagger}{\partial t^\dagger} = -u_j^\dagger \frac{\partial u_i^\dagger}{\partial x_j^\dagger} - \frac{1}{\gamma M^2 \rho^\dagger}\frac{\partial(\rho^\dagger T^\dagger)}{\partial x_i^\dagger} + \frac{1}{Re\rho^\dagger}\frac{\partial \tau_{ij}^\dagger}{\partial x_j^\dagger} + f_i^\dagger, \tag{2.2}$$

$$\begin{aligned}\frac{\partial T^\dagger}{\partial t^\dagger} = &-u_j^\dagger \frac{\partial T^\dagger}{\partial x_j^\dagger} - (\gamma-1)\, T^\dagger \frac{\partial u_j^\dagger}{\partial x_j^\dagger} + \frac{\gamma\,(\gamma-1)\, M^2 \tau_{ij}^\dagger}{Re\rho^\dagger}\frac{\partial u_i^\dagger}{\partial x_j^\dagger} \\ &+ \frac{\gamma}{RePr\rho^\dagger}\frac{d\mu^\dagger}{dT^\dagger}\frac{\partial T^\dagger}{\partial x_j^\dagger}\frac{\partial T^\dagger}{\partial x_j^\dagger} + \frac{\gamma\mu^\dagger}{RePr\rho^\dagger}\frac{\partial^2 T^\dagger}{\partial x_j^\dagger \partial x_j^\dagger}\ ,\end{aligned} \tag{2.3}$$

where

$$\tau_{ij}^\dagger = \mu^\dagger\left(\frac{\partial u_i^\dagger}{\partial x_j^\dagger} + \frac{\partial u_j^\dagger}{\partial x_i^\dagger} - \frac{2}{3}\frac{\partial u_k^\dagger}{\partial x_k^\dagger}\delta_{ij}\right). \tag{2.4}$$

We shall employ the summation convention in which repeated italic indices are summed. The bulk density ρ_m and the bulk velocity U_m are

$$\rho_m = \frac{1}{2H}\int_{-H}^{H}\langle\rho\rangle\, dx_2, \tag{2.5}$$

$$U_m = \frac{1}{2H\rho_m}\int_{-H}^{H}\langle\rho u_1\rangle\, dx_2. \tag{2.6}$$

Viscosity $\mu^\dagger$ is given by Sutherland's law:

$$\mu^\dagger = \frac{1 + S_1/T_{iw}}{T^\dagger + S_1/T_{iw}} T^{\dagger\frac{3}{2}}. \tag{2.7}$$

The non-dimensional state equation and driving force $f_i^\dagger$ are

$$p^\dagger = \frac{1}{\gamma M^2}\rho^\dagger T^\dagger, \tag{2.8}$$

$$f_i^\dagger = -\frac{\left[\langle\tau_{12}^\dagger\rangle_{x_1-x_3}\big|_{x_2^\dagger=1} - \langle\tau_{12}^\dagger\rangle_{x_1-x_3}\big|_{x_2^\dagger=-1}\right]\delta_{i1}}{2Re}. \tag{2.9}$$

A mean pressure gradient is imposed to drive the flow in the DNS of incompressible turbulent channel flow. Although the driving force $f_i^\dagger$ has the same role in the DNS of compressible turbulent channel flow, it is not interpreted as the mean pressure gradient, since pressure is given by the state equation (2.8) (see Coleman *et al.* 1995; Huang *et al.* 1995).

2.3 Form of Convection Term

It is important to maintain numerical stability for the numerical simulation of turbulent flow. Dealiasing is often used to remove the nonlinear instability in the DNS of the turbulent flow (see Blaisdell *et al.* 1993). Blaisdell *et al.* (1993) reported that the magnitude of the aliasing errors was reduced for the skew-symmetric form compared to divergence and advective forms. Using a Fourier analysis, they showed that the skew-symmetric form had a smaller amplitude for the aliasing errors coming from the region close to the resolved wave number range than the other formulations. Kravchenko & Moin (1997) also reported that the aliasing errors due to the advective and divergence forms were of opposite signs, then the skew-symmetric form reduced aliasing errors. Coleman *et al.* (1995) used the advective form for convection term, thus they must give about 30 % more collocation points in x_1, x_2 and x_3 directions than modes to eliminate aliasing errors. The skew-symmetric form is the alternative method to reduce the aliasing errors and to inhibit nonlinear instability while saving the numerical capacity and cost, since the full dealiasing by the padding method is not practical in the DNS of compressible flow with variable fluid properties. Blaisdell *et al.* (1993) maintained the numerical stability by using the skew-symmetric form in the DNS of homogeneous compressible turbulent shear flow. In the present simulations, the skew-symmetric form is also used to maintain numerical stability. The basic equations are different from those used in Blaisdell *et al.* (1993); the present skew-symmetric form used in our study is described below.

$(Cont.) = 0$ represents the continuity equation.

$$(Cont.) = \frac{\partial \rho}{\partial t} + \frac{\partial (\rho u_j)}{\partial x_j} = 0 \tag{2.10}$$

$(Div.)_\phi$, $(Adv.)_\phi$ and $(Skew.)_\phi$ represent the divergence, advective and skew-symmetric forms of the convection term for ϕ (=u_1, u_2, u_3 and T), respectively:

$$(Div.)_\phi = \frac{\partial (\rho\phi)}{\partial t} + \frac{\partial (\rho\phi u_j)}{\partial x_j} \tag{2.11}$$

$$(Adv.)_\phi = \rho\frac{\partial \phi}{\partial t} + \rho u_j \frac{\partial \phi}{\partial x_j} \tag{2.12}$$

$$(Skew.)_\phi = \frac{1}{2}(Div.)_\phi + \frac{1}{2}(Adv.)_\phi \tag{2.13}$$

$(Div.)_\phi$, $(Adv.)_\phi$ and $(Skew.)_\phi$ are connected with each other through the following analytical relations as those of the incompressible flow (see Morinishi *et al.* 1998):

$$(Adv.)_\phi = (Div.)_\phi - \phi(Cont.), \tag{2.14}$$

$$(Skew.)_\phi = (Div.)_\phi - \frac{1}{2}\phi(Cont.), \tag{2.15}$$

$$= (Adv.)_\phi + \frac{1}{2}\phi(Cont.). \tag{2.16}$$

As long as $(Cont.) = 0$ is satisfied, $(Adv.)_\phi$ and $(Skew.)_\phi$ are analytically conservative. Note that these exchanges in compressible flow require time derivative terms. Here, Blaisdell *et al.* (1993) used the following skew-symmetric form with the time derivative term $(Skew.B)_\phi$.

$$(Skew.B)_\phi = \frac{\partial (\rho\phi)}{\partial t} + \frac{1}{2}\left[u_j \frac{\partial (\rho\phi)}{\partial x_j} + \rho\phi \frac{\partial u_j}{\partial x_j} + \frac{\partial (\rho\phi u_j)}{\partial x_j} \right] \tag{2.17}$$

It is difficult to apply $(Skew.B)_\phi$ to wall-bounded compressible turbulent flow, since the density in the computational region and on the boundary should be estimated at the same time and it is difficult to give the adiabatic boundary condition in the time dependent equation of ρT. Therefore, in the present simulations the skew-symmetric form with the time derivative term $(Skew.M)_\phi$ is introduced by using (2.10) and (2.13).

$$(Skew.M)_\phi = \rho\frac{\partial \phi}{\partial t} + \frac{1}{2}\left[\rho u_j \frac{\partial \phi}{\partial x_j} + \frac{\partial (\rho\phi u_j)}{\partial x_j} - \phi \frac{\partial (\rho u_j)}{\partial x_j} \right] \tag{2.18}$$

The comparison between skew-symmetric and advective forms in a simulation will be done in section 2.10.

2.4 Discrete Method in Space

The Fourier Galerkin method (see Canuto *et al.* 1988) is used for the periodic (x_1 and x_3) directions. The variable $\phi^\dagger$ is represented by the discrete Fourier series expansion as follows.

$$\phi^\dagger\left(\mathbf{x}^\dagger\right) = \sum_{k_1=-N_1/2}^{N_1/2-1} \sum_{k_3=-N_3/2}^{N_3/2-1} \hat{\phi^\dagger}_{k_1k_3}(x_2^\dagger) e^{\mathrm{i}(\alpha_{k_1}x_1^\dagger+\beta_{k_3}x_3^\dagger)} \ , \tag{2.19}$$

Equation (2.19) is substituted into (2.1)–(2.3), and then the Fourier pseudo-spectral method is applied in the periodic directions. As a result, the basic equation of the Fourier coefficient for an unknown variable $\phi^\dagger(=\rho^\dagger,\ u_1^\dagger,\ u_2^\dagger,\ u_3^\dagger,\ T^\dagger)$ is obtained.

$$\frac{\partial \hat{\phi}^\dagger_{k_1k_3}(x_2^\dagger)}{\partial t^\dagger} \ = \ \hat{S}_{\phi^\dagger k_1k_3}(x_2^\dagger), \tag{2.20}$$

where $\hat{S}_{\phi^\dagger k_1k_3}(x_2^\dagger)$ is evaluated by the discrete Fourier transformation of $S_{\phi^\dagger}$ (pseudo-spectral method). The Fourier coefficient $\hat{\phi}_{k_1k_3}(x_2^\dagger)$ is obtained by integrating (2.20). The B-spline collocation method is used in the wall-normal (x_2) direction. The Fourier coefficient $\hat{\phi}_{k_1k_3}(x_2^\dagger)$ is expanded by the B-spline of order k (see Appendix B.1).

$$\hat{\phi^\dagger}_{k_1k_3}(x_2^\dagger) = \sum_{j=1}^{N_2} \phi^\dagger_{jk_1k_3} B_j^k(x_2^\dagger) \tag{2.21}$$

When (2.21) is integrated after being multiplied by weight function $\Psi_i(x_2^\dagger)$ $(i = 1, \cdots, N_2)$, the following equation is obtained.

$$\int_{-1}^{1} \Psi_i(x_2^\dagger) \sum_{j=1}^{N_2} \phi^\dagger_{jk_1k_3} B_j^k(x_2^\dagger) dx_2^\dagger = \int_{-1}^{1} \Psi_i(x_2^\dagger) \hat{\phi^\dagger}_{k_1k_3}(x_2^\dagger) dx_2^\dagger \tag{2.22}$$

Since $\Psi_i(x_2^\dagger)$ is $\delta(x_2^\dagger - x_2^{\dagger i})$ for the collocation method, equation (2.22) becomes the following equation.

$$\sum_{j=1}^{N_2} \phi^\dagger_{jk_1k_3} B_j^k(x_2^{\dagger i}) = \hat{\phi^\dagger}_{k_1k_3}(x_2^{\dagger i}), \ \ (i = 1, \cdots, N_2) \tag{2.23}$$

In addition, no-slip, adiabatic and isothermal wall boundary conditions are, respectively, as follows.

$$\sum_{j=1}^{N_2} u_{1\ jk_1k_3}^{\dagger}\ B_j^k(x_2^{\dagger})\Big|_{\text{wall}} = \sum_{j=1}^{N_2} u_{2\ jk_1k_3}^{\dagger}\ B_j^k(x_2^{\dagger})\Big|_{\text{wall}} = \sum_{j=1}^{N_2} u_{3\ jk_1k_3}^{\dagger}\ B_j^k(x_2^{\dagger})\Big|_{\text{wall}} = 0 \quad (2.24)$$

$$\sum_{j=1}^{N_2} T_{jk_1k_3}^{\dagger}\ \frac{dB_j^k(x_2^{\dagger})}{dx_2^{\dagger}}\Bigg|_{\text{adiabatic wall}} = 0 \quad (2.25)$$

$$\sum_{j=1}^{N_2} T_{jk_1k_3}^{\dagger}\ B_j^k(x_2^{\dagger})\Big|_{\text{isothermal wall}} = \begin{cases} 1 & (k_1, k_3 = 0) \\ 0 & (\text{others}) \end{cases} \quad (2.26)$$

When the temperatures of both isothermal walls are different, the value of zero mode in (2.26) depends on the temperature difference. Density at the walls is solved by using (2.23) with $i = 1$ and N_2. The equation on the vector of coefficient of B-spline $\vec{\phi}^{\dagger}{}_{k_1k_3}$ is constructed from (2.23) to (2.26).

$$\mathbf{B}\ \vec{\phi}^{\dagger}{}_{k_1k_3} = \vec{r}^{\dagger}{}_{k_1k_3}, \quad (2.27)$$

where $\mathbf{B}$ is the matrix $(N_2 \times N_2)$ and $\vec{r}^{\dagger}{}_{k_1k_3}$ is the RHS vector. Once (2.27) is solved for the wave modes (k_1, k_3) for each variable, the B-spline coefficient $\phi_{jk_1k_3}^{\dagger}$ is obtained. Since $B_j^k(x_2)$ has the compact support, matrix $\mathbf{B}$ is a banded matrix (see Kravchenko & Moin 1998). Equation (2.27) is solved by LU decomposition. Although the B-spline Galerkin method is available, the B-spline collocation method is used in the present algorithm because of the low computational cost. The comparison of numerical costs between the B-spline Galerkin and collocation methods is presented in the following subsection.

2.5 Comparison of B-spline Galerkin and Collocation Methods

Loulou *et al.* (1997) and Kravchenko *et al.* (1999) reported that using the B-spline Galerkin method to calculate the nonlinear terms of incompressible turbulent flow was expensive. In this section, we compare the number of the operation counts of a nonlinear term, $d(\rho u_1 u_2)/dx_2$, between the B-spline Galerkin and collocation methods for wall-bounded compressible turbulent flow.

In a case using the B-spline Galerkin method, the integration of the products of B-spline in the wall-normal direction is evaluated as

$$\sum_l \sum_m \sum_n \left[\int_{-H}^{+H} B_i^k(x_2) \frac{dB_l^k(x_2) B_m^k(x_2) B_n^k(x_2)}{dx_2} dx_2 \right] \rho_l \, u_{1\,m} u_{2\,n}$$
$$= \sum_l \sum_m \sum_n n_{ilmn} \rho_l \, u_{1\,m} u_{2\,n}, \tag{2.28}$$

where the integral in brackets (n_{ilmn}) is usually pre-computed and stored. The sums of (2.28) can be evaluated in order $N_2(2k+1)^3$ operations.

On the other hand, the calculation using the B-spline collocation method are as follows. First of all, the function $\zeta(x_2^i)$ is calculated as

$$\zeta(x_2^i) = \rho(x_2^i) u_1(x_2^i) u_2(x_2^i), \;\; (i = 1, \cdots, N_2) \tag{2.29}$$

where the number of operation counts is N_2. Second, the coefficient of B-spline interpolation for the function $\zeta(x_2^i)$ is obtained by solving the following equation.

$$\zeta(x_2^i) = \sum_j \zeta_j B_j^k(x_2^i), \;\; (i = 1, \cdots, N_2) \tag{2.30}$$

where the number of operation counts is $N_2 k$. Finally, using the coefficient ζ_j, the derivative of $\zeta(x_2)$ is gained at the collocation points as

$$\frac{d(\rho u_1 u_2)}{dx_2}(x_2^i) = \sum_j \zeta_j^1 B_j^k(x_2^i), \;\; (i = 1, \cdots, N_2) \tag{2.31}$$

where the number of operation counts is $N_2 k$. Thus, the total operation counts using the B-spline collocation method are about $N_2(2k+1)$.

For instance, the operation counts of the fourth order B-spline Galerkin method are about 40 times larger than that of the eighth order B-spline collocation method. Note that the orders of the B-spline Galerkin and collocation methods give the same modified wave numbers for derivatives (see Kravchenko & Moin 1998 in detail). Although the estimate used here is done only for one nonlinear term, it is easily expected that the B-spline collocation method can allow a drastic reduction in the cost of simulating wall-bounded compressible turbulent flow. In addition, note that calculations of the other terms such as

the diffusion term using the B-spline Galerkin method are also expensive for compressible turbulent flows with variable fluid properties.

Note that the memory requirement of B-spline collocation method is much smaller than that of B-spline Galerkin method which requires a lot of matrices (see Guarini 1998).

2.6 Discrete Method in Time

The time-advancement scheme in this study is a third-order compact storage Runge–Kutta method (RK3) developed by Wray (1986) (see Spalart 1991). Since periodic boundary conditions are used in the present simulations, the mass and momentum should be conserved. In the present simulation, the driving force, (2.9), is given at each time step in order to conserve mass and momentum. However, the numerical error due to the time advancements slightly destroys the conservations, since the continuity equation in compressible flow contains the time derivative term. Coleman *et al.* (1995) avoided this problem by setting the zero (prime) Legendre polynomial mode of density in advance (see Buell 1990). Since this device is only applicable to the orthogonal polynomials, the corresponding procedure is introduced in this study. The mass C_1^n and momentum C_2^n at time t_n are given by (2.32) and (2.33).

$$\int_0^{L_1}\int_{-H}^{H}\int_0^{L_3} \rho(\mathbf{x},t_n)d\mathbf{x} = C_1^n \tag{2.32}$$

$$\int_0^{L_1}\int_{-H}^{H}\int_0^{L_3} \rho(\mathbf{x},t_n)u_1(\mathbf{x},t_n)d\mathbf{x} = C_2^n \tag{2.33}$$

The averages over the streamwise and spanwise directions for density and streamwise velocity are modified by (2.34) and (2.35) respectively.

$$\langle\rho(x_2)\rangle_{x_1-x_3} \Leftarrow \frac{\rho_m^0}{\rho_m^n}\times\langle\rho(x_2)\rangle_{x_1-x_3} = \frac{C_1^0}{C_1^n}\times\langle\rho(x_2)\rangle_{x_1-x_3}\,, \tag{2.34}$$

$$\langle u_1(x_2)\rangle_{x_1-x_3} \Leftarrow \frac{U_m^0}{U_m^n}\times\langle\rho(x_2)\rangle_{x_1-x_3} = \frac{C_1^n}{C_1^0}\times\frac{C_2^0}{C_2^n}\times\langle u_1(x_2)\rangle_{x_1-x_3}\,, \tag{2.35}$$

where $\langle\ \rangle_{x_1-x_3}$ represents spatial average over x_1 and x_3 directions. C_1^0 and C_2^0 are mass and momentum at the initial time and $\Leftarrow$ represents the modification

done in the direction. The modifications are small enough to be negligible after the turbulent flows become stationary. We confirmed that the errors of mass and momentum were smaller than $O(10^{-8})$ at each time step. Lenormand *et al.* (2000) performed the LES of compressible periodic channel flow, and reported that the mass flux was conserved within 0.01% in the long-term integration using the driving force based on the mass flux.

2.7 Summary of Present DNS Algorithm

The present algorithm for compressible turbulent channel flow is summarized in the following (see also Morinishi *et al.* 2001*a*). First, the Fourier coefficient $\hat{\phi}^{\dagger}{}_{k_1k_3}(x_2^{\dagger})$ of the variable $\phi^{\dagger}(=\rho^{\dagger},\ u_1^{\dagger},\ u_2^{\dagger},\ u_3^{\dagger}$ and $T^{\dagger})$ at the new time is solved by the time integration of (2.20). The RHS of (2.20) is evaluated by the pseudo-spectral method in the x_1 and x_2 directions and by the B-spline collocation method in the x_2 direction. The skew-symmetric form (2.18) is used. Second, the coefficient of B-spline interpolation $\phi^{\dagger}_{jk_1k_3}$ is obtained by calculating (2.27). The coefficient $\phi^{\dagger}_{jk_1k_3}$ is used for the calculations of a wall-normal derivative in the RHS of (2.20) (see Appendix B.2). The variable $\phi^{\dagger}$ in physical space is obtained by (2.19). Note that the temperature $T^{\dagger}$ in physical space for the flow which includes the adiabatic wall is solved by (2.19) and (2.21). The series of operations is carried out repeatedly, and the time-dependent variables are advanced with the third-order compact storage Runge–Kutta method.

On the other hand, we briefly explain the numerical method to solve the continuity, momentum and energy equations (see (A.10)–(A.12)) for incompressible turbulent channel flows as follows (see also Morinishi *et al.* 2001*b*). The Chebyshev-tau method is used in the wall-normal direction, and the Fourier Galerkin method is used in the streamwise and spanwise directions (see Canuto *et al.* 1988). The continuity and Navier–Stokes equations are solved by the modified Kleiser–Schumann method (Kleiser & Schumann 1980; Werne 1995). The skew-symmetric form for convection term is used for the stable numerical simulation. The semi-implicit time marching algorithm is used where the diffusion

term is treated implicitly with the Crank–Nicolson scheme, and the third order Runge–Kutta scheme is used for all other terms. We confirmed the validity of the present code for the incompressible turbulent channel flow, comparing our results with those of existing DNS of incompressible turbulent channel flow (Kim & Moin 1989; Horiuti 1992).

2.8 Numerical Conditions

The non-dimensional parameters for the present simulations of compressible turbulent channel flows (Cases 1 and 2) are the Reynolds number $Re = 3000$, the Mach number $M = 1.5$, the Prandtl number $Pr = \mu c_p/\kappa = 0.72$, and the ratio of specific heats $\gamma = c_p/c_v = 1.4$ (where κ is thermal conductivity, μ is molecular viscosity, c_p is specific heat at constant pressure, and c_v is specific heat at constant volume). The Reynolds number, $Re = \rho_m U_m H/\mu_{iw}$, is based on the bulk density, bulk velocity, channel half-width, and viscosity at the isothermal wall, and the Mach number, $M = U_m/\left(\gamma R T_{iw}\right)^{1/2}$, is based on the bulk velocity and sound speed at the isothermal wall. The low-Reynolds and low-Mach numbers do not make the present analysis useless, because our goal is to clarify the difference and similarity between compressible turbulent flows near adiabatic and isothermal walls. The viscosity is given by Sutherland's law (see (2.7)), where $S_1 = 110.4$[K] and $T_{iw} = 293.15$[K].

The non-dimensional parameters for the present simulations of incompressible turbulent channel flow with passive scalar transport (Cases A and B) are the Reynolds number $Re_\tau = 150$ and the Prandtl number $Pr = 0.72$. The Reynolds number, $Re_\tau = u_\tau H/\nu$, is based on the friction velocity, the channel half-width, and the kinematic viscosity. Note that the Reynolds number Re_τ is given by $Re_\tau = \rho_w u_\tau H/\mu_w$ for compressible turbulent flow, where the friction velocity is defined as $u_\tau = (\tau_w/\rho_w)^{1/2}$ and τ_w is the wall shear stress.

The initial condition for Case 1 is as follows. The mean streamwise velocity is given by superimposing random velocity fluctuations upon the profile based on Spalding's law (see Spalding 1961). The wall-normal and spanwise velocity

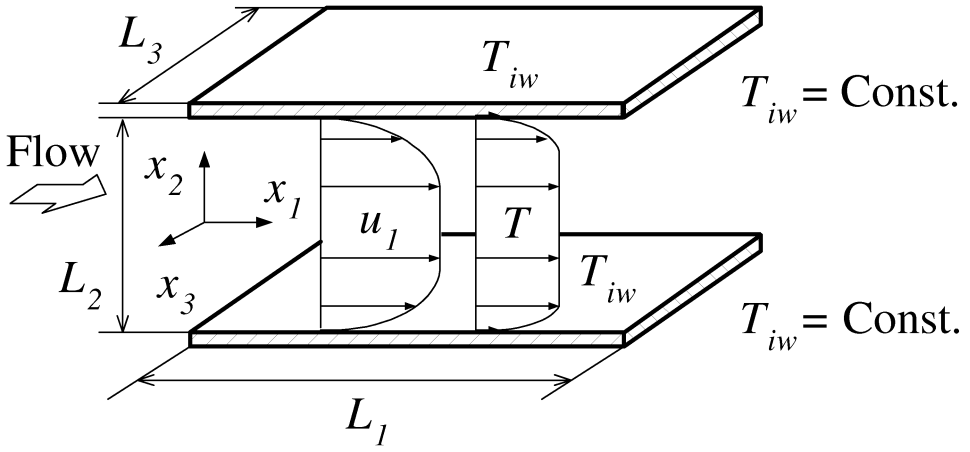

(a) Flow between isothermal walls

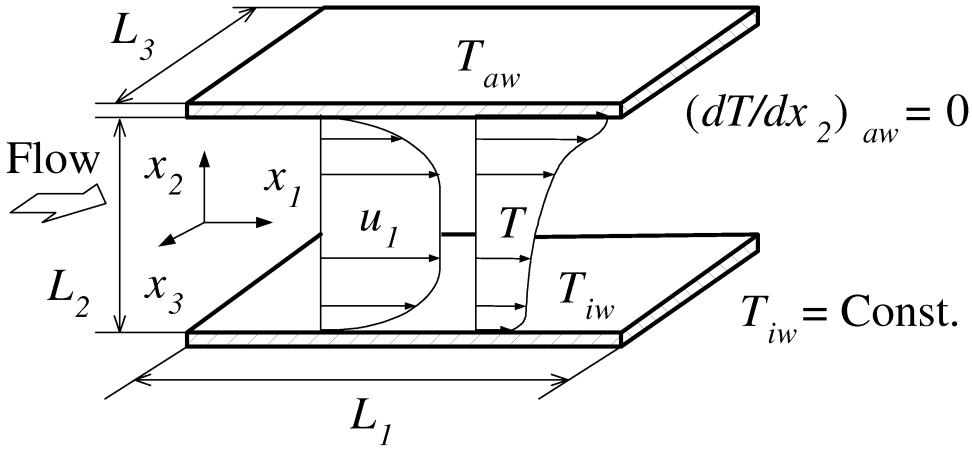

(b) Flow between adiabatic and isothermal walls

FIGURE 2.1. Computational cases: (a) Case 1 or A and (b) Case 1 or B.

components are given as random fluctuations with zero mean values. The RMS of velocity fluctuation is given by the function of the mean distribution and the amplitude of the random variable goes to zero as the wall is approached. The temperature and density fluctuations are zero, and their mean values are uniform: $\langle\rho\rangle_{x_1-x_3}/\rho_m = 1$ and $\langle T\rangle_{x_1-x_3}/T_{iw} = 1$. The initial field for Case 2 is a flow field of Case 1. A smoothing of density in the wall-normal direction is done for Case 2 a few times soon after the temperature boundary condition is changed from the isothermal wall to the adiabatic wall, because the sudden change causes unphysical oscillation.

TABLE 2.1. Classification of computational cases corresponding to thermal wall boundary conditions.

	Compressible		Incompressible	
Computational cases	Case 1	Case 2	Case A	Case B
Near isothermal wall	Case 1IW	Case 2IW	Case AIW	Case BIW
Near adiabatic wall	–	Case 2AW	–	Case BAW

TABLE 2.2. Physical simulation parameters.

Case	Re	Re_τ	M	Pr	γ
1	3000	(218)	1.5	0.72	1.4
2	3000	$(86.4 - 279)$	1.5	0.72	1.4
A	(2291)	150	–	0.72	–
B	(2291)	150	–	0.72	–
Coleman *et al.*	3000	(222)	1.5	0.7	1.4

The no-slip wall boundary condition is used for all cases. The Dirichlet or Neumam boundary condition of the density is not imposed, instead the continuity equation is solved at the wall with keeping the bulk density constant. The upper and lower walls of Case 1 are isothermal, and their temperatures are the same. The upper and lower walls of Case 2 are adiabatic and isothermal, respectively. The wall boundary conditions of Cases A and B correspond to those of Cases 1 and 2, respectively.

The computational domains and wall boundary conditions of temperature are shown in figure 2.1. The classification of the computational cases corresponding to thermal wall boundary conditions is shown in table 2.1. Cases 1IW, 2IW and 2AW represent the isothermal wall side of Case 1, the isothermal wall side of Case 2 and the adiabatic wall side of Case 2, respectively. Cases AIW, BIW and BAW represent the isothermal wall side of Case A, the isothermal wall side of Case B and the adiabatic wall side of Case B, respectively.

TABLE 2.3. Numerical simulation parameters.

Case	$L_1 \times L_2 \times L_3$	$N_1 \times N_2 \times N_3$
1	$4\pi H \times 2H \times 4\pi H/3$	$120 \times 180 \times 120$
2	$4\pi H \times 2H \times 4\pi H/3$	$120 \times 240 \times 120$
A	$4\pi H \times 2H \times 4\pi H/3$	$128 \times 129 \times 128$
B	$4\pi H \times 2H \times 4\pi H/3$	$128 \times 129 \times 128$
Coleman *et al.*	$4\pi H \times 2H \times 4\pi H/3$	$144 \times 119 \times 80$

Grid spacing in the periodic directions is uniform for all cases. The wall-normal collocation points x_2^i are distributed by using a hyperbolic-tangent function for Cases 1 and 2,

$$\frac{x_2^i}{H} = \frac{\tanh\left[G\left(2(i-1)/(N_2-1)-1\right)\right]}{\tanh\left(G\right)}, \quad (i = 1, \cdots, N_2) \tag{2.36}$$

where G is 2.0. The wall-normal grid points are given by Gauss–Lobatto points (see Canuto *et al.* 1988) for Cases A and B.

The physical and numerical parameters for all cases are given in tables 2.2 and 2.3, respectively. (N_1, N_2, N_3) and (L_1, L_2, L_3) are the number of grid points and computational region in the x_1, x_2 and x_3 directions, respectively. In the tables, parameters of Coleman *et al.* (1995) are also presented for comparison.

The eighth order B-spline, which has enough resolving power (see Appendix B.3), is used for Cases 1 and 2. The statistics are obtained by averaging over space (x_1 and x_3 directions) and time after the turbulent flows become stationary. The acoustic Courant number is defined as

$$AC = \left[\frac{|u_1| + a}{\Delta x_1} + \frac{|u_2| + a}{\Delta x_2} + \frac{|u_3| + a}{\Delta x_3}\right] \Delta t, \tag{2.37}$$

where $a = (\gamma RT)^{1/2}$ is acoustic speed, Δt is time increment, and $\Delta x_i (i = 1, 2, 3)$ is grid spacing in the x_i direction, respectively. The acoustic Courant numbers for Cases 1 and 2 are smaller than 0.43 and 0.36, respectively.

The time-averaged data for Cases 1 and 2 and Coleman *et al.* (1995) are summarized in Table 2.4. Reynolds number based on variables at the center of

TABLE 2.4. Time-averaged results.

Case	Re_τ	Re_c	$-B_q$	M_c	M_τ	u_τ/U_m	C_f	Nu
1IW	218	2717	0.048	1.502	0.080	0.0533	7.7×10^{-3}	39
2IW	279	2344	0.059	1.326	0.077	0.0517	9.6×10^{-3}	30
2AW	86.4	2344	0	1.326	0.071	0.0741	8.0×10^{-3}	0
Coleman *et al.*	222	2760	0.049	1.502	0.082	0.0545	8.1×10^{-3}	-

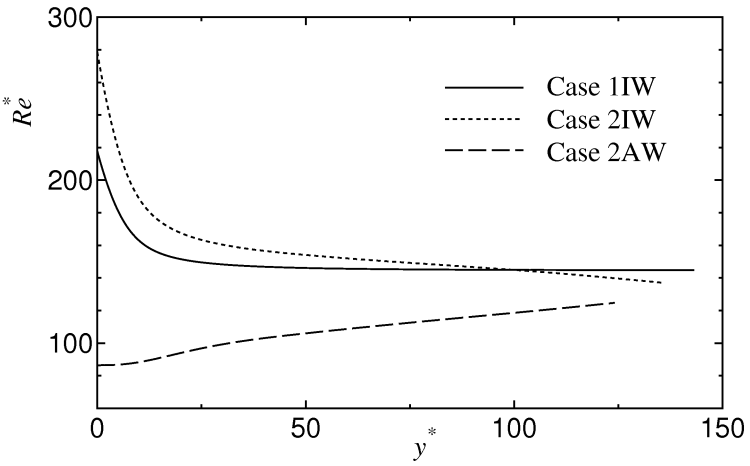

FIGURE 2.2. Profiles of Reynolds number Re^*_τ.

channel, Re_c, non-dimensional heat flux, B_q, Mach number based on velocity and sound speed at the center, M_c, friction Mach number based on friction velocity and wall sound speed, M_τ, skin friction coefficient, C_f, and Nusselt number, N_u, are respectively defined as follows: $Re_c = \rho_c u_{1c} H/\mu_c$, $B_q = q_w/(\rho_w c_p u_\tau T_w)$, $C_f = 2\tau_w/(\rho_m U_m^2)$, $M_c = u_{1c}/a_c$, $M_\tau = u_\tau/a_w$, $Nu = 2Hq_w/\kappa_w(T_w - T_m)$, where q_w is wall heat flux, τ_w is wall stress, T_m is bulk temperature, and $(\ )_c$ is value at the center of channel. The results of Case 1 are almost the same as those of Coleman *et al.* (1995). The non-dimensional heat flux B_q is zero at the adiabatic wall because of no heat flux, and it is negative at the isothermal wall since the heat is transported out of the isothermal wall, i.e. the flow is cooled at the isothermal wall.

TABLE 2.5. Grid resolution.

Case	Δx_1^+	Δx_2^+	Δx_3^+	Δx_1^*	Δx_2^*	Δx_3^*
1IW	23	0.36–5.1	7.6	15–23	0.36–3.4	5.1–7.6
2IW	9.1	0.11–1.5	3.0	9.1–13	0.11–2.2	3.0–4.4
2AW	29	0.35–4.8	9.7	14–29	0.35–2.4	4.8–9.7
A (B)	15	0.045–3.7	4.9	15	0.045–3.7	4.9

The grid resolution is evaluated by using not only the Reynolds number based on the friction velocity, Re_τ, but also the Reynolds number based on the semi-local friction velocity ($u_{\tau *} = (\tau_w / \langle \rho \rangle)^{1/2}$), $Re_\tau^* = \langle \rho \rangle u_{\tau *} H / \langle \mu \rangle$, where $\langle \ \rangle$ represents the Reynolds average over time and the x_1 and x_3 directions. Profiles of Re_τ^* for Cases 1IW, 2IW and 2AW are shown in figure 2.2. The semi-local wall unit, $y^* = \langle \rho \rangle u_{\tau *} y / \langle \mu \rangle$, is used in the figure, instead of wall unit, $y^+ = \rho_w u_\tau y / \mu_w$. Grid resolution based on wall and local variables for the present simulations is shown in table 2.5. The velocity field for Cases A and B does not depend on the temperature field, so the resolution of Case B is the same as that of Case A. The resolution of Cases 1 and 2 is comparable with that of Coleman *et al.* (1995) and Guarini *et al.* (2000) for compressible turbulent flow. The resolution of Cases A and B is better than that of Kim & Moin (1989) and Horiuti (1992) for incompressible turbulent flow. The streamwise resolution near the isothermal wall for compressible turbulent flow seems to be lower than that of incompressible turbulent channel flow. However, when local scaling is used, the resolution of compressible turbulent flow is comparable with that of incompressible turbulent flow.

2.9 Spectra and Two-point Correlations

The grid numbers and domain sizes must be chosen in such a way that all the relevant scales are resolved. The determination of proper resolution and domain size of the simulation is accomplished by analyzing the one-dimensional

(1D) energy spectra and two-point correlations, respectively. The 1D energy spectrum is a good indication for the smaller scales. If the simulation is well-resolved, then the energy spectrum should show several decades of decay and very little pipe up of energy at higher wave numbers. For the large scales, the domain size is most important. The domain size selected must be large enough to contain the largest structure that is encountered in the simulation. Then, the two-point correlation should go to zero within the domain.

The streamwise and spanwise energy spectra are

$$E_{\phi\phi}(k_1, x_2) = \left\langle \hat{\phi}_{k_1 k_3}(x_2)\ \overline{\hat{\phi}}_{k_1 k_3}(x_2) \right\rangle_{x_3 - t}, \tag{2.38}$$

$$E_{\phi\phi}(k_3, x_2) = \left\langle \hat{\phi}_{k_1 k_3}(x_2)\ \overline{\hat{\phi}}_{k_1 k_3}(x_2) \right\rangle_{x_1 - t}, \tag{2.39}$$

where $\overline{(\ )}$, $\langle\ \rangle_{x_1-t}$, and $\langle\ \rangle_{x_3-t}$ represent the complex conjugate, average over time and x_1 direction, and average over time and x_3 direction, respectively. Figure 2.3(a,c) shows the streamwise 1D energy spectra $E_{\phi\phi}(k_1, x_2)$ for Case 1, and figure 2.3(b,d) shows the spanwise 1D energy spectra $E_{\phi\phi}(k_3, x_2)$ for Case 1. Figure 2.4(a,c,e) shows the streamwise 1D energy spectra $E_{\phi\phi}(k_1, x_2)$ for Case 2, and figure 2.4(b,d,f) shows the spanwise 1D energy spectra $E_{\phi\phi}(k_3, x_2)$ for Case 2. The 1D energy spectra $E_{\phi\phi}$ are examined at the center of the channel for Cases 1 and 2, near the isothermal wall of Cases 1 and 2, and near the adiabatic wall of Case 2. All the 1D energy spectra in the region of high wave numbers are gradually decreasing, and the magnitude of $E_{\phi\phi}$ between the smallest and the largest wave number has dropped off by 3–4 orders. Moreover, the 1D energy spectra $E_{\phi\phi}$ of the present simulations are also comparable with those of Coleman *et al.* (1995) and Guarini *et al.* (2000). We therefore conclude that the resolutions of Cases 1 and 2 are sufficient.

The streamwise and spanwise two-point correlations are

$$R_{\phi\phi}(r_1, x_2) = \frac{\langle \phi'(x_1, x_2)\ \phi'(x_1 + r_1, x_2) \rangle}{\langle \phi'^2 \rangle}, \tag{2.40}$$

$$R_{\phi\phi}(r_3, x_2) = \frac{\langle \phi'(x_3, x_2)\ \phi'(x_3 + r_3, x_2) \rangle}{\langle \phi'^2 \rangle}, \tag{2.41}$$

where r_1 and r_3 represent separations in the x_1 and x_3 directions, respectively.

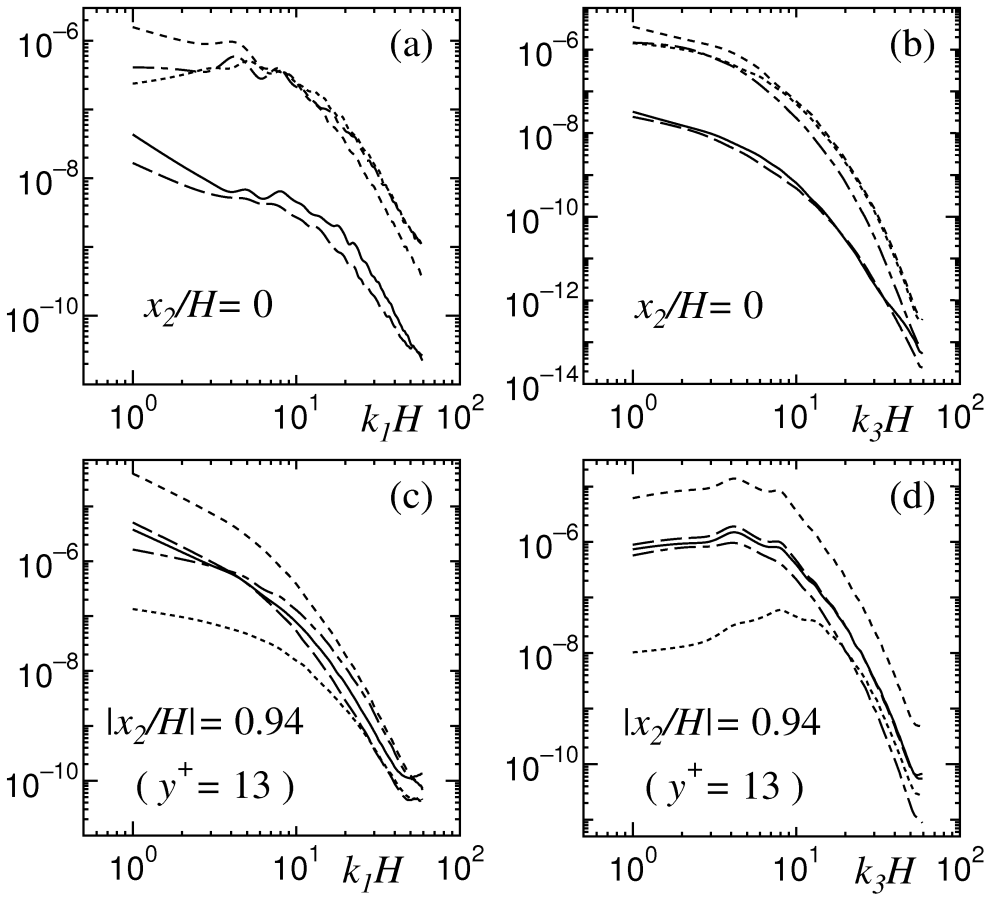

FIGURE 2.3. One-dimensional energy spectra for Case 1; ———, ρ ; - - - -, u_1 ; $\cdots\cdots$, u_2 ; – - –, u_3 ; — — —, T. (a,c) streamwise; (b,d) spanwise.

The streamwise two-point correlations $R_{\phi\phi}(r_1, x_2)$ and the spanwise two-point correlations $R_{\phi\phi}(r_3, x_2)$ for Cases 1 and 2 are shown in figures 2.5 and 2.6, respectively. The two-point correlations $R_{\phi\phi}$ are calculated at the same wall-normal positions as those of the 1D energy spectra $E_{\phi\phi}$. Figure 2.5(c) shows that the spanwise two-point correlation of density at the center of the channel is high for Case 1. This tendency was also observed in the simulation of Coleman *et al.* (1995). They argued that it was caused by acoustic resonance and did not affect other statistics. No serious problems caused by the acoustic effect appear in the results of Cases 1 and 2 (see the subsequent chapters). The other two-point correlations reach zero within the domain size, therefore it is proven that the computational domains of Cases 1 and 2 are sufficient.

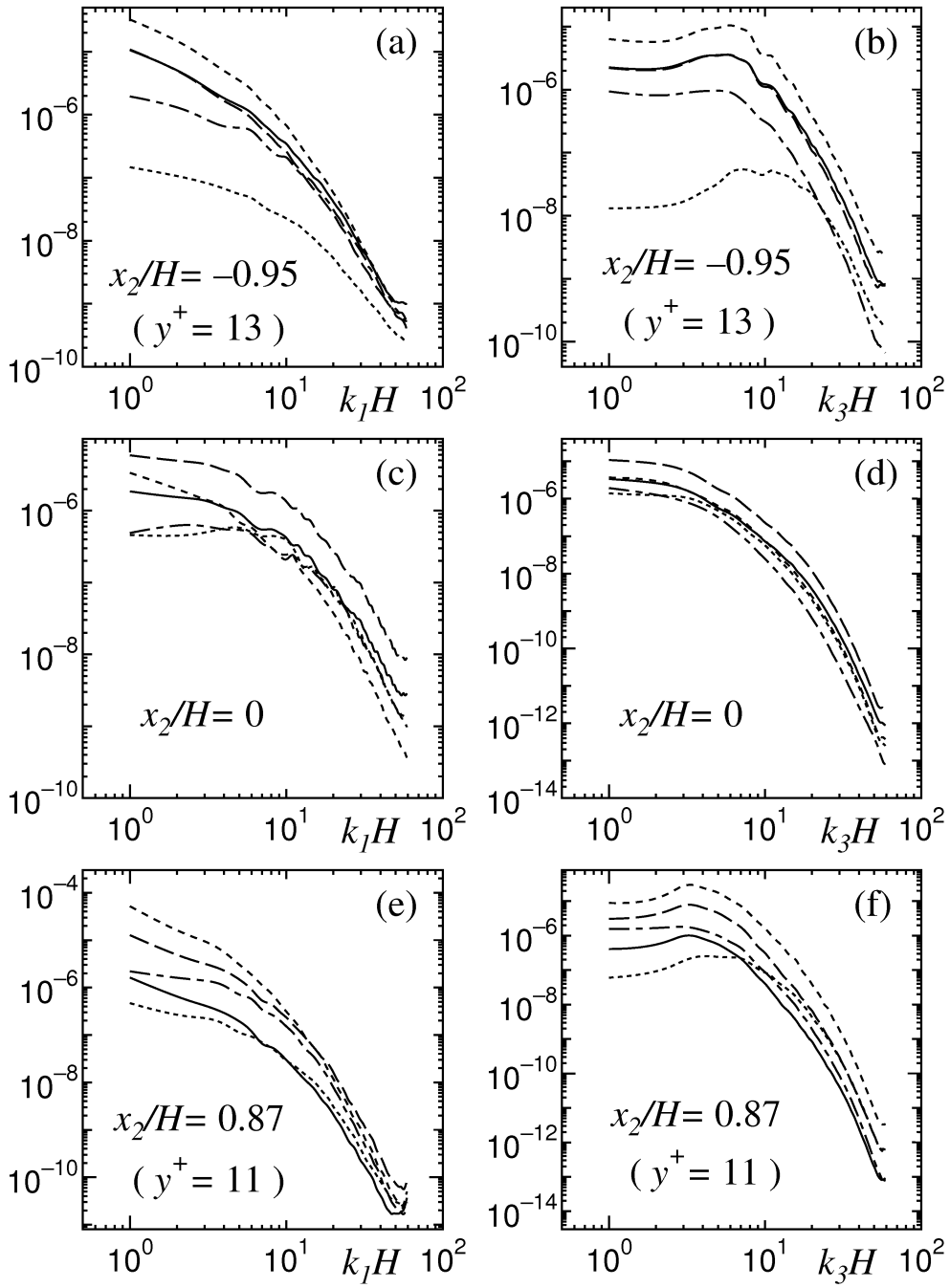

FIGURE 2.4. One-dimensional energy spectra for Case 2; lines as figure 2.3. (a, c, e) streamwise; (b, d, f) spanwise.

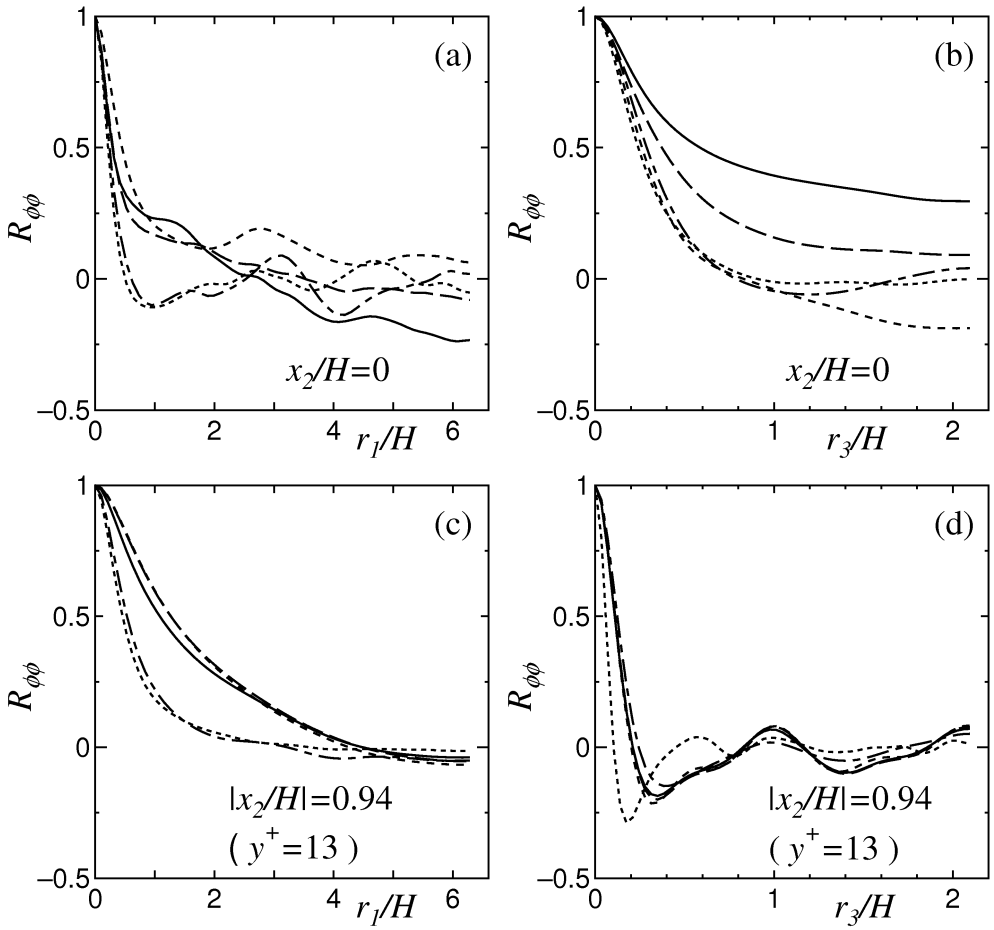

FIGURE 2.5. Two-point correlations for Case 1; lines as figure 2.3. (a, c) streamwise; (b, d) spanwise.

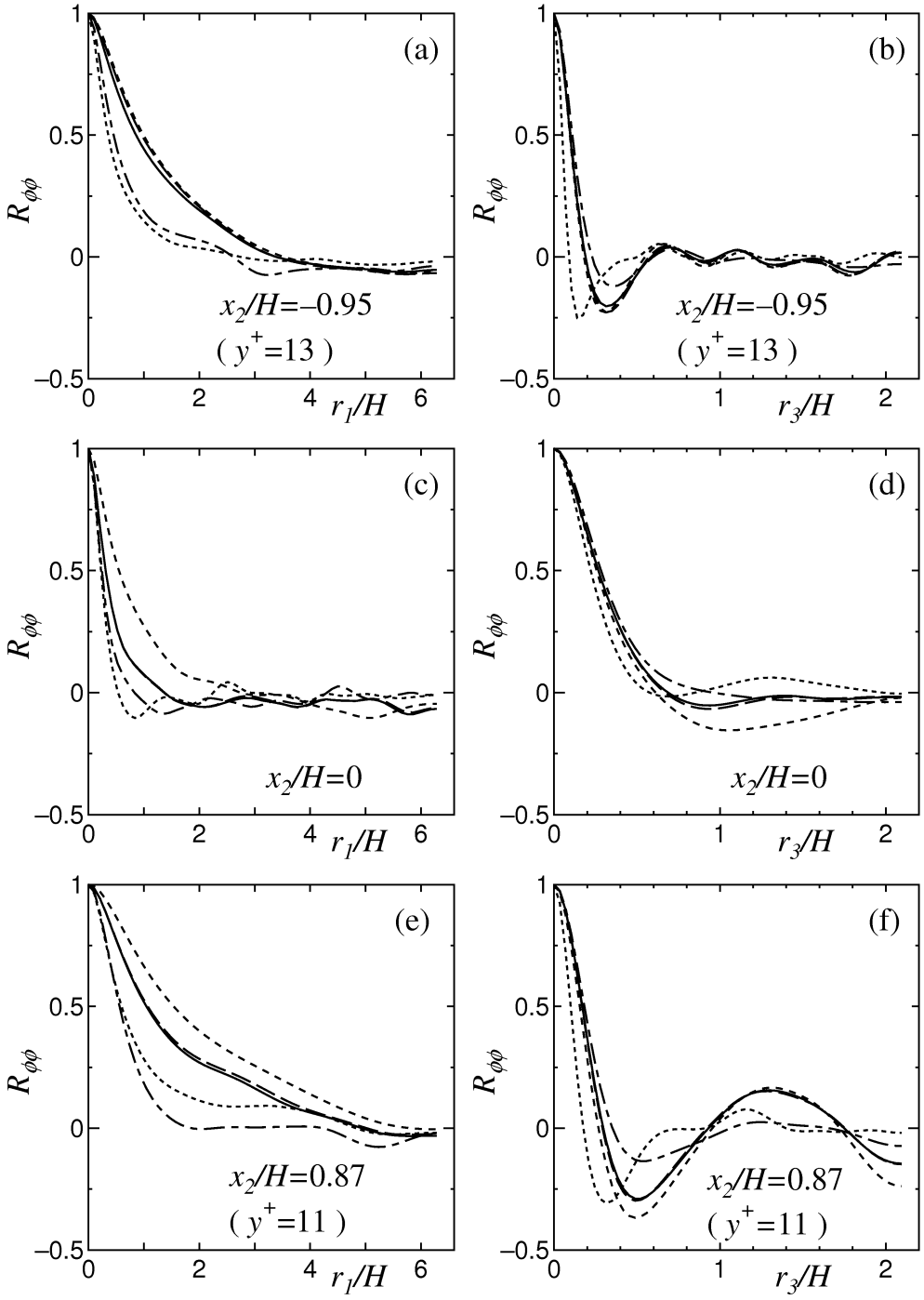

FIGURE 2.6. Two-point correlations for Case 2; lines as figure 2.3. (a, c, e) streamwise; (b, d, f) spanwise.

2.10 Comparison of Skew-symmetric and Advective Forms

The effect of the present skew-symmetric form (see (2.18)) is shown by comparing it with the advective form. To clarify the difference between these two forms, the simulations with poor grid resolutions in the periodic directions are carried out ($N_1 = N_3 = 32$ for Case 1-32, $N_1 = N_3 = 60$ for Case 1-60). The initial field is given by interpolating the fully developed turbulent flow of Case 1 ($N_1 = N_3 = 120$). The numerical conditions of Cases 1-32 and 1-60 are the same as those of Case 1 except for the grid number. The simulations for Cases 1-32 and 1-60 are carried out by using the skew-symmetric and advective forms respectively for the convection term. Table 2.6 summarizes the results for the simulations of Cases 1-32 and 1-60. The simulation with the advective form diverged for Case 1-32 after about 10,000 time steps, while those with the skew-symmetric form were stable for Cases 1-32 and 1-60. The simulation with the advective form was possible for Case 1-60, but its results were aliased.

Figure 2.7 shows the streamwise 1D energy spectra of temperature for the skew-symmetric and advective forms of Case 1-60 at 3,000 time steps after the interpolation. The result with the advective form has a large aliasing error at the largest wave number. On the other hand, the result with the skew-symmetric form is less aliased. These numerical tests lead to the conclusion that stable and low cost simulations can be done with the skew-symmetric form. Moreover, the 1D energy spectra for Cases 1 and 2 with the skew-symmetric form were gradually decreasing (see figures 2.3 and 2.4), therefore the usefulness of the present skew-symmetric form is verified.

TABLE 2.6. Comparison of advective and skew-symmetric forms for convection term: ↑, Diverged; △, Aliased; ◯, Stable.

Type of convection term	Case 1-32	Case 1-60
Advective form	↑	△
Skew-symmetric form	◯	◯

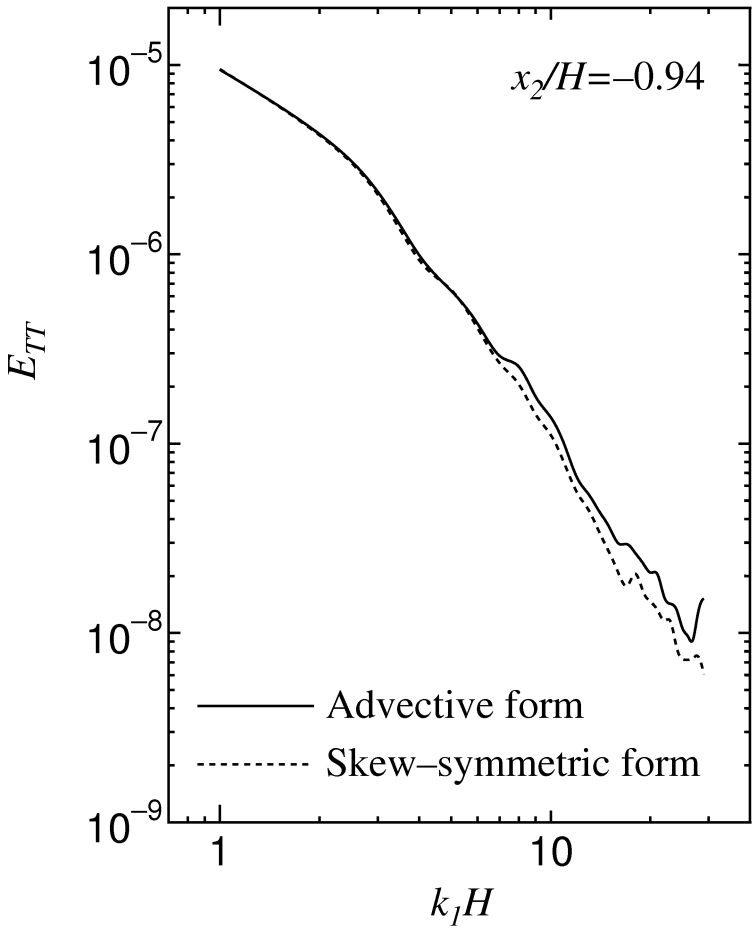

FIGURE 2.7. One-dimensional Fourier spectra of temperature for Case 1-60.

2.11 Summary

In this chapter, the new DNS algorithm which can simulate the compressible turbulent channel flow between adiabatic and isothermal walls accurately and efficiently is explained in detail.

(1) It is explained that the present DNS algorithm based on the B-spline collocation method has the advantages that the numerical boundary condition is uniquely and accurately determined corresponding to the physical boundary, particularly, at the adiabatic wall.

(2) It is shown that the construction of the algorithm is simple and the numerical cost is much cheaper than that of the B-spline Galerkin method, comparing the number of the operation counts of a nonlinear term between the B-spline Galerkin and collocation methods for wall-bounded compressible turbulent flow.

(3) The skew-symmetric form which is suitable for the wall-bounded compressible flow is proposed for the convection term to maintain numerical stability. The usefulness of the proposed skew-symmetric form is confirmed by performing the simulations with poor grid resolutions in the periodic directions and by comparing the proposed one with the advective form.

(4) The reliability of the present DNS algorithm is confirmed by comparing our result with that of Coleman *et al.* (1995) for the compressible turbulent channel flow between isothermal walls. The applicability and usefulness of the present DNS algorithm is also confirmed by the stable implementation of DNS of the compressible turbulent channel flow between adiabatic and isothermal walls.

(5) It is confirmed that the present DNS data has sufficient resolution and domain size, examining the 1D energy spectra and two-point correlations.

Chapter 3.

Mean Velocity and Temperature Profiles

3.1 Outline

First of all, the effects of the non-dimensional heat flux and the friction Mach number on the wall law of the mean velocity and temperature are examined theoretically. Next, the mean velocity and temperature profiles near adiabatic and isothermal walls are investigated using the present DNS results. The scaling laws of mean velocity and temperature profiles are also discussed.

3.2 Wall Laws of Mean Velocity and Temperature

It is known from the dimensional analysis result that the mean velocity and temperature profiles depend on the non-dimensional heat flux, B_q, and the friction Mach number, M_τ, when the Prandtl number Pr and the ratio of specific heats γ are constants. Since Pr and γ are fixed in the present simulations, we consider the effects of parameters B_q and M_τ (see table 2.4) on the mean velocity and temperature profiles. Parameters B_q and M_τ strongly depend on the mean density as described later, and the variation in the mean density is generally large near the wall in compressible turbulent flow. In this section, the wall laws of the mean velocity and temperature profiles are examined using the non-dimensional parameters B_q and M_τ. Assuming the length scale of turbulence, $l_u = \kappa_u y$, and

the temperature length scale, $l_T = \kappa_T y$, the mixing length theory leads to the following equations, respectively (Rotta 1960; Bradshaw 1977).

$$\frac{d\langle u_1\rangle}{dy} = \frac{\left(\tau_w/\langle\rho\rangle\right)^{1/2}}{\kappa_u y} \tag{3.1}$$

$$\frac{d\langle T\rangle}{dy} = -\frac{\tau_w\langle u_1\rangle + q_w}{\langle\rho\rangle c_p\left(\tau_w/\langle\rho\rangle\right)^{1/2}\kappa_T y} \tag{3.2}$$

The viscous friction work, $\tau_w\langle u_1\rangle$, is induced from the fifth term on the right-hand side of equation (A.3), and it does not appear in incompressible turbulent flow with passive scalar transport (cf. (A.12) and (A.3)). Equation (3.1) leads to the following equation;

$$\left(\frac{\langle\rho\rangle}{\rho_w}\right)^{1/2}\frac{d\langle u_1\rangle^+}{dy^+} = \frac{1}{\kappa_u y^+} \ , \tag{3.3}$$

where $\langle u_1\rangle^+ = \langle u_1\rangle/u_\tau$ is the mean velocity scaled by the friction velocity. The Van Driest transformed velocity $\langle u_1\rangle^+_{VD}$ (see Van Driest 1951) is defined as

$$\langle u_1\rangle^+_{VD} = \int_0^{\langle u_1\rangle^+}\left(\frac{\langle\rho\rangle}{\rho_w}\right)^{1/2} d\langle u_1\rangle^+ . \tag{3.4}$$

From (3.3) and (3.4), the log-law of $\langle u_1\rangle^+_{VD}$ is obtained as

$$\langle u_1\rangle^+_{VD} = \frac{1}{\kappa_u}\ln y^+ + B, \tag{3.5}$$

where B is the additive constant. Assuming $\langle\rho\rangle = \rho_w$, the log-law of $\langle u_1\rangle^+$ is given by

$$\langle u_1\rangle^+ = \frac{1}{\kappa_u}\ln y^+ + B. \tag{3.6}$$

Note that the assumption of $\langle\rho\rangle = \rho_w$ is not successful in the present results (see figure 3.1(a)). Moreover, we consider whether the mean velocity scaled by the semi-local friction velocity, $\langle u_1\rangle^* = \langle u_1\rangle/u_{\tau *}$, provides the log-law. The assumption,

$$d\left(\langle\rho\rangle/\rho_w\right)^{1/2}/dy^+ \simeq 0, \tag{3.7}$$

yields the following log-law of $\langle u_1\rangle^*$.

$$\langle u_1\rangle^* = \frac{1}{\kappa_u}\ln y^+ + B \tag{3.8}$$

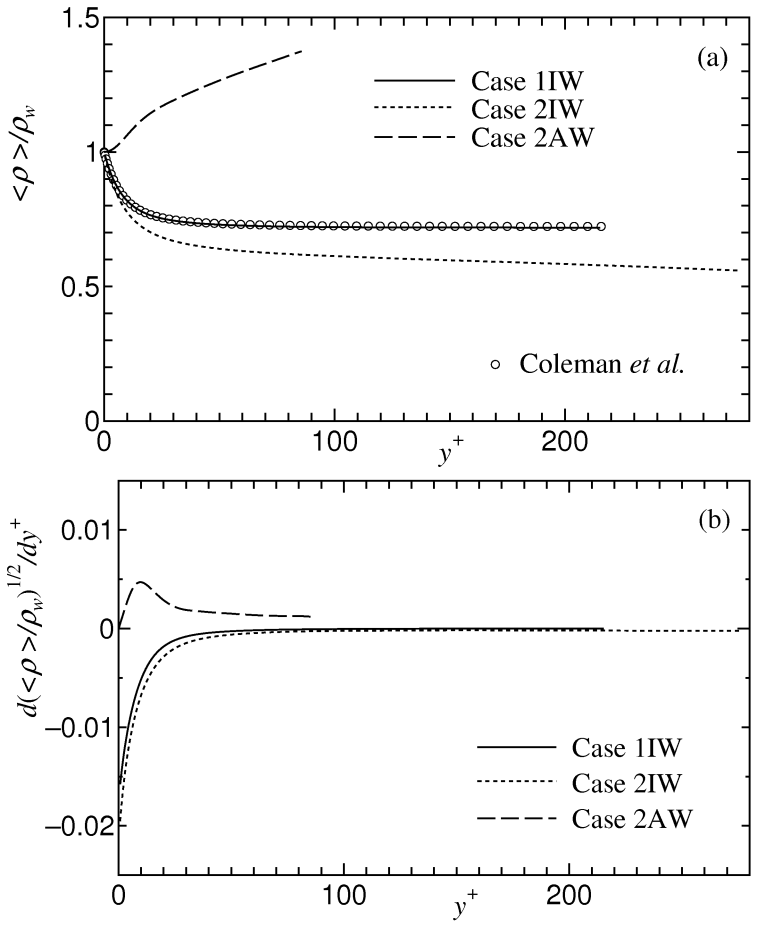

FIGURE 3.1. Mean profiles: (a) $\langle\rho\rangle/\rho_w$ and (b) $d\left(\langle\rho\rangle/\rho_w\right)^{1/2}/dy^+$.

Note that (3.7) is the assumption in the region of sufficiently large y^+ and does not correspond to $\langle\rho\rangle = \rho_w$. In the present simulations, the assumption (3.7) is satisfied in the range of $y^+ > 50$ for Cases 1IW and 2IW and is not successful for Case 2AW (see figure 3.1(b)). As pointed out by Coleman *et al.* (1995), if the semi-local wall variable, y^*, is used in (3.8) instead of the wall variable, y^+, the additive constant in (3.8), B, depends on the heat transfer and shear at the wall.

Next, in order to show the effects of B_q and M_τ on the mean velocities $\langle u_1\rangle^+_{VD}$, $\langle u_1\rangle^*$ and $\langle u_1\rangle^+$ explicitly, we use the relationship between $\langle T\rangle/T_w$ and $\langle u_1\rangle^+$ obtained from (3.1) and (3.2) (see Huang *et al.* 1994; Huang & Coleman

1994).

$$\frac{\langle T\rangle}{T_w} = 1 - Pr_t B_q \langle u_1\rangle^+ - Pr_t M_\tau^2 \frac{\gamma-1}{2}\langle u_1\rangle^{+2}, \tag{3.9}$$

where $Pr_t = \kappa_u/\kappa_T$ is the turbulent Prandtl number. Assuming that pressure given by the state equation (see (A.9)) is constant, it yields the relationship between density and temperature, $\langle\rho\rangle/\rho_w = T_w/\langle T\rangle$. The relationship between $\langle u_1\rangle^+_{VD}$ and $\langle u_1\rangle^+$ is given by

$$\langle u_1\rangle^+_{VD} = E^{1/2}\left[\arcsin\left(\frac{A+\langle u_1\rangle^+}{D}\right) - \arcsin\left(\frac{A}{D}\right)\right], \tag{3.10}$$

where $E = 2/[Pr_t M_\tau^2(\gamma-1)]$, $A = B_q/[(\gamma-1)M_\tau^2]$ and $D = (A^2+E)^{1/2}$ (see Huang & Coleman 1994). The relationship between $\langle u_1\rangle^*$ and $\langle u_1\rangle^+$ is given by

$$\langle u_1\rangle^* = \left[1 - Pr_t B_q \langle u_1\rangle^+ - Pr_t M_\tau^2 \frac{\gamma-1}{2}\langle u_1\rangle^{+2}\right]^{-1/2}\langle u_1\rangle^+. \tag{3.11}$$

The rearranged mean velocity in the standard wall-unit is given by

$$\langle u_1\rangle^+ = D\sin\left(\frac{1}{\kappa_u E^{1/2}}\ln\frac{y^+}{y_0^+}\right), \tag{3.12}$$

where $y_0^+ = \exp(-\kappa_u B)$ (see White 1991).

The effects of B_q and M_τ are investigated respectively as follows. In the case of $M_\tau = 0$, the mean velocities $\langle u_1\rangle^+$, $\langle u_1\rangle^+_{VD}$ and $\langle u_1\rangle^+$ are written by

$$\langle u_1\rangle^+ = \frac{1}{\kappa_u}\ln\frac{y^+}{y_0^+} - \frac{Pr_t B_q}{4\kappa_u^2}\ln^2\frac{y^+}{y_0^+}, \tag{3.13}$$

$$\langle u_1\rangle^+_{VD} = -\frac{2}{Pr_t B_q}\left[\left(1 - Pr_t B_q\langle u_1\rangle^+\right)^{1/2} - 1\right], \tag{3.14}$$

$$\langle u_1\rangle^* = \left[1 - Pr_t B_q\langle u_1\rangle^+\right]^{-1/2}\langle u_1\rangle^+, \tag{3.15}$$

respectively. We assume that $Pr_t = 0.9$, $\kappa_u = 0.4$ and $y_0^+ = \exp(-0.4\times 5.5) \simeq 0.1108$ for simplicity. In the case of $B_q = M_\tau = 0$, the mean velocities $\langle u_1\rangle^+$, $\langle u_1\rangle^+_{VD}$ and $\langle u_1\rangle^*$ are the same as the log-law for the incompressible turbulent flow. In the case of $M_\tau = 0$, the mean velocities given by (3.13)–(3.15) in the range of $0.02 \le -B_q \le 0.12$ where the increment of $-B_q$ is 0.02, are shown in figure 3.2(a). The velocity $\langle u_1\rangle^+$ increases and $\langle u_1\rangle^*$ decreases with the increase

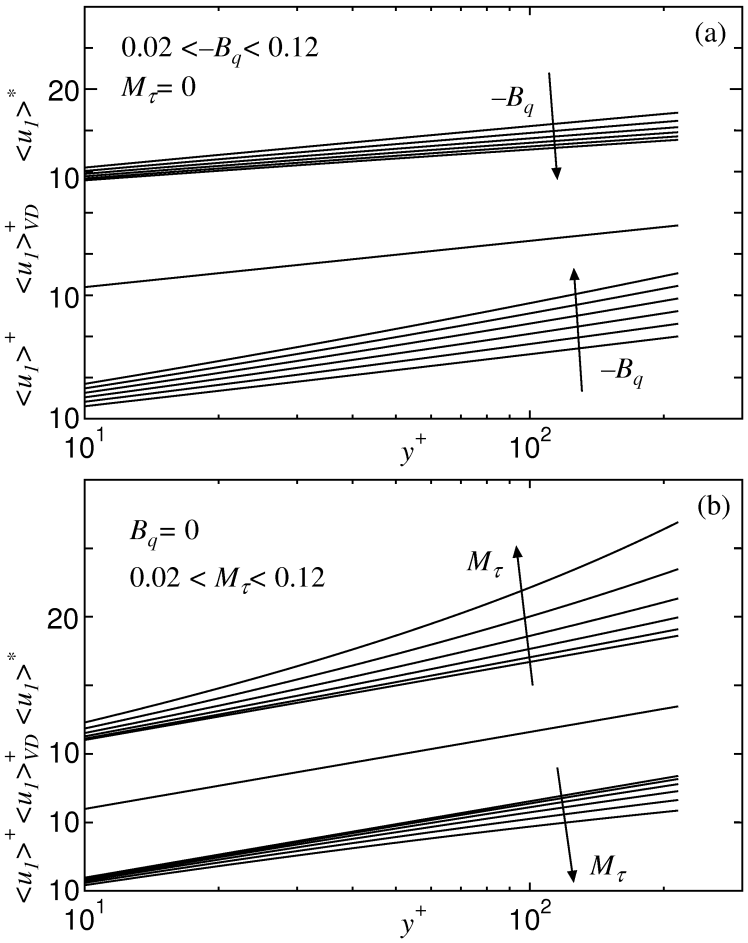

FIGURE 3.2. Mean velocity: (a) effects of B_q and (b) effects of M_τ.

of $-B_q$, respectively. The transformed velocity $\langle u_1 \rangle^+_{VD}$ is independent of $-B_q$. In the case of $B_q = 0$, the mean velocities $\langle u_1 \rangle^+$, $\langle u_1 \rangle^+_{VD}$ and $\langle u_1 \rangle^*$, are written by

$$\langle u_1 \rangle^+ = E^{1/2} \sin\left(\frac{1}{\kappa_u E^{1/2}} \ln \frac{y^+}{y_0^+}\right), \tag{3.16}$$

$$\langle u_1 \rangle^+_{VD} = E^{1/2} \arcsin\left(\frac{\langle u_1 \rangle^+}{E^{1/2}}\right), \tag{3.17}$$

$$\langle u_1 \rangle^* = \left[1 - Pr_t M_\tau^2 \frac{\gamma - 1}{2} \langle u_1 \rangle^{+2}\right]^{-1/2} \langle u_1 \rangle^+ . \tag{3.18}$$

In the case of $B_q = 0$, the mean velocities given by (3.16)–(3.18) in the range of $0.02 \leq M_\tau \leq 0.12$ where the increment of M_τ is 0.02, are shown in figure 3.2(b). The velocity $\langle u_1 \rangle^+$ decreases and $\langle u_1 \rangle^*$ increases with the increase of M_τ, respectively. The transformed velocity $\langle u_1 \rangle^+_{VD}$ is independent of M_τ.

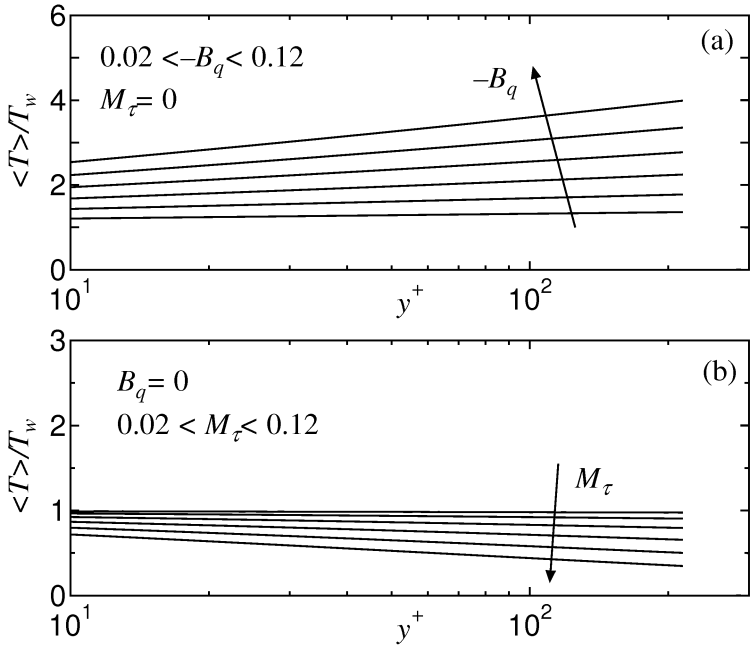

FIGURE 3.3. Variation of $\langle T\rangle/T_w$: (a) effects of B_q and (b) effects of M_τ.

Next, we show the effects of B_q and M_τ on the mean temperature profiles. In the case of $M_\tau = 0$, the mean temperature scaled by the wall temperature given by (3.9), $\langle T\rangle/T_w$, with the range of $0.02 \leq -B_q \leq 0.12$ is shown in figure 3.3(a). In the case of $B_q = 0$, the mean temperature $\langle T\rangle/T_w$ with the range of $0.02 \leq M_\tau \leq 0.12$ is shown in figure 3.3(b). The velocities $\langle u_1\rangle^+$ for $M_\tau = 0$ and $B_q = 0$ are given by (3.13) and (3.16), respectively. The mean temperature $\langle T\rangle/T_w$ increases with the increase of $-B_q$ and decreases with the increase of M_τ. The relationship between $\langle T\rangle^+ = (T_w - \langle T\rangle)/T_\tau$ and $\langle u_1\rangle^+$,

$$\langle T\rangle^+ = Pr_t \langle u_1\rangle^+ + Pr_t \frac{M_\tau^2}{B_q}\frac{\gamma-1}{2}\langle u_1\rangle^{+2}, \tag{3.19}$$

is obtained in the case of $B_q \neq 0$ which corresponds to the non-adiabatic wall. The friction temperature T_τ is defined as $T_\tau = B_q T_w$. In case of $M_\tau = 0$, equation (3.19) yields the similarity law of mean velocity and temperature, $\langle T\rangle^+ = Pr_t \langle u_1\rangle^+$. The mean temperature $\langle T\rangle^+$ with the range of $0.02 \leq -B_q \leq 0.12$ in the case of $M_\tau = 0$ is shown in figure 3.4(a). The mean temperature $\langle T\rangle^+$ with the range of $0.02 \leq M_\tau \leq 0.12$ in the case of $-B_q = 0.048$ is shown in

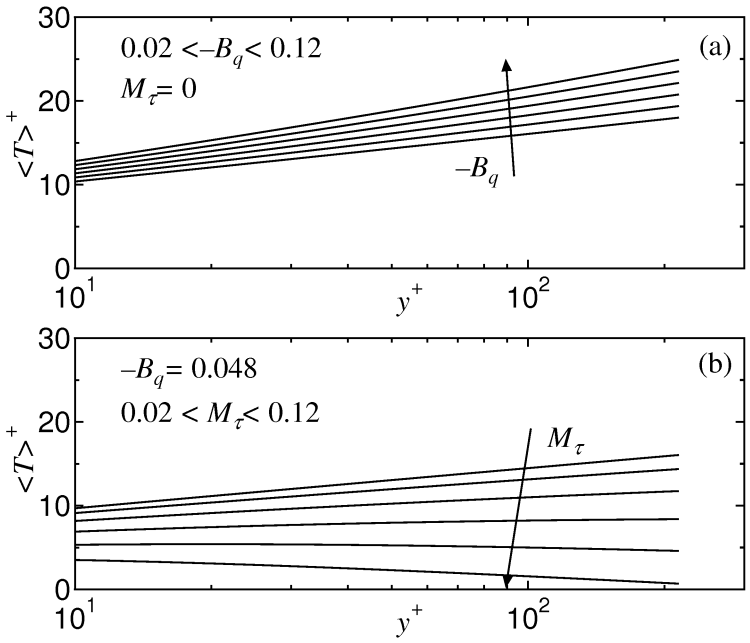

FIGURE 3.4. Variation of $\langle T \rangle^+$: (a) effects of B_q and (b) effects of M_τ.

figure 3.4(b). The velocities $\langle u_1 \rangle^+$ in the case of $M_\tau = 0$ and $-B_q = 0.048$ are given by (3.13) and (3.12), respectively. The mean temperature $\langle T \rangle^+$ increases with the increase of $-B_q$ and decreases with the increase of M_τ. Note that the mean temperature $\langle T \rangle^+$ depends on B_q even if M_τ is zero (see figure 3.4(a)), because the mean velocity $\langle u_1 \rangle^+$ depends on B_q in the case of $M_\tau = 0$. Here, the log-law of the mean temperature near the non-adiabatic wall in the compressible turbulent flow depends on the second term on the right-hand side of (3.19) which corresponds to the viscous friction work, and it can be usually neglected in incompressible turbulent flow. On the other hand, the log-law of the mean temperature for incompressible turbulent flow is

$$\langle T \rangle^+ = \frac{Pr_t}{\kappa_u} \ln y^+ + C, \tag{3.20}$$

where C is the additive constant (see White 1991). In the following sections, we shall explain the mean velocity and temperature profiles obtained from the present DNS results, using the analysis in this section.

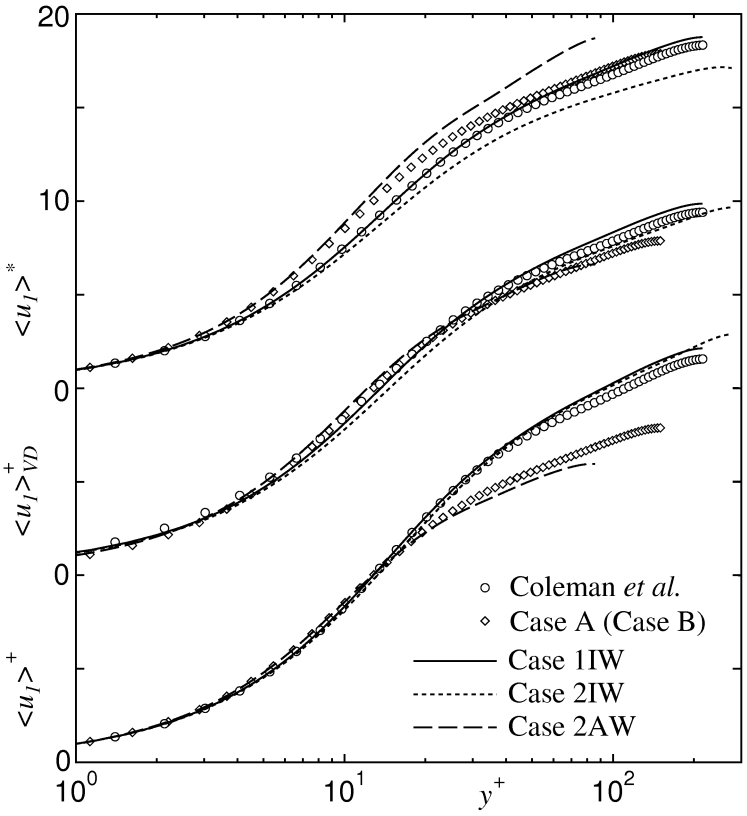

FIGURE 3.5. Mean velocity profiles: $\langle u_1 \rangle^+$, $\langle u_1 \rangle^+_{VD}$ and $\langle u_1 \rangle^*$.

3.3 Mean Velocity Profiles

Figure 3.5 shows the profiles of mean velocities $\langle u_1 \rangle^+$, $\langle u_1 \rangle^+_{VD}$ and $\langle u_1 \rangle^*$. The figure obviously shows that the Van Driest transformed velocity $\langle u_1 \rangle^+_{VD}$ agrees well with the data of the incompressible turbulent flow. Thus, the Van Driest transformation provides the most universal velocity profiles.

Next, the mean velocities $\langle u_1 \rangle^+$, $\langle u_1 \rangle^+_{VD}$ and $\langle u_1 \rangle^*$ for $y^+ \geq 20$, are compared under the same thermal boundary condition. The profiles of mean velocities for Cases 2IW and 2AW which correspond to the compressible turbulent flow near isothermal and adiabatic walls are shown in figure 3.6. Using the theoretical results of figure 3.2 and the numerical results of figure 3.6, the effects of the parameters B_q and M_τ on the mean velocity are summarized as follows. The Van Driest transformed mean velocity $\langle u_1 \rangle^+_{VD}$ of Cases 2IW and 2AW agrees well

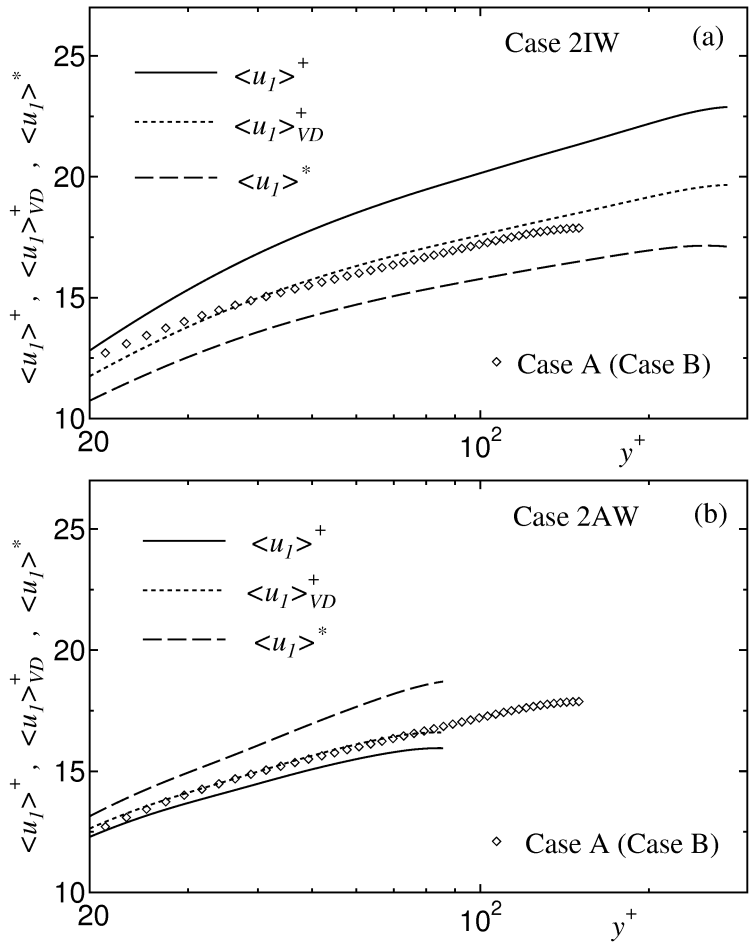

FIGURE 3.6. Profiles of mean streamwise velocity: (a) Case 2IW and (b) Case 2AW.

with the data of Case A, because $\langle u_1 \rangle^+_{VD}$ is independent of B_q and M_τ. The velocity $\langle u_1 \rangle^+$ of Case 2IW is larger than that of Case A. This is because the effect of B_q is larger than that of M_τ. The value of $\langle u_1 \rangle^+$ for Case 2AW is slightly smaller than that of Case A because of the effect of M_τ. Unlike $\langle u_1 \rangle^+$ of Case 2IW, $\langle u_1 \rangle^+$ of Case 2AW is close to that of Case A. This is probably caused by the influence of the low-Reynolds number effect near the adiabatic wall, as mentioned in the Introduction. We checked the profile of $y^+ d \langle u_1 \rangle^+ / dy^+$ and confirmed that the log-region of Case 2AW was very small. The log-law is not realized for $\langle u_1 \rangle^+$ of Cases 2IW and 2AW because of the failure of the assumption of $\langle \rho \rangle = \rho_w$. The velocity $\langle u_1 \rangle^*$ of Case 2IW is smaller than that of Case A. This

is because the effect of B_q is larger than that of M_τ. The value of $\langle u_1 \rangle^*$ for Case 2AW is much larger than that of Case A because of the effect of M_τ. The log-law of $\langle u_1 \rangle^*$ is not realized, because the assumption of (3.7) is not satisfied.

3.4 Mean Temperature Profiles

Profiles of mean temperature $\langle T \rangle / T_w$ are shown in figure 3.7(a). The temperature $\langle T \rangle / T_w$ for Case 2AW becomes smaller than unity, because of the effect of M_τ (see figure 3.3(b)). The values of $\langle T \rangle / T_w$ for Cases 1IW and 2IW become larger than unity, because the effect of B_q is larger than that of M_τ (see figure 3.3). The value of $\langle T \rangle / T_w$ for Case 2IW is larger than that of Case 1IW because $-B_q$ (=0.048) of Case 1IW is smaller than $-B_q$ (=0.059) of Case 2IW, and M_τ (=0.080) of Case 1IW is larger than M_τ (=0.077) of Case 2IW (see figure 3.3).

Profiles of mean temperature scaled $\langle T \rangle^+$ are given in figure 3.7(b). The temperatures $\langle T \rangle^+$ of the compressible turbulent flows (Cases 1IW and 2IW) are smaller than those of the incompressible turbulent flows (Cases AIW and BIW). The difference in $\langle T \rangle^+$ between Cases 1IW and 2IW is explained by figure 3.4, as well as the profiles of $\langle T \rangle / T_w$. The gradient of $\langle T \rangle^+$ for Cases 2IW and BIW is large near the centre of the channel, because they are influenced by the opposite wall which corresponds to the adiabatic wall.

Next, to clarify the logarithmic regions of velocity and temperature, the profiles of $y^+ d \langle u_1 \rangle^+ / dy^+$ and $y^+ d \langle T \rangle^+ / dy^+$ are investigated (see figure 3.8). The logarithmic regions of the velocity and temperature correspond to the regions where $y^+ d \langle u_1 \rangle^+ / dy^+ (= 1/\kappa_u)$ and $y^+ d \langle T \rangle^+ / dy^+ (= 1/\kappa_T)$ are constants, respectively. The logarithmic region of velocity is found for all cases, and the values of κ_u for Cases 1IW and 2IW are larger than for Case A. No logarithmic region of the mean temperature for Case 1IW can be seen in figure 3.8(b). Although a mimic logarithmic region is observed around the minimum point of $y^+ d \langle T \rangle^+ / dy^+$ for Cases 2IW and BIW, it is caused by the different thermal wall boundary condition on the opposite wall. Since the second term on right-

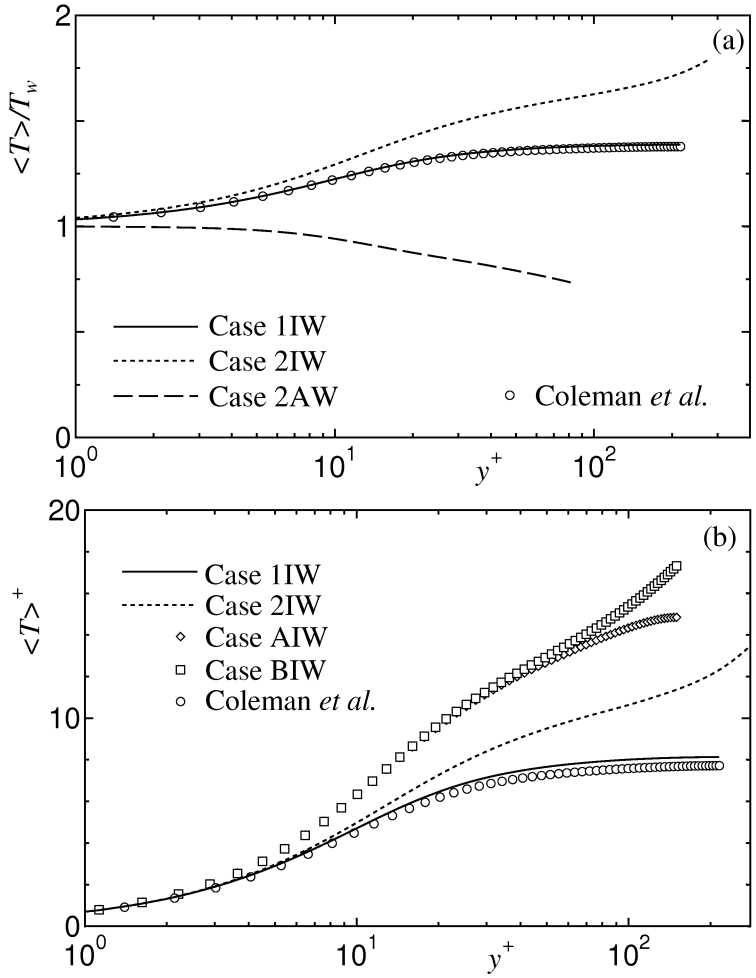

FIGURE 3.7. Profiles of (a) $\langle T \rangle / T_w$ and (b) $\langle T \rangle^+$.

hand side of (3.19) that corresponds to the viscous friction work is not zero for the compressible turbulent flow, the logarithmic region of temperature is not found for Cases 1IW and 2IW. The logarithmic region of temperature is not realized for Case AIW in spite of $M_\tau = 0$, because of the low-Reynolds number ($Re_\tau = 150$). The logarithmic region of the mean temperature appears for the incompressible turbulent channel flow with the higher Reynolds number (see Case CIW in figure 3.8(b)). Case CIW represents the isothermal wall side of Case C whose conditions are the same as those of Case A, except the Reynolds number, $Re_\tau = 300$, the grid numbers, (N_1, N_2, N_3)=(128, 161, 128), and computational domain sizes, (L_1, L_2, L_3)=$(2\pi H, 2H, 2\pi H/3)$.

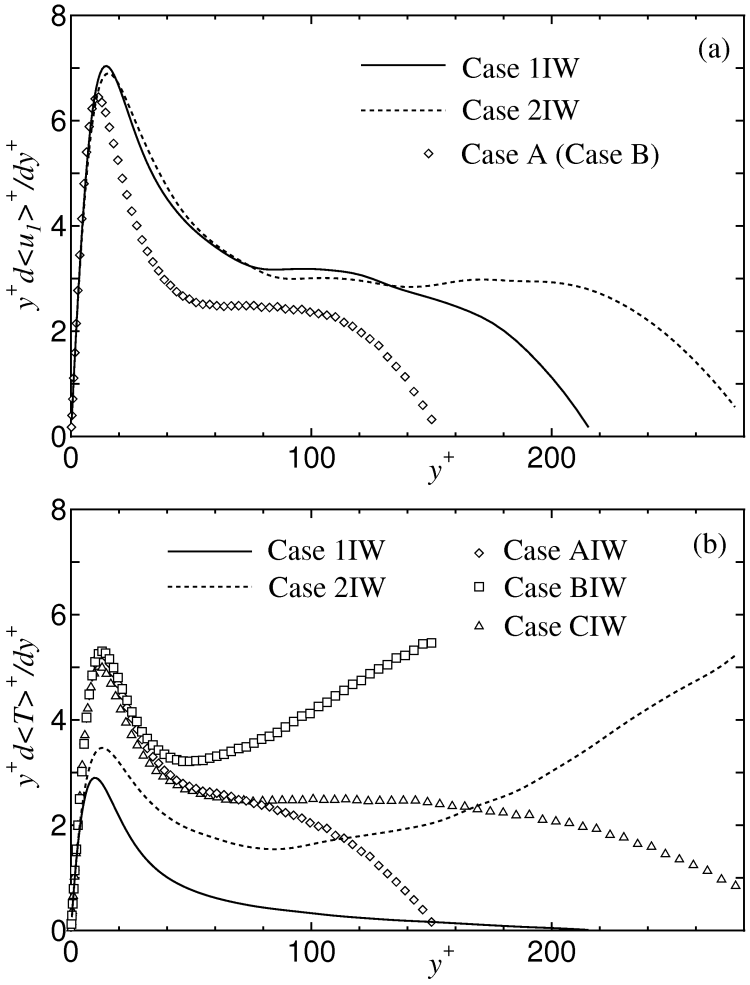

FIGURE 3.8. Similarity law of velocity and temperature (a) $y^+ d\langle u_1\rangle^+/dy^+$ and (b) $y^+ d\langle T\rangle^+/dy^+$.

3.5 Summary

In this chapter, the mean streamwise velocity and temperature profiles are investigated. The results are summarized as follows.

(1) The Van Driest transformation collapses the mean velocity profiles of the compressible turbulent flow near adiabatic and isothermal walls onto the log-law for the incompressible turbulent flow. This can be explained by the theoretical analysis result, i.e., the Van Driest transformed velocity is independent of non-dimensional heat flux B_q and the friction Mach number M_τ, while the untransformed velocity increases with an increase of $-B_q$ and decreases with an

increase of M_τ. The log-law of the mean velocity normalized by the semi-local friction velocity is not realized for compressible turbulent flows near both adiabatic and isothermal walls.

(2) The mean temperature profiles scaled by the wall and friction temperatures can be explained using the theoretical analysis result, i.e., the mean temperature increases with an increase of $-B_q$ and decreases with an increase of M_τ. And the difference of the mean temperature between compressible turbulent flows near isothermal and adiabatic walls is clarified.

(3) The logarithmic region of the mean temperature near the isothermal wall does not appear for compressible turbulent flow because of the effect of the viscous friction work, while the logarithmic region appears near the isothermal wall in incompressible turbulent flow.

Chapter 4.

Turbulence Statistics

4.1 Outline

First, the profiles of the RMS velocity fluctuations, the RMS density and temperature fluctuations, Reynolds shear stress and turbulent heat flux are discussed through the different normalizations for compressible turbulent flow. Second, the difference between the near-wall asymptotic behaviors of compressible and incompressible turbulent flows is investigated. Finally, the applicability and usefulness of the Reynolds analogy and the modified Reynolds analogy are examined using the present simulation results.

4.2 Profiles of Turbulence Statistics

The usefulness of the semi-local scaling is investigated by comparing the RMS velocity fluctuations scaled by the friction velocity, $(u'_\alpha)^+_{rms} = \langle u'_\alpha u'_\alpha \rangle^{1/2} / u_\tau$, with those scaled by the semi-local friction velocity, $(u'_\alpha)^*_{rms} = \langle u'_\alpha u'_\alpha \rangle^{1/2} / u_{\tau *}$, ($\alpha = 1, 2, 3$, no summation for α) (see figure 4.1). The streamwise intensities of turbulence for the compressible turbulent flow near the isothermal wall (Cases 1IW and 2IW) in the region of $y^+ \geq 10$, are larger than that of the incompressible turbulent flow (Case A). The streamwise intensity of turbulence for the compressible turbulent flow near the adiabatic wall (Case 2AW) in the region of $y^+ \geq 10$, is smaller than that of Case A. On the other hand, the semi-local scaling collapses the RMS velocity fluctuations of the compressible turbulent flow

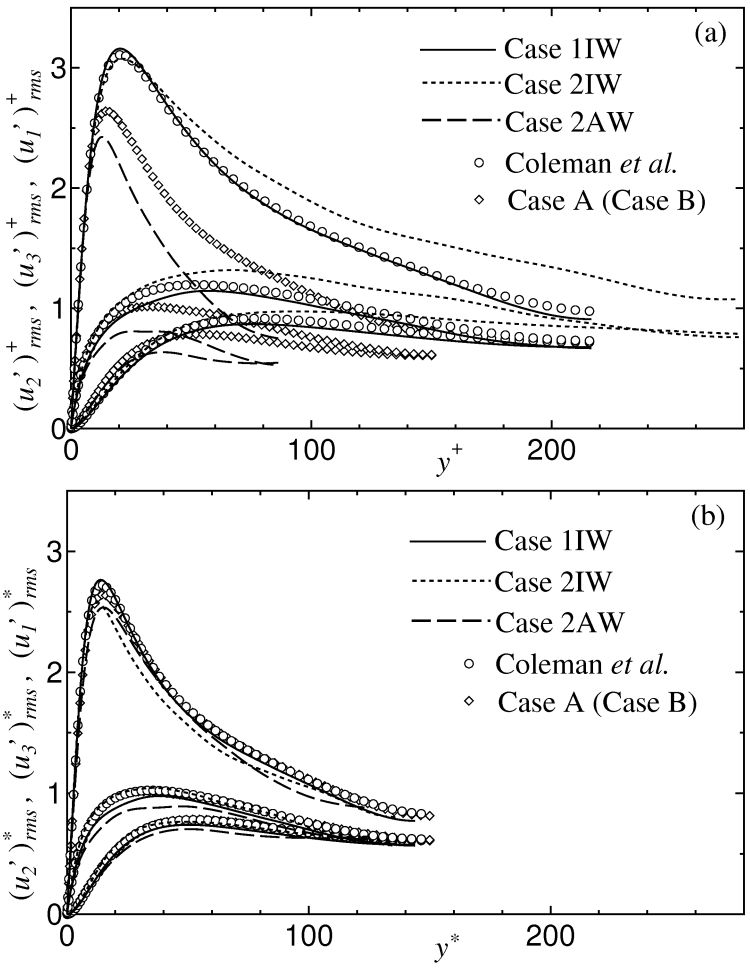

FIGURE 4.1. Profiles of RMS velocity fluctuations: (a) $(u'_\alpha)^+_{rms}$ ($\alpha = 1, 2, 3$) and (b) $(u'_\alpha)^*_{rms}$ ($\alpha = 1, 2, 3$).

onto those of the incompressible turbulent flow. Namely, Morkovin's hypothesis is satisfied in the RMS velocity fluctuations. However, the wall-normal and spanwise intensities of turbulence, $(u'_2)^*_{rms}$ and $(u'_3)^*_{rms}$, in the compressible turbulent flow near the adiabatic wall (Case 2AW) are slightly smaller than those of Case A, respectively. The same trend was also observed in the turbulent channel flow of $M = 0$ with variable properties between isothermal walls by Nicoud (1999). The difference may be caused by the low-Reynolds number effect (see Antonia *et al.* 1992).

The RMS density, temperature fluctuations and the relationship between

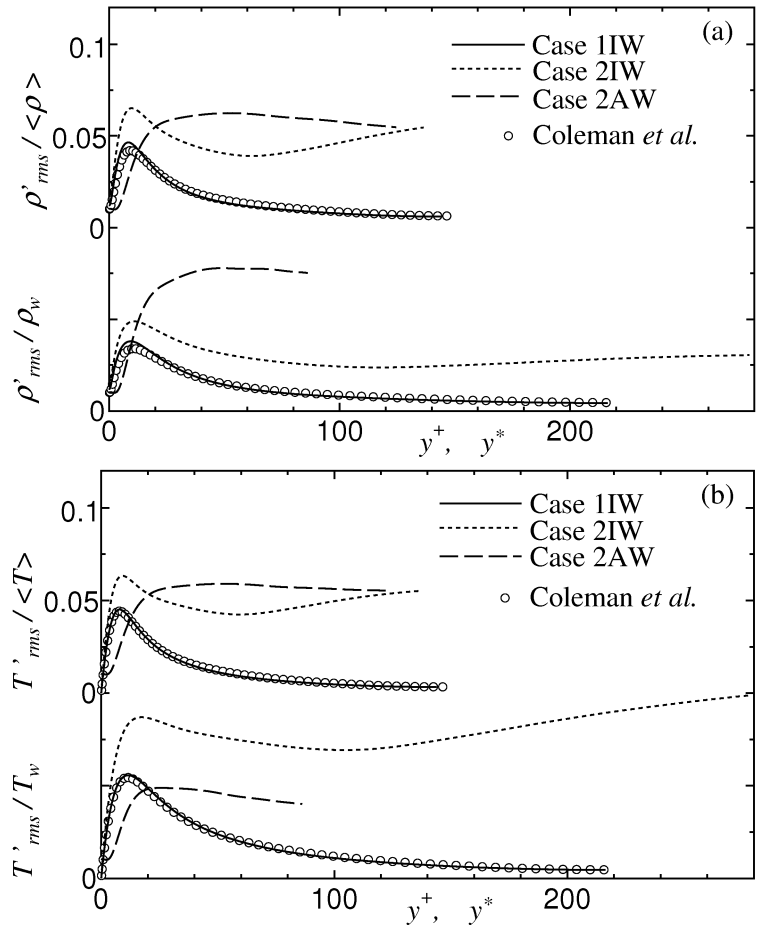

FIGURE 4.2. Profiles of (a) ρ'_{rms}/ρ_w and $\rho'_{rms}/\langle\rho\rangle$, (b) T'_{rms}/T_w and $T'_{rms}/\langle T\rangle$.

these variables have not been sufficiently investigated to date. The density and temperature fluctuation profiles scaled by the wall and local variables are compared with each other. The profiles of the RMS density flluctuations ρ'_{rms}/ρ_w and $\rho'_{rms}/\langle\rho\rangle$ are shown in figure 4.2(a), and the profiles of the RMS temperature fluctuations T'_{rms}/T_w and $T'_{rms}/\langle T\rangle$ are shown in figure 4.2(b). The peak value of ρ'_{rms}/ρ_w for Case 2AW is almost twice that of Case 2IW, while the peak value of T'_{rms}/T_w for Case 2IW is almost twice that of Case 2AW. This corresponds to the isobaric change. On the other hand, the RMS temperature fluctuation $T'_{rms}/\langle T\rangle$ is almost the same as the RMS density fluctuation $\rho'_{rms}/\langle\rho\rangle$, except that the RMS temperature fluctuation on the isothermal wall is zero.

Next, we investigate the universal scaling method with respect to the Reynolds

shear stress. The Favre average of a quantity ϕ is given by $\{\phi\} = \langle\rho\phi\rangle / \langle\rho\rangle$ and $''$ represents the turbulent fluctuation with respect to the Favre average. The relationships between averaging operations $\langle\ \ \rangle$ and $\{\ \ \}$ are as follows.

$$\langle\phi''\rangle = \langle\phi\rangle - \{\phi\} \tag{4.1}$$

$$\{\phi''\psi''\} = \langle\phi'\psi'\rangle - \langle\phi''\rangle\langle\psi''\rangle + \langle\rho'\phi'\psi'\rangle / \langle\rho\rangle \tag{4.2}$$

The non-dimensional Reynolds shear stresses are as follows;

$$-\langle\rho u_1' u_2'\rangle^+ = -\langle\rho u_1' u_2'\rangle/(\rho_w u_\tau^2), \tag{4.3}$$

$$-\langle\rho\rangle\langle u_1' u_2'\rangle^+/\rho_w = -\langle\rho\rangle\langle u_1' u_2'\rangle/(\rho_w u_\tau^2), \tag{4.4}$$

$$-\langle u_1' u_2'\rangle^* = -\langle\rho\rangle\langle u_1' u_2'\rangle/(\langle\rho\rangle u_{\tau*}^2), \tag{4.5}$$

$$-\langle\rho u_1' u_2'\rangle^* = -\langle\rho u_1' u_2'\rangle/(\langle\rho\rangle u_{\tau*}^2), \tag{4.6}$$

$$-\{u_1'' u_2''\}^* = -\langle\rho\rangle\{u_1'' u_2''\}/(\langle\rho\rangle u_{\tau*}^2), \tag{4.7}$$

$$-\langle\rho\rangle\{u_1'' u_2''\}^+/\rho_w = -\langle\rho\rangle\{u_1'' u_2''\}/(\rho_w u_\tau^2). \tag{4.8}$$

Equations (4.3)–(4.8) collapse the same form, provided that the density is constant. The profiles of (4.3)–(4.8) are shown in figure 4.3. The Reynolds shear stresses normalized by the wall variables $-\langle\rho u_1' u_2'\rangle^+$, $-\langle\rho\rangle\langle u_1' u_2'\rangle^+/\rho_w$ and $-\langle\rho\rangle\{u_1'' u_2''\}^+/\rho_w$, have almost the same value, and the Reynolds shear stresses scaled by the local and semi-local variables $-\langle u_1' u_2'\rangle^*$, $-\langle\rho u_1' u_2'\rangle^*$ and $-\{u_1'' u_2''\}^*$ coincide with each other. It indicates that the difference in the Reynolds shear stress between Favre and Reynolds averages is negligible. This is because the second and third terms on the right-hand side of (4.2) are negligible compared with the first term in the present data. The Reynolds shear stresses scaled by the wall variables for Cases 1IW and 2IW are smaller than that of Case A for $y^+ \leq 40$ and are almost the same as that of Case A for $y^+ \geq 40$. The Reynolds shear stress scaled by the wall variables for Case 2AW is almost the same as that of Case A for $y^+ \leq 20$ and are smaller than that of Case A for $y^+ \geq 20$. On the other hand, $-\langle u_1' u_2'\rangle^*$, $-\langle\rho u_1' u_2'\rangle^*$ and $-\{u_1'' u_2''\}^*$ have almost the same value of Case A near adiabatic and isothermal walls. Coleman *et al.* (1995), Guarini *et al.* (2000) and So *et al.* (1998) used $-\langle\rho u_1' u_2'\rangle^+$, $-\langle\rho\rangle\langle u_1' u_2'\rangle^+/\rho_w$ and $-\langle\rho\rangle\{u_1'' u_2''\}^+/\rho_w$

for the scaling of the Reynolds shear stress, respectively. In the present results, these scaling methods collapse the Reynolds shear stresses onto data of the incompressible turbulent flow (Case A) in the region of $y^+ \geq 40$ on the isothermal wall side and in the region of $y^+ \leq 20$ on the adiabatic wall side.

Figure 4.4 shows the profiles of the turbulent heat flux, $-\langle \rho u_2' T' \rangle / (\rho_w u_\tau T_w)$ and $-\langle \rho u_2' T' \rangle / (\langle \rho \rangle u_{\tau *} \langle T \rangle)$. The sign of the turbulent heat flux of the compressible turbulent flow near the isothermal wall (Cases 1IW and 2IW) is opposite to that of flow near the adiabatic wall (Case 2AW). Unlike the Reynolds shear stress, the turbulent heat flux does not have a universal profile in the present result, because the turbulent heat flux is directly and strongly influenced by the thermal boundary condition.

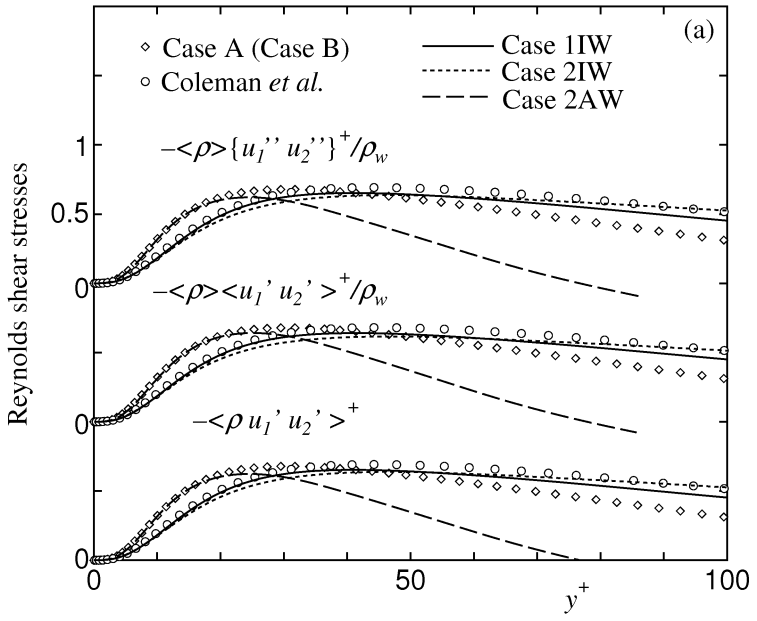

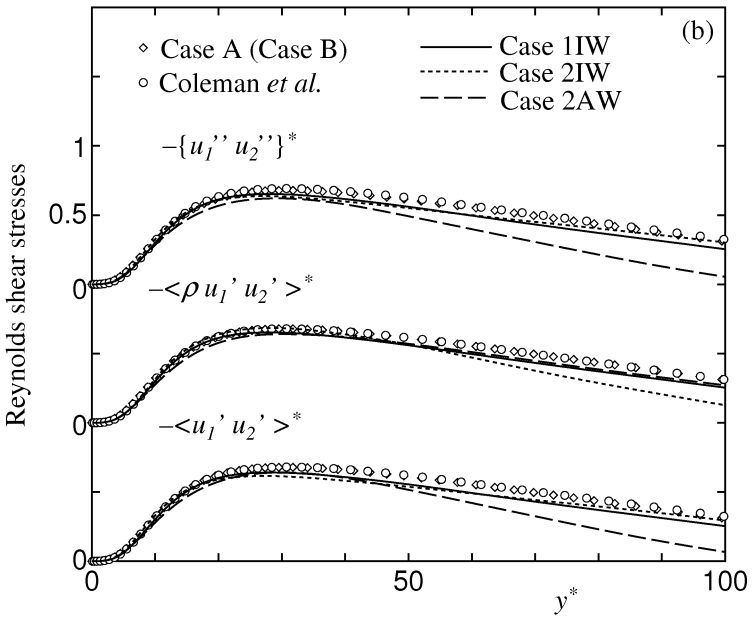

FIGURE 4.3. Profiles of Reynolds shear stresses.

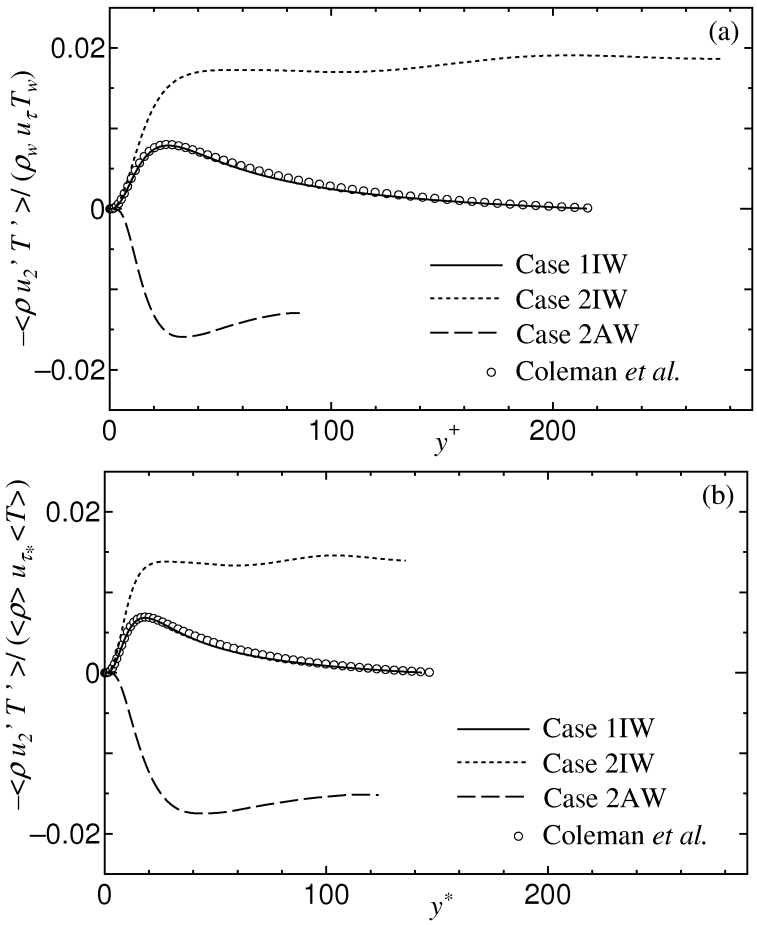

FIGURE 4.4. Profiles of turbulent heat fluxes.

4.3 Near-wall Asymptotic Behaviors

4.3.1 Analytical Estimates for Near-wall Asymptotic Behaviors

The turbulent fluctuations ϕ' and ϕ'' with respect to Reynolds and Favre averages of ϕ are expanded in terms of y as follows;

$$\phi' = \phi'(0) + y \left.\frac{\partial \phi'}{\partial y}\right|_{y=0} + \frac{y^2}{2} \left.\frac{\partial^2 \phi'}{\partial y^2}\right|_{y=0} + O(y^3), \tag{4.9}$$

$$\phi'' = \phi''(0) + y \left.\frac{\partial \phi''}{\partial y}\right|_{y=0} + \frac{y^2}{2} \left.\frac{\partial^2 \phi''}{\partial y^2}\right|_{y=0} + O(y^3). \tag{4.10}$$

The near-wall asymptotic behaviors with respect to Reynolds and Favre averages are theoretically gained from (4.9) and (4.10) with boundary conditions. Since the density at the wall is governed by the continuity equation, the mean density approaches a constant non-zero value with the decrease of y^+ for Cases 1IW, 2IW and 2AW (see figure 4.5). The continuity equation and the non-slip wall boundary condition provide the following relation at the wall.

$$\left.\frac{\partial u_i}{\partial x_i}\right|_w = \frac{1}{\rho_w} \left.\frac{\partial \rho}{\partial t}\right|_w \tag{4.11}$$

The density varies in time and space in the present compressible simulations, this yields $\partial u_j/\partial x_j|_w \neq 0$. As a result, $\partial u_2'/\partial x_2|_w$ and $\partial u_2''/\partial x_2|_w$ do not become zero for Cases 1 and 2. On the other hand, the continuity equation provides $\partial u_2'/\partial x_2|_w = 0$ in incompressible turbulent flow. Regarding the wall boundary conditions, the near-wall asymptotic behaviors of $(u_\alpha')_{rms}$ $(\alpha = 1, 2, 3)$, $\langle k \rangle$ $(= \langle u_i' u_i' \rangle /2)$, ε_k (see (5.13)), ρ'_{rms}, p'_{rms}, T'_{rms}, $-\langle u_1' u_2' \rangle$ and $-\langle u_2' T' \rangle$ are summarized in table 4.1. Note that the near-wall asymptotic behaviors of $(u_2')_{rms}$, $-\langle u_1' u_2' \rangle$ and $-\langle u_2' T' \rangle$ for compressible turbulent flow are different from the corresponding incompressible ones.

4.3.2 Near-wall Asymptotic Behaviors of Turbulence Statistics

The difference in scaling is investigated using the wall-normal RMS velocities $(u_2')^+_{rms}$ and $[\langle \rho \rangle \{u_2''^2\}/(\rho_w u_\tau^2)]^{1/2}$ (see figure 4.6). The wall-normal inten-

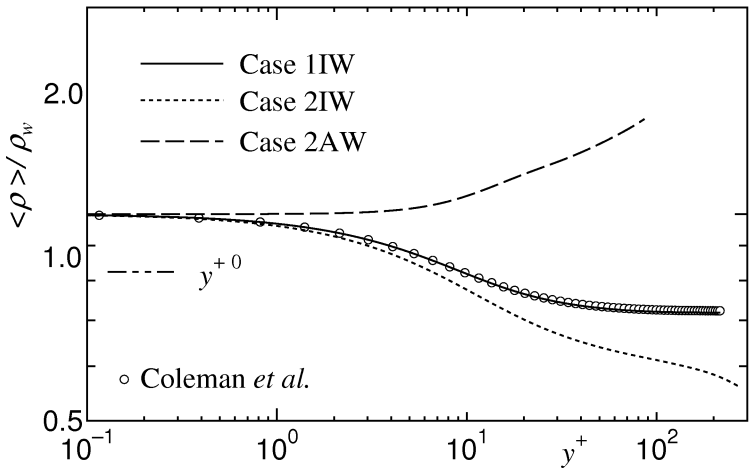

FIGURE 4.5. Near-wall behavior of $\langle\rho\rangle/\rho_w$.

TABLE 4.1. Power index n ($\phi \propto y^n$) of near-wall asymptotic behavior.

Case	$(u_1')_{rms}$	$(u_2')_{rms}$	$(u_3')_{rms}$	$\langle k\rangle$	ε_k	ρ'_{rms}	T'_{rms}	p'_{rms}	$-\langle u_1'u_2'\rangle$	$-\langle u_2'T'\rangle$
1IW, 2IW	1	1	1	2	0	0	1	0	2	2
2AW	1	1	1	2	0	0	0	0	2	1
AIW, BIW	1	2	1	2	0	-	1	0	3	3
BAW	1	2	1	2	0	-	0	0	3	2

sities of turbulence, $(u_2')^+_{rms}$, for Cases 1IW, 2IW and 2AW vary linearly with the decrease of y^+, while that of Case A vary linearly with the decrease of y^{+2} as shown in table 4.1. The asymptotic behavior of $[\langle\rho\rangle\{u_2''^2\}/(\rho_w u_\tau^2)]^{1/2}$ is the same as that of $(u_2')^+_{rms}$. This is because the boundary conditions of Favre and Reynolds averages are not different, and the condition of density, $\langle\rho\rangle/\rho_w \propto O(y^{+0})$, is satisfied (see figure 4.5). Figure 4.6 shows that the range of $O(y^{+0})$ near the adiabatic wall is narrower than that near the isothermal wall. So *et al.* (1998), using the Morkovin's hypothesis, found that the asymptotic behavior of $[\langle\rho\rangle\{u_2''^2\}/(\rho_w u_\tau^2)]^{1/2}$ became equal to that of the incompressible turbulent flow. However, they did not compare the asymptotic behaviors for compressible and incompressible turbulent flows in logarithmic coordinates. The present result indicates that the asymptotic behavior of $\left[\langle\rho\rangle\{u_2''^2\}/(\rho_w u_\tau^2)\right]^{1/2}$ is the same as that of $(u_2')^+_{rms}$ for the turbulent channel flows at $M = 1.5$. The asymptotic

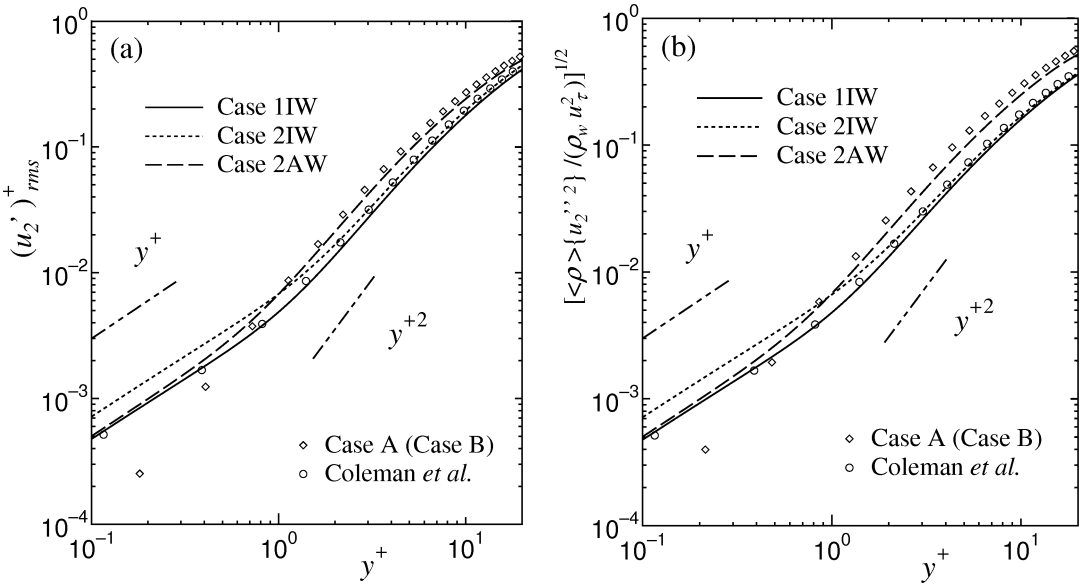

FIGURE 4.6. Near-wall behavior (a) $(u_2')^+_{rms}$ and (b) $[\langle\rho\rangle\{u_2''^2\}/(\rho_w u_\tau^2)]^{1/2}$.

behavior of the wall-normal RMS velocity fluctuation for the compressible turbulent flow is not equal to that for the incompressible turbulent flow, even if the mean density variation is taken into account for the scaling. Thus, Morkovin's hypothesis is not applicable to near-wall asymptotic behavior.

RMS density and temperature fluctuations scaled by the wall variables are shown in figure 4.7. The RMS density fluctuation approaches a constant non-zero value with the decrease of y^+ near both adiabatic and isothermal walls in compressible turbulent flow. On the other hand, the RMS temperature fluctuation varies linearly with the decrease of y^+ near the isothermal wall and approaches a constant non-zero value with the decrease of y^+ near the adiabatic wall in compressible turbulent flow.

The Reynolds shear stress $-\langle\rho u_1' u_2'\rangle^+$ and turbulent heat flux, $-\langle\rho u_2' T'\rangle^+$ $=-\langle\rho u_2' T'\rangle/(\rho_w u_\tau T_\tau)$ are shown in figure 4.8. The near-wall asymptotic behaviours of compressible turbulent flow presented in table 4.1 are obviously not observed for both $-\langle\rho u_1' u_2'\rangle^+$ and $-\langle\rho u_2' T'\rangle^+$ in the present simulations, because the dilatational effect is small at the wall. We confirmed the same trend

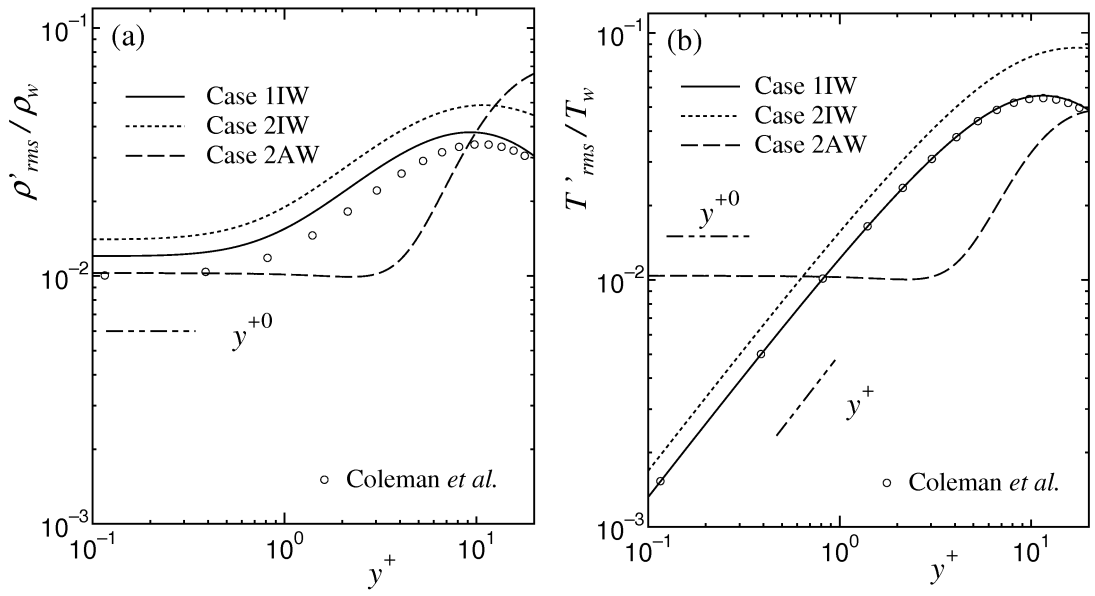

FIGURE 4.7. Near-wall behavior (a) ρ'_{rms}/ρ_w and (b) T'_{rms}/T_w.

for turbulent heat flux near the adiabatic wall. The relation between near-wall asymptotic behaviour and the Mach number will be considered in the near future. We also confirmed that near-wall asymptotic behaviours of the other statistics corresponded to the theoretical behaviours in table 4.1.

4.4 Reynolds Analogies

Morkovin (1962) proposed the five SRA relations for the adiabatic wall. One of them is as follows:

$$\frac{T'/\langle T\rangle}{(\gamma-1)\langle M\rangle^2 u_1'/\langle u_1\rangle} \approx 1 \tag{4.12}$$

The Reynolds average is used in (4.12) for simplicity. We confirmed that the difference between Favre and Reynolds averages was negligible. Gaviglio (1987), Rubesin (1990) and Huang *et al.* (1995) presented modified Reynolds analogies (GSRA, RSRA and HSRA) which could apply to the isothermal wall. They are given for the adiabatic and isothermal walls as follows:

$$\frac{T'/\langle T\rangle}{(\gamma-1)\langle M\rangle^2 u_1'/\langle u_1\rangle} \approx \frac{1}{h\,(1-g\,\partial\langle T_t\rangle/\partial\langle T\rangle)} \quad , \tag{4.13}$$

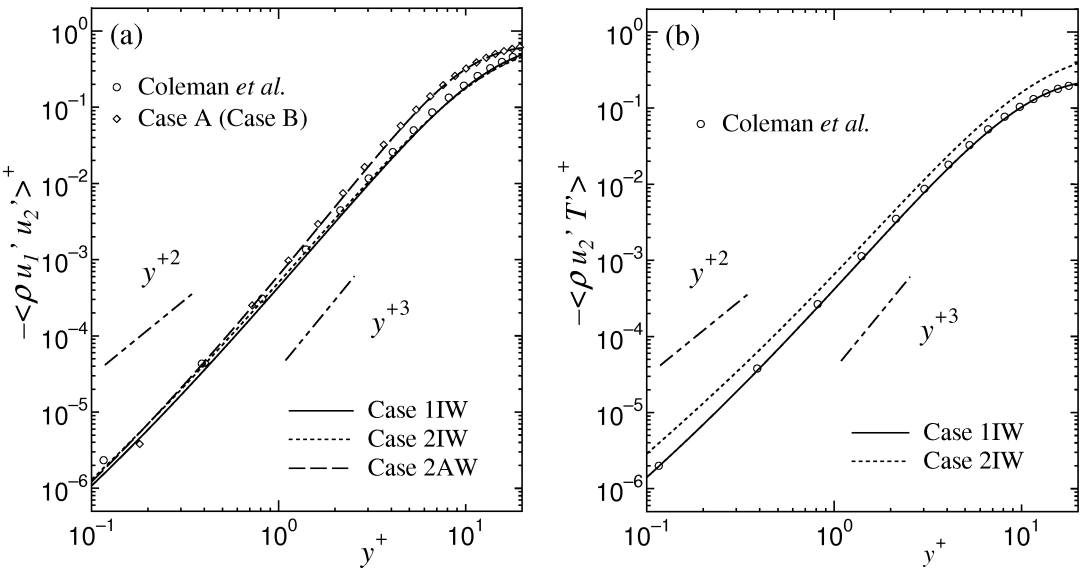

FIGURE 4.8. Near-wall behavior (a) $-\langle \rho u_1' u_2' \rangle^+$ and (b) $-\langle \rho u_2' T' \rangle^+$.

$$\frac{T'/\langle T \rangle}{(\gamma-1)\langle M \rangle^2 u_1'/\langle u_1 \rangle} \approx \frac{1}{h\,(g\,\partial\langle T_t \rangle/\partial\langle T \rangle - 1)} \quad , \tag{4.14}$$

where $\langle M \rangle = \langle u_1 \rangle / \left((\gamma-1)c_p \langle T \rangle\right)^{1/2}$ is a local Mach number and $T_t = T + u_i^2/(2c_p)$ is a total temperature. The factors (g, h) of GSRA, RSRA and HSRA are $(1, 1)$, $(1, 1.34)$ and $(1, Pr_t)$, respectively. If (g, h) are $(0, 1)$, the form of (4.13) becomes equal to that of (4.12). GSRA and HSRA are based on the mixing length theory with respect to the streamwise velocity and temperature fluctuations. The turbulent Prandtl number in HSRA is defined as

$$Pr_t = \frac{\{u_2'' u_1''\}\ \partial\{T\}/\partial y}{\{u_2'' T''\}\ \partial\{u_1\}/\partial y} \quad . \tag{4.15}$$

To examine the applicability and usefulness of the SRA, GSRA, RSRA and HSRA, we introduce a criterion:

$$G \equiv \frac{\langle T'^2 \rangle^{1/2}/\langle T \rangle}{(\gamma-1)\langle M \rangle^2 \langle u_1'^2 \rangle^{1/2}/\langle u_1 \rangle} \left(h \left| g \frac{\partial \langle T_t \rangle}{\partial \langle T \rangle} - 1 \right| \right). \tag{4.16}$$

Note that the root mean squares $\langle u_1'^2 \rangle^{1/2}$ and $\langle T'^2 \rangle^{1/2}$ are used instead of u_1' and T'. The model yields the exact value for $G = 1$.

The profiles of G for Cases 1IW, 2IW and 2AW are shown in figure 4.9, where SRA near the isothermal wall is also considered for comparison. The values of G of SRA are greatly different from unity for Cases 1IW and 2IW. Although the SRA is satisfied near the adiabatic wall in Guarini *et al.* (2000), the SRA is not successful for Case 2AW. The reason is explained as below. The SRA is available under the assumption that the total temperature fluctuation is negligible compared to the static temperature fluctuations. When the above assumption is not satisfied, the following condition presented by Guarini *et al.* (2000) must be satisfied.

$$\frac{\langle T'^2 \rangle}{\langle T \rangle^2} \ll \frac{\langle T_t'^2 \rangle - 2 \langle T' T_t' \rangle}{\langle T \rangle^2} \tag{4.17}$$

However, both assumption and condition are not satisfied for Case 2AW (see figure 4.10), so that the SRA is not successful near the adiabatic wall.

The region of $G \simeq 1$ of HSRA is larger than that of GSRA for Case 1IW, because the turbulent Prandtl number is treated as a variable in HSRA and unity in GSRA. The values of G of HSRA and GSRA for Cases 2IW and 2AW are almost unity in the region of $y/H < 0.6$ and decrease gradually in the region of $y/H > 0.6$ where the influence of the opposite wall is not negligible. The RSRA does not agree well with the DNS data for all cases. It is found that the existing modified Reynolds analogies do not agree well with the DNS data on the compressible turbulent flow between adiabatic and isothermal walls.

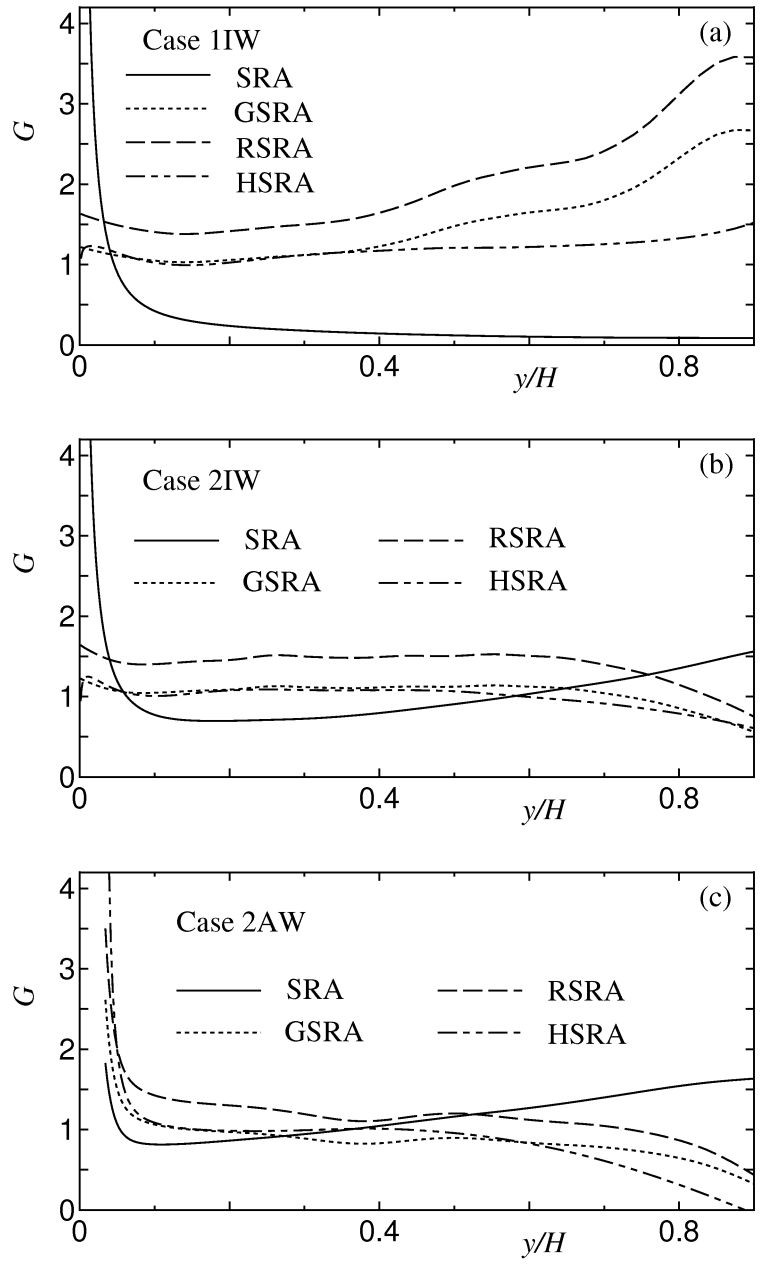

FIGURE 4.9. Strong Reynolds analogy and modified Reynolds anologies: (a) Case 1IW, (b) Case 2IW and (c) Case 2AW.

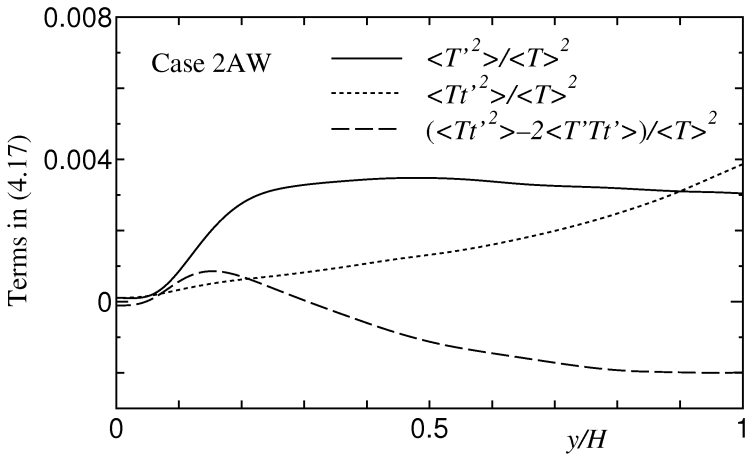

FIGURE 4.10. Comparison between RMS total and static temperature fluctuations with Reynolds average for Case 2AW.

4.5 Summary

We can summarize as follows:

(1) When the velocity fluctuations are scaled by the wall variables, these profiles are larger and smaller near isothermal and adiabatic walls, respectively, compared with those of the incompressible turbulent channel flow. On the other hand, these profiles agree well with the data on incompressible turbulent channel flow, when such profiles are scaled by local mean variables. This means that Morkovin's hypothesis is applicable to velocity fluctuation profiles.

(2) The RMS temperature fluctuation profile scaled by the mean temperature is almost the same as that of the RMS density fluctuation profile scaled by the mean density, except that the RMS temperature fluctuation on the isothermal wall is zero. The wall variable scaling does not result in such a similarity between temperature and density fluctuations.

(3) The difference between Favre and Reynolds averages on the Reynolds shear stresses is negligible. The semi-local scaling provides the universal profile of the Reynolds shear stress. On the other hand, the turbulent heat flux does not have universal scaling in this study.

(4) The near-wall asymptotic behavior of the wall-normal RMS velocity fluctuation of the compressible turbulent flow is not equal to that of the incompressible turbulent flow, even if the mean density variation is taken into account for the scaling. Thus, Morkovin's hypothesis is not applicable to near-wall asymptotic behavior.

(5) The RMS density fluctuation approaches a constant non-zero value with the decrease of the wall unit, y^+, near both adiabatic and isothermal walls in compressible turbulent flow. The RMS temperature fluctuation profile scaled by the wall temperature varies linearly with the decrease of y^+ near the isothermal wall and approaches a constant non-zero value with the decrease of y^+ near the adiabatic wall in compressible turbulent flow.

(6) The existing modified Reynolds analogies do not agree well with the data on compressible turbulent flow between adiabatic and isothermal walls.

Chapter 5.

Energy Transfers

5.1 Outline

In this chapter, the mechanism of the energy transfer among the turbulent kinetic, mean kinetic and internal energies is investigated for compressible turbulent flows near isothermal and adiabatic walls. First, the conservation equations of compressible turbulent flow are explained. Next, the turbulent kinetic, mean kinetic and internal energies are investigated to understand the energy transfers of compressible turbulent flow. In particular, the compressibility and dissipation terms are investigated in detail.

5.2 Conservation Equations

The Favre-averaged mean-flow kinetic energy $\{K\}$, the Favre-averaged turbulent kinetic energy $\{k\}$, the Favre-fluctuation mean-flow kinetic energy K'' and the Favre-fluctuation turbulent kinetic energy k'' are defined as $\{K\} \equiv \{u_i\}^2/2$, $\{k\} \equiv \{u_i'' u_i''\}/2$, $K'' \equiv \{u_i\} u_i''$ and $k'' \equiv u_i'' u_i''/2 - \{k\}$, respectively. The continuity, momentum and total energy equations are as follows in fully developed turbulent channel flow (see Huang *et al.* 1995);

$$\frac{\partial \langle\rho\rangle \{u_2\}}{\partial x_2} = 0, \tag{5.1}$$

$$\frac{\partial \langle\rho\rangle \{u_i\}\{u_2\}}{\partial x_2} = \frac{\partial \langle\tau_{i2}\rangle}{\partial x_2} - \frac{\partial \langle\rho\rangle \{u_i'' u_2''\}}{\partial x_2} + \langle\rho\rangle f_i, \tag{5.2}$$

$$\frac{\partial \langle\rho\rangle \{u_2\} [\{K\} + \{k\} + c_v\{T\} + \langle p\rangle / \langle\rho\rangle]}{\partial x_2} = \frac{\partial [\langle\tau_{i2}\rangle \langle u_i\rangle + \langle\tau_{i2}' u_i'\rangle - \langle q_2\rangle]}{\partial x_2}$$

$$-\frac{\partial\left[\langle\rho\rangle\left\{u_2''K''\right\}+\langle\rho\rangle\left\{u_2''k''\right\}+\langle\rho\rangle c_p\{u_2''T''\}\right]}{\partial x_2}+\langle\rho\rangle f_1\{u_1\}, \quad (5.3)$$

where $\{u_2''K''\}$ and $\{u_2''k''\}$ are

$$\{u_2''K''\}=\{u_2''u_i''\}\{u_i\}, \quad (5.4)$$

$$\{u_2''k''\}=\{u_2u_iu_i\}/2-\{u_2\}\{u_i\}\{u_i\}/2-\{u_2''u_i''\}\{u_i\}-\{u_i''u_i''\}\{u_2\}/2. \quad (5.5)$$

The averaged state equation is

$$\langle p\rangle=\frac{(\gamma-1)c_p\langle\rho\rangle\{T\}}{\gamma}. \quad (5.6)$$

The Reynolds averaged viscous tensor $\langle\tau_{ij}\rangle$ is defined as

$$\begin{aligned}\langle\tau_{ij}\rangle=&\langle\mu\rangle\left(\frac{\partial\langle u_i\rangle}{\partial x_j}+\frac{\partial\langle u_j\rangle}{\partial x_i}\right)-\frac{2}{3}\langle\mu\rangle\langle d\rangle\delta_{ij}\\&+\left\langle\mu'\left(\frac{\partial u_i'}{\partial x_j}+\frac{\partial u_j'}{\partial x_i}\right)\right\rangle-\frac{2}{3}\langle\mu'd'\rangle\delta_{ij}, \quad (5.7)\end{aligned}$$

where $\langle d\rangle=\partial\langle u_j\rangle/\partial x_j$ and $d'=\partial u_j'/\partial x_j$. The fluctuation viscous tensor, $\tau_{ij}'=\tau_{ij}-\langle\tau_{ij}\rangle$, is defined as

$$\begin{aligned}\tau_{ij}'=&\langle\mu\rangle\left(\frac{\partial u_i'}{\partial x_j}+\frac{\partial u_j'}{\partial x_i}\right)-\left\langle\mu'\left(\frac{\partial u_i'}{\partial x_j}+\frac{\partial u_j'}{\partial x_i}\right)\right\rangle-\frac{2}{3}\langle\mu\rangle d'\delta_{ij}+\frac{2}{3}\langle\mu'd'\rangle\delta_{ij}\\&+\mu'\left(\frac{\partial u_i'}{\partial x_j}+\frac{\partial u_j'}{\partial x_i}\right)-\frac{2}{3}\mu'd'\delta_{ij}+\mu'\left(\frac{\partial\langle u_i\rangle}{\partial x_j}+\frac{\partial\langle u_j\rangle}{\partial x_i}\right)-\frac{2}{3}\mu'\langle d\rangle\delta_{ij}. \quad (5.8)\end{aligned}$$

The Reynolds averaged heat flux $\langle q_2\rangle$ is given by

$$\langle q_2\rangle=-\langle\kappa\rangle\frac{\partial\langle T\rangle}{\partial x_2}-\left\langle\kappa'\frac{\partial T'}{\partial x_2}\right\rangle. \quad (5.9)$$

The total energy is defined as the sum of the turbulent kinetic energy $\{k\}$, the mean kinetic energy $\{K\}$ and the internal energy, $\{e\}=c_v\{T\}$, and it should be conserved in the compressible turbulent channel flow. We confirmed that the conservation of the total energy was satisfied in the present simulations of Cases 1 and 2. On the other hand, there are energy transfers among the turbulent kinetic, mean kinetic and internal energies. In the subsequent sections, we shall clarify the mechanism of the energy transfer through these energy budgets.

5.3 Energy Budgets

The turbulent kinetic energy equation is

$$P_k + D_k - \varepsilon_k + C_k = 0, \tag{5.10}$$

where the production P_k, diffusion D_k, dissipation per unit volume ε_k and intrinsic compressibility term C_k are defined as follows:

$$\begin{aligned} P_k &= -\langle\rho\rangle \{u_1'' u_2''\} \frac{\partial\{u_1\}}{\partial x_2}, & (5.11)\\ D_k &= \frac{\partial\left[\langle\tau_{i2}' u_i'\rangle - \langle\rho\rangle \{u_2'' k''\} - \langle p' u_2'\rangle\right]}{\partial x_2}, & (5.12)\\ \varepsilon_k &= \left\langle \tau_{ij}' \frac{\partial u_i'}{\partial x_j} \right\rangle, & (5.13)\\ C_k &= -C_{k1} + C_{k2} + C_{k3}, & (5.14) \end{aligned}$$

where $C_{k1} = \langle u_2''\rangle \partial\langle p\rangle / \partial x_2$, $C_{k2} = \langle u_i''\rangle \partial\langle\tau_{i2}\rangle / \partial x_2$ and $C_{k3} = \langle p' \partial u_k' / \partial x_k\rangle$. The mean kinetic energy equation is

$$D_K - \varepsilon_{TK} - \varepsilon_{VK} + C_K + F_K = 0, \tag{5.15}$$

where the diffusion D_K, turbulent dissipation per unit volume ε_{TK}, viscous dissipation per unit volume ε_{VK}, intrinsic compressibility term C_K and force term F_K are as follows:

$$\begin{aligned} D_K &= \frac{\partial\left[\langle\tau_{i2}\rangle\langle u_i\rangle - \langle\rho\rangle \{u_2'' K''\} - \langle p\rangle\langle u_2\rangle\right]}{\partial x_2}, & (5.16)\\ \varepsilon_{TK} &= -\langle\rho\rangle \{u_1'' u_2''\} \frac{\partial\{u_1\}}{\partial x_2}, & (5.17)\\ \varepsilon_{VK} &= \langle\tau_{i2}\rangle \frac{\partial\langle u_i\rangle}{\partial x_2}, & (5.18)\\ C_K &= C_{k1} - C_{k2} + C_{K1}, & (5.19)\\ F_K &= \langle\rho\rangle f_1\{u_1\}. & (5.20) \end{aligned}$$

After turbulent kinetic and mean kinetic energy equations are subtracted from the total energy equation (5.3), the internal energy equation is obtained as

$$D_e + \varepsilon_{VK} + \varepsilon_k - C_{K1} - C_{k3} = 0, \tag{5.21}$$

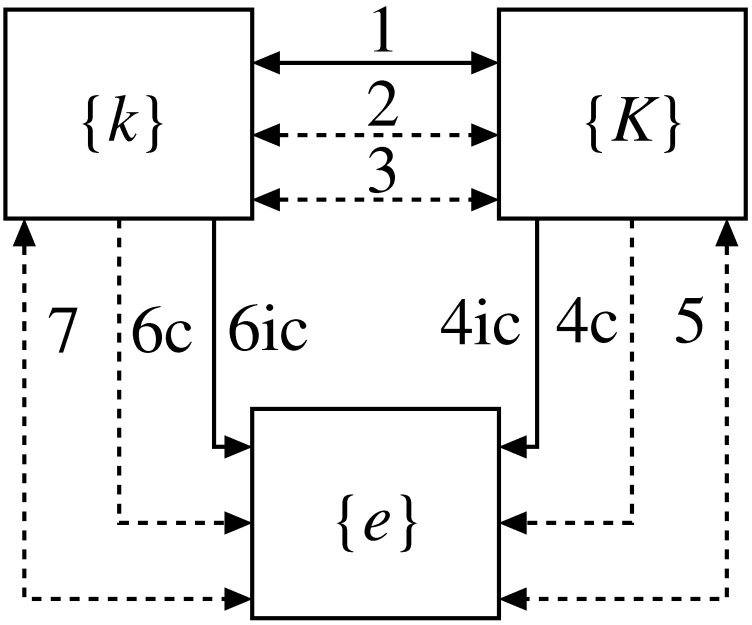

FIGURE 5.1. Energy transfer of wall-bounded compressible turbulent flow: 1. $P_k(=\varepsilon_{TK})$, 2. C_{k1}, 3. C_{k2}, 4c. Compressible part of ε_{VK}, 4ic. Incompressible part of ε_{VK}, 5. C_{K1}, 6c. Compressible part of ε_k, 6ic. Incompressible part of ε_k, 7. C_{k3}. Terms 4c, 4ic, 6c and 6ic are irreversible. Dashed arrows indicate intrinsic compressibility terms.

where the diffusion D_e is defined as

$$D_e = D_{e1} + D_{e2}, \tag{5.22}$$

where

$$D_{e1} = -\frac{\partial \langle \rho \rangle c_v \{u_2'' T''\}}{\partial x_2}, \qquad D_{e2} = -\frac{\partial \langle q_2 \rangle}{\partial x_2}. \tag{5.23}$$

From (5.10), (5.15) and (5.21), the energy transfers among turbulent kinetic, mean kinetic and internal energies are represented by seven terms (see Huang *et al.* 1995). 1. $P_k(=\varepsilon_{TK})$, 2. C_{k1}, 3. C_{k2}, 4. ε_{VK}, 5. C_{K1}, 6. ε_k, 7. C_{k3}. Terms 2, 3, 5 and 7 represent the intrinsic compressibility terms. Terms 4 and 6 which represent the irreversible energy transfers can be distinguished into the compressible parts (4c, 4ic) and the incompressible parts (6c, 6ic), respectively. Terms 4 and 6 were not divided into compressible and incompressible parts in the study of

Huang *et al.* (1995). Energy transfers of wall-bounded compressible turbulent flow are summarized in figure 5.1. The dashed arrows represent the intrinsic compressibility terms.

Turbulent kinetic energy budgets of Cases 1, 2 and A (B) are shown in figure 5.2, in which the profiles are scaled by bulk variables, $\rho_m U_m^3/H$, for comparison of Cases 1 and 2. The scaling of Case A is the same as for Case 1. Here, Huang *et al.* (1995) used the mixture of wall and bulk variables, $\tau_w U_m/H$, and Guarini *et al.* (2000) used wall variables, $\rho_w u_\tau/\delta_v$, where $\delta_v = \mu_w/(\rho_w u_\tau)$ is viscous length scale, for scaling the turbulent kinetic energy budget, respectively. The peak value of the production term P_k (term 1 of figure 5.1) near the adiabatic wall is smaller and its location moves to the centre of the channel, comparing with those of P_k near the isothermal wall (see figure 5.2(b)). The intrinsic compressibility term in the turbulent kinetic energy equation, C_k, and the turbulent kinetic energy dissipation rate per unit volume, ε_k, are discussed in sections 5.4 and 5.5, respectively.

Next, we consider the budgets scaled by the mixture of local and semi-local variables, $\langle\rho\rangle\, u_{\tau*}^3/\delta_{v*}$, where $\delta_{v*} = \langle\mu\rangle/(\langle\rho\rangle\, u_{\tau*})$ is semi-local viscous length scale, for Cases 2IW and 2AW (see figure 5.3). Lechner *et al.* (2001) reported that the production and dissipation rate in the turbulent kinetic energy equation normalized by $\tau_w U_m/H$ were reduced compared to their incompressible counterparts. However, figure 5.3 shows that the production and dissipation terms of Cases 2IW and 2AW agree well with the data of the Case A. It indicates that the difference observed in the turbulent kinetic energy budget scaled by $\rho_m U_m/H$ or $\tau_w U_m/H$ is mainly due to the variable property effect.

The mean kinetic energy budgets of Case 1, 2 and A (B) are shown in figure 5.4, which shows that the mean kinetic energy budget of Case 1 is not essentially different from that of Case A. We also confirmed that the difference between budgets near adiabatic and isothermal walls for Case 2 was mainly due to the variable property effect. The intrinsic compressibility term in the mean kinetic energy equation, C_K, and the viscous dissipation per unit volume, ε_{VK},

are discussed in sections 5.4 and 5.5, respectively.

The internal energy budgets of Cases 1 and 2 are shown in figure 5.5, and the energy (passive scalar) budgets of Cases A and B are shown in figure 5.6. For Cases A and B, the bulk velocity U_m and the friction temperature T_τ at the isothermal wall are used for scaling the enrgy budgets. The dissipation rates ε_k and ε_{VK} are irreversible energy transfers from the turbulent kinetic and mean kinetic energies to the internal energy, respectively. On the other hand, the energy transfer due to the dissipation rate does not exist in incompressible turbulent flow with passive scalar transport, because the viscous friction work does not appear in the energy equation of incompressible turbulent flow (cf. (A.12) and (A.3)). For Cases A and B, the artificial heat sources are added in the energy (passive scalar) equations instead of the viscous friction work, where the heat source of Case A is twice that of Case B (see (A.13) and (A.14)). As a result, the profiles of internal energy budgets of Cases 1 and 2 are different from those of Cases A and B. The qualitative comparison of the internal energy budgets between compressible and incompressible turbulent flows has no meaning, because their normalizations are different. Note that the peaks of turbulent and molecular diffusions do not appear near the adiabatic wall of Case B.

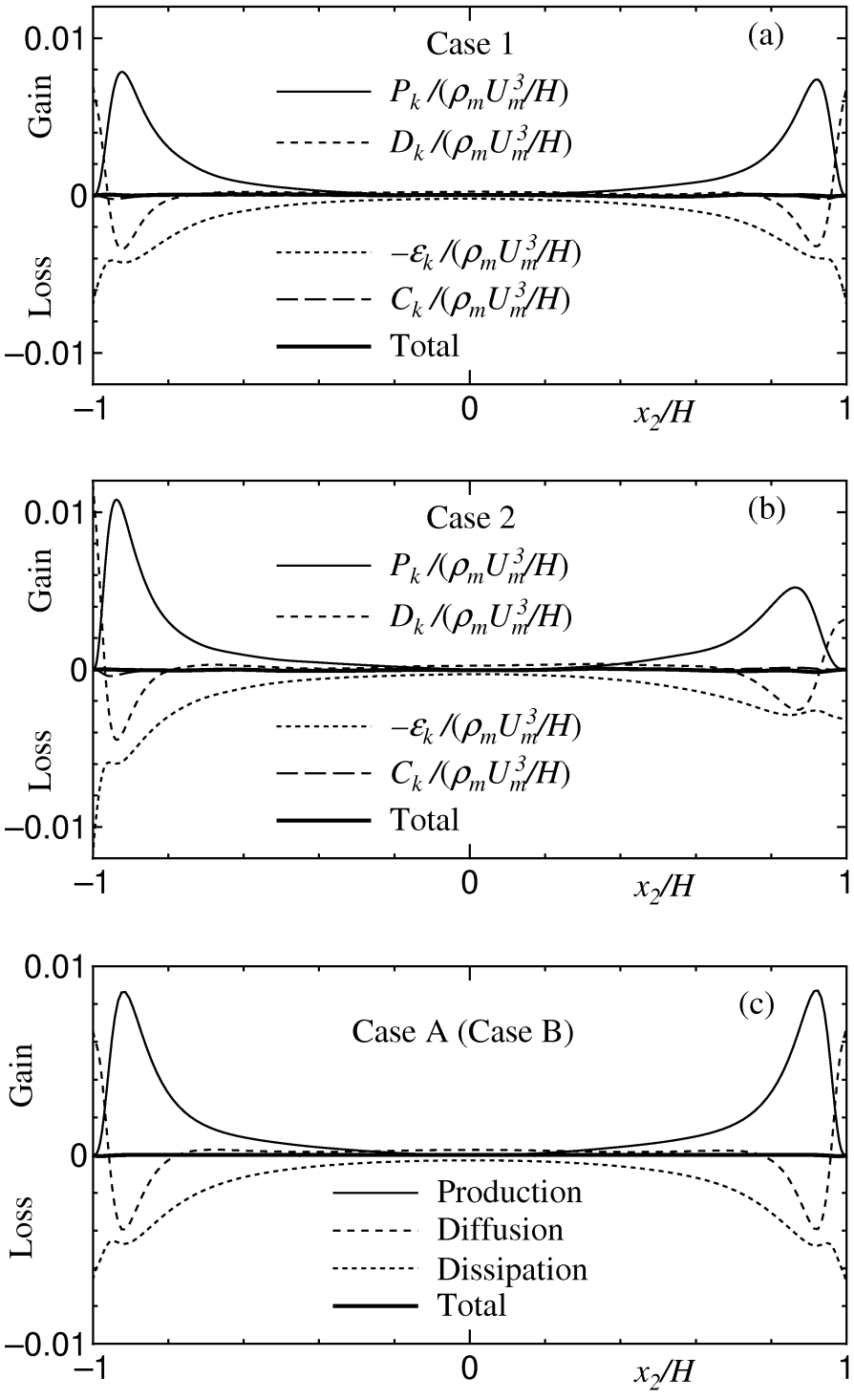

FIGURE 5.2. Turbulent kinetic energy budgets: (a) Case 1, (b) Case 2, (c) Case A (B).

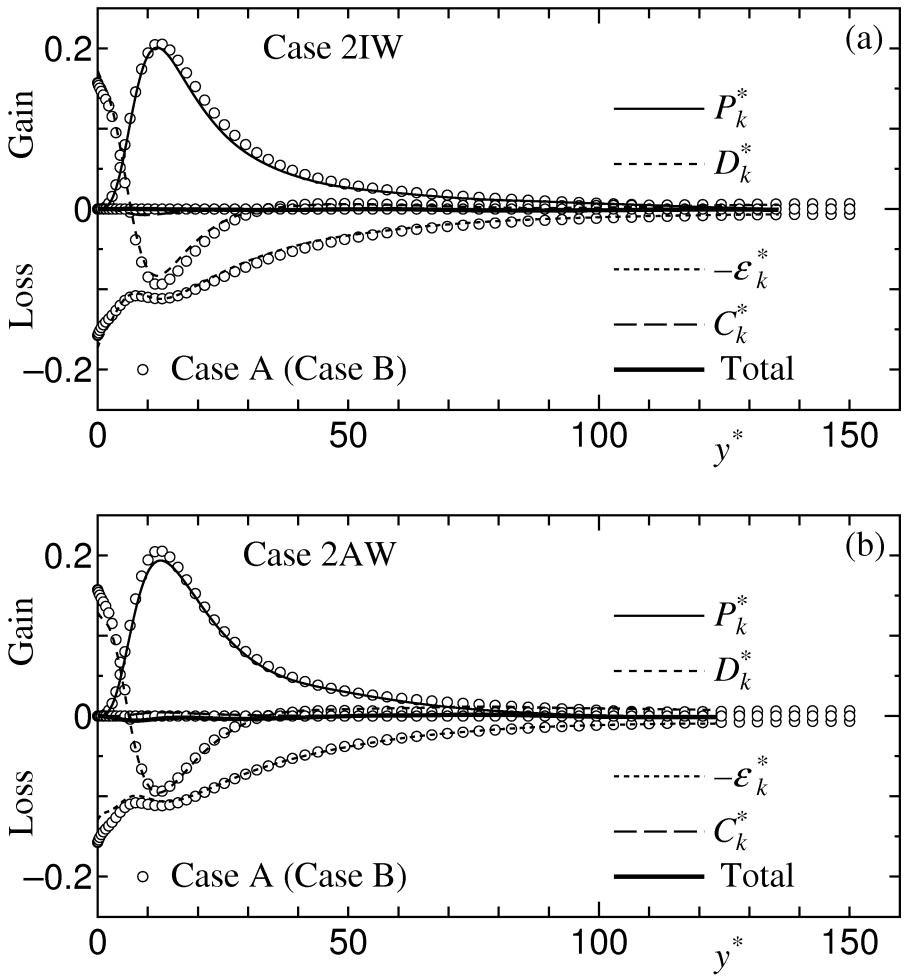

FIGURE 5.3. Turbulent kinetic energy budgets in semi-local wall units for Case 2: (a) near the isothermal wall, (b) near the adiabatic wall.

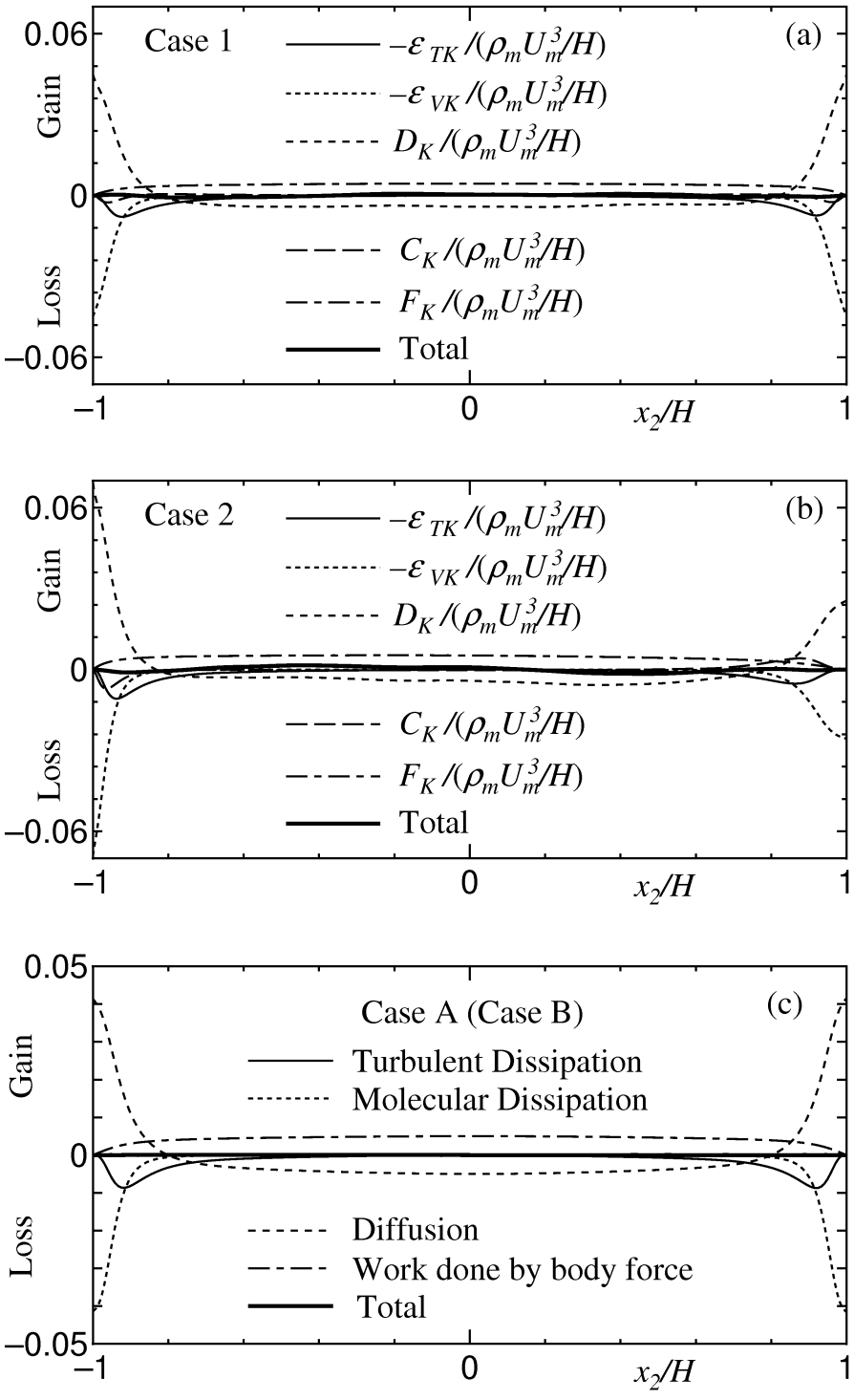

FIGURE 5.4. Mean kinetic energy budgets: (a) Case 1, (b) Case 2, (c) Case A (B).

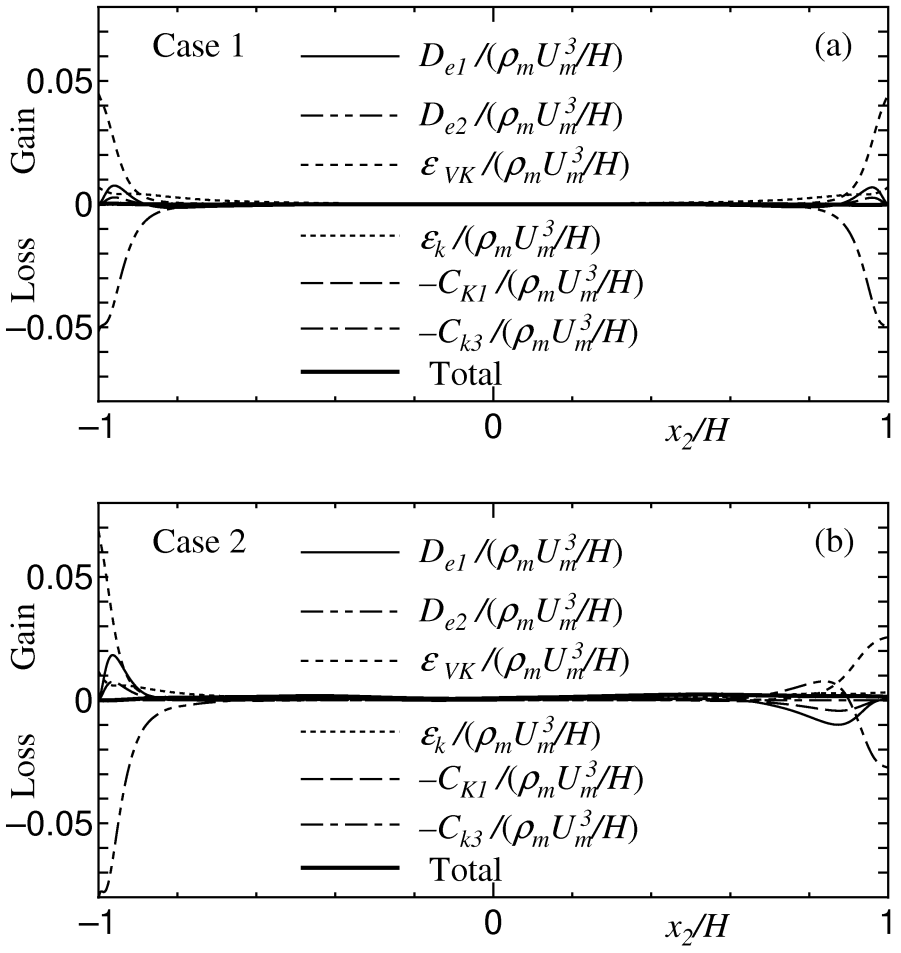

FIGURE 5.5. Internal energy budgets: (a) Case 1 and (b) Case 2.

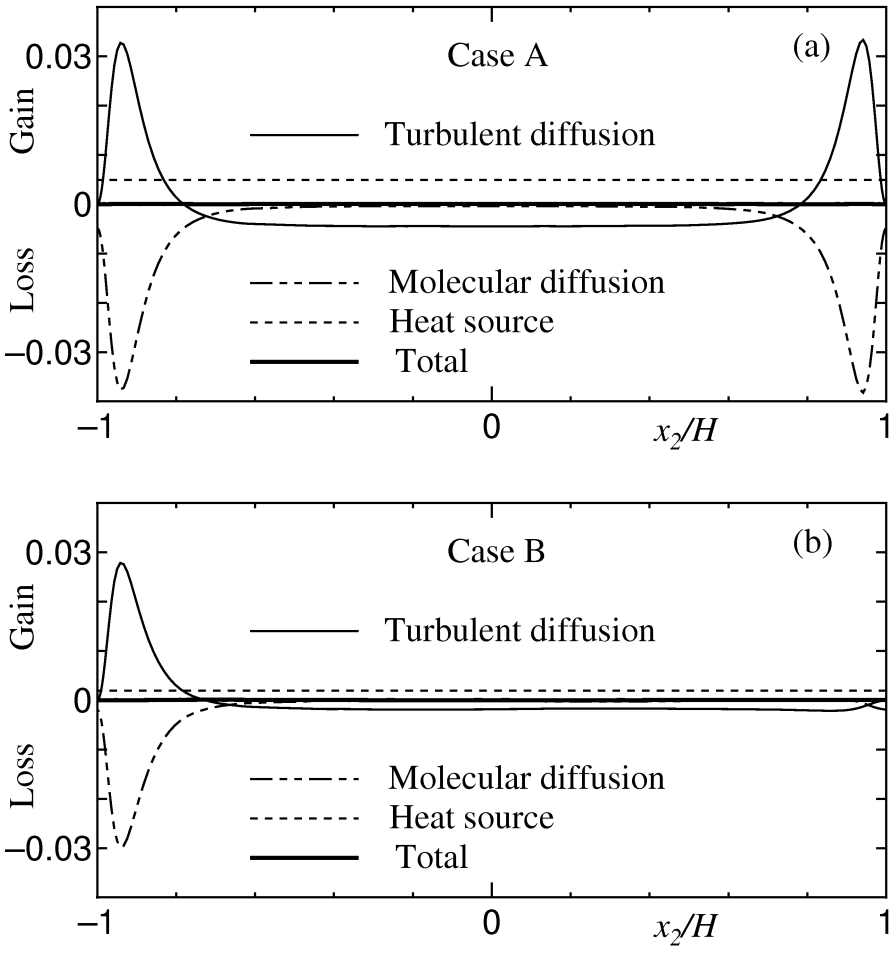

FIGURE 5.6. Internal energy budgets: (a) Case A and (b) Case B.

5.4 Compressibility Terms of Turbulent and Mean Kinetic Energy Budgets

The intrinsic compressibility term of the turbulent kinetic energy equation, C_k, is almost zero and has a slight value in the region very close to the wall (see figure 5.2). On the other hand, the intrinsic compressibility term of the mean kinetic energy equation, C_K, has a small value in the region very close to the wall (see figure 5.4). In the present simulations ($M = 1.5$), the result that C_k is almost zero is supported by the previous knowledge that the intrinsic compressibility effect like the pressure-dilatation correlation term is negligible for the wall-bounded compressible turbulent flow (e.g., Coleman *et al.* 1995; Huang *et al.* 1995; Guarini *et al.* 2000). Although some studies have been carried out to clarify the reason why the intrinsic compressibility effect is small near the wall (e.g. Sarkar 1995; Friedrich 1997), its detailed mechanism is still an open question. This is due to the lack of reliable DNS data for quantitative investigation. Therefore, we first clarify the dominant terms in C_k and C_K. Then the roles of these terms with respect to energy transfers are investigated.

Intrinsic compressibility terms of the turbulent kinetic energy equation are shown in figure 5.7. The pressure-dilatation correlation term C_{k3} (term 7 in figure 5.1) and the additional compressibility term C_{k1} (term 2 in figure 5.1) are almost zero near adiabatic and isothermal walls in compressible turbulent flow. The additional compressibility term C_{k2} (term 3 in figure 5.1) is dominant in C_k, and it has plus and minus values near isothermal and adiabatic walls, respectively. It implies that the term C_{k2} transfers the turbulent kinetic energy to the mean flow near the isothermal wall and transfers the energy from the mean flow to the turbulent flow near the adiabatic wall. This difference is explained as follows. The sign of C_{k2}, in which the term $\langle u_1'' \rangle \, \partial \langle \tau_{12} \rangle / \partial x_2$ is dominant, depends on that of $\langle u_1'' \rangle$, because $\partial \langle \tau_{12} \rangle / \partial x_2$ is always negative. The value of $\langle u_1'' \rangle$ is equal to $- \langle \rho' u_1' \rangle / \langle \rho \rangle$ (see (4.1)), which is positive and negative near isothermal and adiabatic walls, respectively. As a result, the value of C_{k2} is

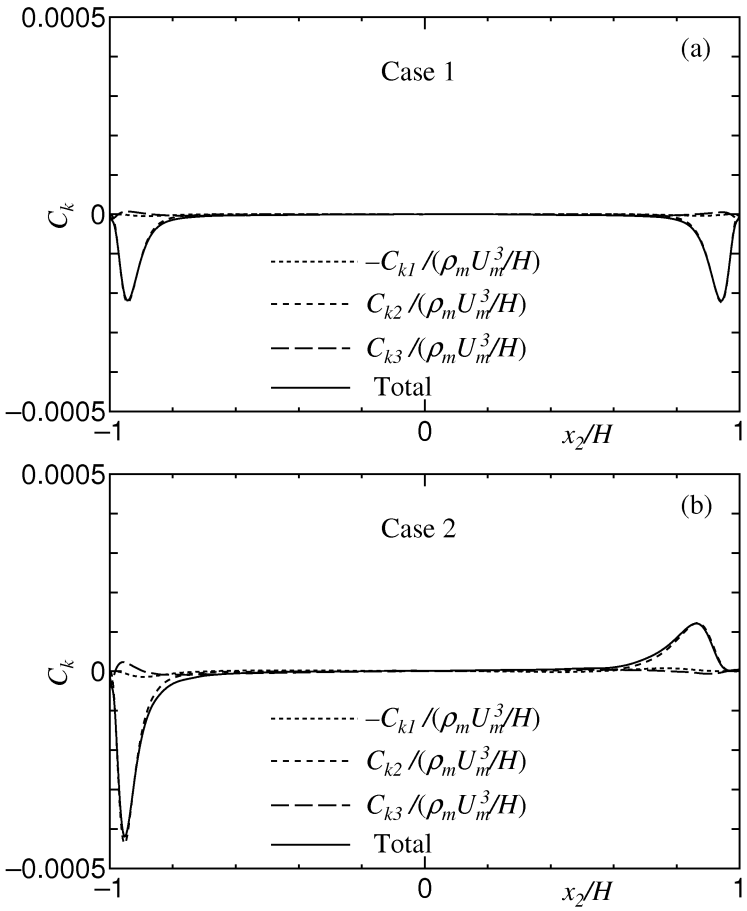

FIGURE 5.7. Intrinsic compressibility terms of turbulent kinetic energy equation: (a) Case 1 and (b) Case 2.

negative and positive near isothermal and adiabatic walls, respectively. Note that these energy transfers due to C_{k2} are small as mentioned above.

The intrinsic compressibility terms of the turbulent kinetic energy equation are shown in figure 5.8. The term relative to the pressure work (term 5 in figure 5.1), C_{K1}, is dominant in C_K, and it has minus and plus values near isothermal and adiabatic walls, respectively. It means that the term C_{K1} exchanges the internal energy for mean kinetic energy near the isothermal wall and exchanges the mean kinetic energy for internal energy near the adiabatic wall. This difference can be explained by the result that the value of the mean dilatation $\langle d \rangle$ is positive and negative near adiabatic and isothermal walls, respectively (see

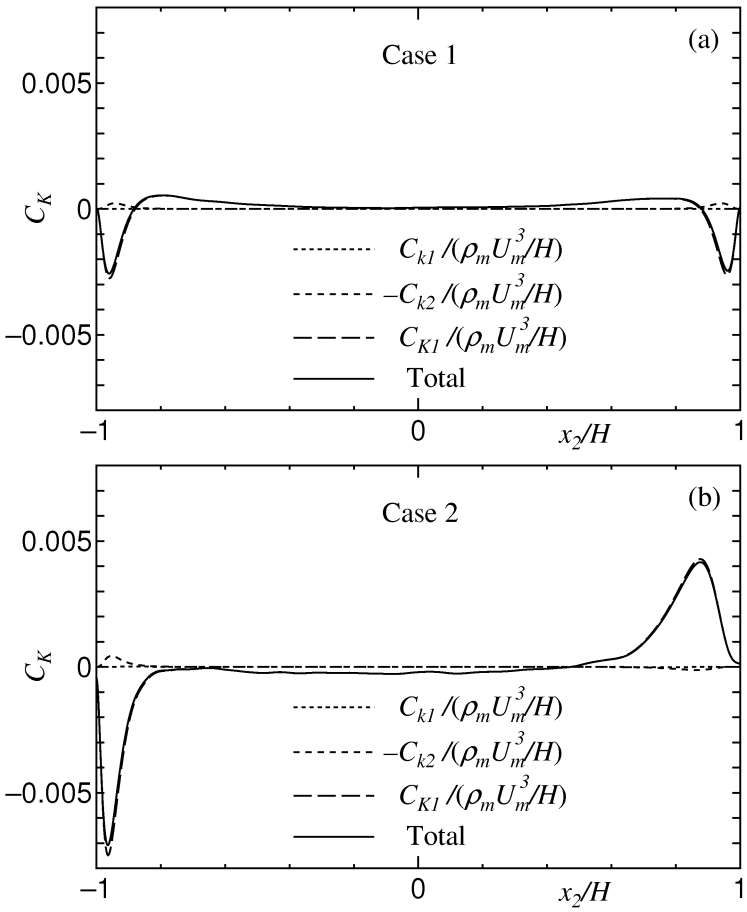

FIGURE 5.8. Intrinsic compressibility terms of mean kinetic energy equation: (a) Case 1 and (b) Case 2.

figure 5.9). Note that the negative and positive quantities represent the compression and expansion of the fluid, respectively.

5.5 Dissipation Terms of Turbulent and Mean Kinetic Energy Budgets

In this section, we consider the irreversible energy transfers due to the turbulent kinetic energy dissipation (see (5.13)), ε_k, and the mean kinetic energy dissipation (see (5.18)), ε_{VK}.

Using the vorticity fluctuation, $\omega_i' = \epsilon_{ijk}\partial u_k'/\partial x_j$, and (5.8), the dissipation

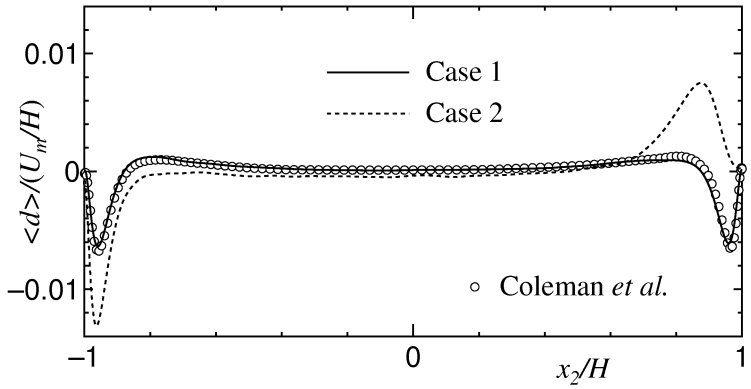

FIGURE 5.9. Mean dilatation terms for Cases 1 and 2.

of turbulent kinetic energy per unit volume, ε_k, is rewritten as follows.

$$\varepsilon_k = \langle\mu\rangle\langle\omega_i'\omega_i'\rangle - \frac{2}{3}\langle\mu\rangle\langle d'd'\rangle + \langle\mu'\omega_i'\omega_i'\rangle - \frac{2}{3}\langle\mu'd'd'\rangle + \frac{\partial\langle u_i\rangle}{\partial x_j}\left\langle\mu'\frac{\partial u_i'}{\partial x_j}\right\rangle + \frac{\partial\langle u_j\rangle}{\partial x_i}\left\langle\mu'\frac{\partial u_i'}{\partial x_j}\right\rangle - \frac{2}{3}\langle d\rangle\langle\mu'd'\rangle + 2\langle\mu\rangle\left\langle\frac{\partial u_i'}{\partial x_j}\frac{\partial u_j'}{\partial x_i}\right\rangle + 2\left\langle\mu'\frac{\partial u_i'}{\partial x_j}\frac{\partial u_j'}{\partial x_i}\right\rangle \quad (5.24)$$

The enstrophy dissipation term $\varepsilon_{k1} = \langle\mu\rangle\langle\omega_i'\omega_i'\rangle$, the dilatational dissipation term $\varepsilon_{k2} = -2/3\langle\mu\rangle\langle d'd'\rangle$, the thermodynamic dissipation term $\varepsilon_{k3} = \partial\langle u_i\rangle/\partial x_j \langle\mu'\partial u_i'/\partial x_j\rangle$, and the total dissipation per unit volume ε_k, are shown for Case 2 in figure 5.10. The value of ε_{k1} is dominant in the dissipation ε_k, the value of ε_{k2} is almost zero and the value of ε_{k3} is not negligible in the region very close to the isothermal wall. We confirmed that the other terms of (5.24) were negligible. The sum of the second and the eighth terms on the right-hand side of (5.24) is the dilatational dissipation for the homogenous compressible turbulent flow (see Sarkar 1991).

Using the following equation,

$$\omega_i'\omega_i' = \frac{\partial u_i'}{\partial x_j}\frac{\partial u_i'}{\partial x_j} - \frac{\partial u_i'}{\partial x_j}\frac{\partial u_j'}{\partial x_i}, \quad (5.25)$$

equation (5.24) is rewritten as follows.

$$\varepsilon_k = \langle\mu\rangle\left\langle\frac{\partial u_i'}{\partial x_j}\frac{\partial u_i'}{\partial x_j}\right\rangle - \frac{2}{3}\langle\mu\rangle\langle d'd'\rangle + \left\langle\mu'\frac{\partial u_i'}{\partial x_j}\frac{\partial u_i'}{\partial x_j}\right\rangle - \frac{2}{3}\langle\mu'd'd'\rangle + \frac{\partial\langle u_i\rangle}{\partial x_j}\left\langle\mu'\frac{\partial u_i'}{\partial x_j}\right\rangle + \frac{\partial\langle u_j\rangle}{\partial x_i}\left\langle\mu'\frac{\partial u_i'}{\partial x_j}\right\rangle - \frac{2}{3}\langle d\rangle\langle\mu'd'\rangle + \langle\mu\rangle\left\langle\frac{\partial u_i'}{\partial x_j}\frac{\partial u_j'}{\partial x_i}\right\rangle + \left\langle\mu'\frac{\partial u_i'}{\partial x_j}\frac{\partial u_j'}{\partial x_i}\right\rangle \quad (5.26)$$

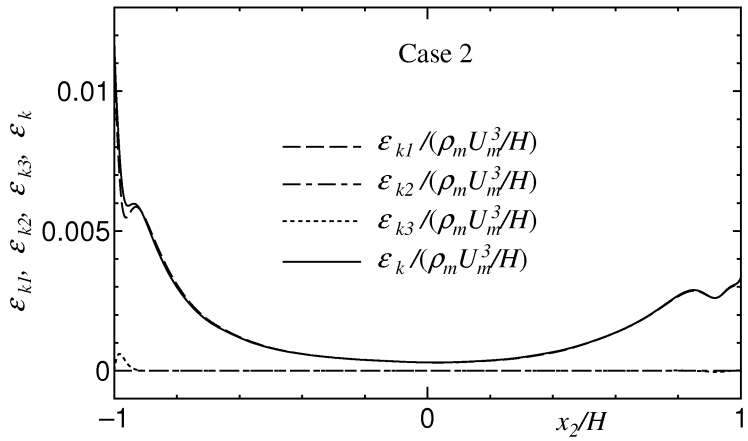

FIGURE 5.10. Turbulent kinetic energy dissipation per unit volume for Case 2.

The dissipation per unit mass, $\varepsilon_c = \varepsilon_k / \langle\rho\rangle$, is divided into the incompressible part, $\varepsilon_{ci} = (\langle\mu\rangle / \langle\rho\rangle) \langle(\partial u_i'/\partial x_j)^2\rangle$, and the compressible part, $\varepsilon_{cc} = \varepsilon_c - \varepsilon_{ci}$. The incompressible part $\langle\rho\rangle \varepsilon_{ci}$ and the compressible part $\langle\rho\rangle \varepsilon_{cc}$ correspond to terms 6ic and 6c, respectively. The dissipations per unit mass, ε_{ci}^*, ε_{cc}^* and ε_c^*, which are normalised by $u_{\tau *}$, $\langle\rho\rangle$ and $\langle\mu\rangle$, are shown for Cases 2IW and 2AW in figure 5.11. The compressible part ε_{cc}^* is not negligible near the isothermal wall, while it does not contribute near the adiabatic wall. Figures 5.10 and 5.11 indicate that the thermodynamic dissipation term is dominant in the compressible part of the turbulent energy dissipation and is not negligible in the region very close to the isothermal wall, i.e., it increases the internal energy. Figure 5.11 also shows that the scaling with the local variables collapses the dissipation ε_c^* onto the data of the incompressible turbulent flow. We confirmed that the dissipation scaled by the wall variables did not agree well with the data of the incompressible turbulent flow.

Next, we investigate the viscous dissipation per unit volume in the mean kinetic energy budget (see (5.18)), ε_{VK}, which is divided into the incompressible part (term 4ic in figure 5.1), $\varepsilon_{VKi} = \langle\mu\rangle (\partial \langle u_1\rangle / \partial x_2)^2$, and the compressible part (term 4c in figure 5.1), $\varepsilon_{VKc} = \varepsilon_{VK} - \varepsilon_{VKi}$. The viscous dissipations ε_{VK}, ε_{VKc} and ε_{VKi}, for Case 2 are shown in figure 5.12. The compressible part ε_{VKc} is almost

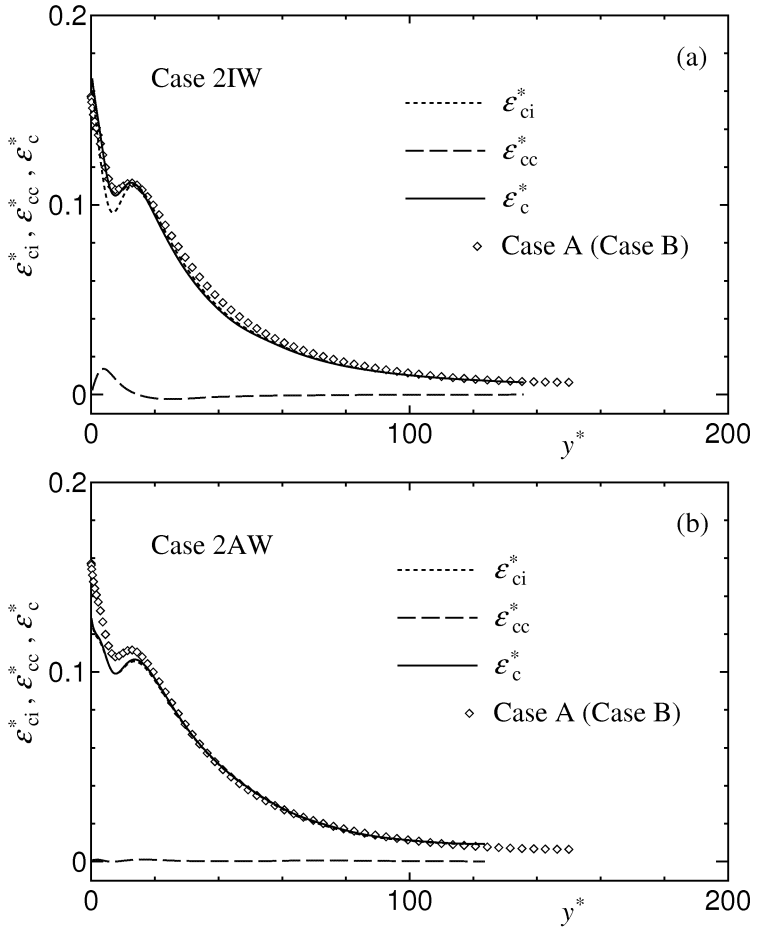

FIGURE 5.11. Turbulent kinetic energy dissipation per unit mass in semi-local wall units: (a) Case 2IW and (b) Case 2AW.

zero near adiabatic and isothermal walls for compressible turbulent flow, then we can ignore the energy transfer due to term 4c in figure 5.1.

5.6 Energy Transfers near Adiabatic and Isothermal walls

The energy transfers near isothermal and adiabatic walls are summarized for compressible turbulent flow as shown in figure 5.13. Term 1 is the energy transfer from the mean kinetic energy to the turbulent kinetic energy near adiabatic and isothermal walls in compressible turbulent flow. The roles of terms 2, 3, 5 and 7 with respect to intrinsic compressibility are as follows (see section 5.4). Terms 2

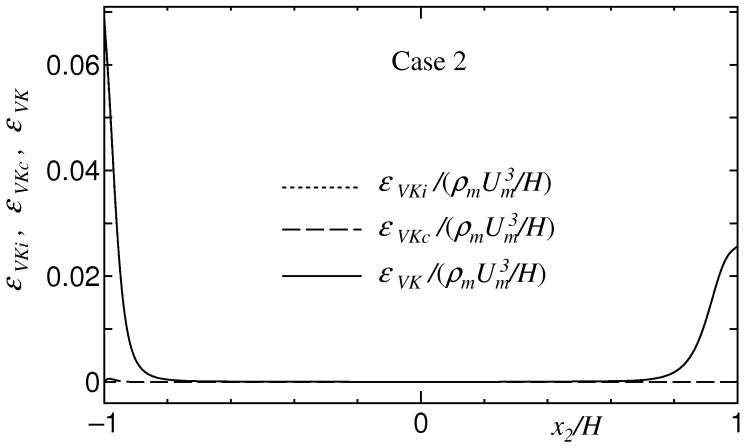

FIGURE 5.12. Mean kinetic energy dissipation per unit volume for Case 2.

and 7 do not contribute to energy transfers near isothermal and adiabatic walls in compressible turbulent flow. Term 3, which has a slight contribution to the energy transfer, transfers the turbulent kinetic energy to the mean flow near the isothermal wall and transfers the energy from the mean flow to the turbulent flow near the adiabatic wall. Term 5, which is a small contribution to the energy transfer, exchanges the internal energy for the mean kinetic energy near the isothermal wall and exchanges the mean kinetic energy for the internal energy near the adiabatic wall. The roles of terms 4 and 6 with respect to dissipations, ε_{VK} and ε_k, are as follows (see section 5.5). Most parts of the energy transfers due to terms 4 and 6 are composed of incompressible parts (terms 4ic and 6ic). The compressible part (term 6c) is not negligible close to the isothermal wall.

For the wall-bounded incompressible turbulent flows with passive scalar transport, the energy transfers due to terms 4ic and 6ic, which correspond to the incompressible parts of terms ε_{VK} and ε_k, do not exist. The only energy transfer due to term 1 exists in the wall-bounded incompressible turbulent flow, and its role is the same as that of the wall-bounded compressible turbulent flow.

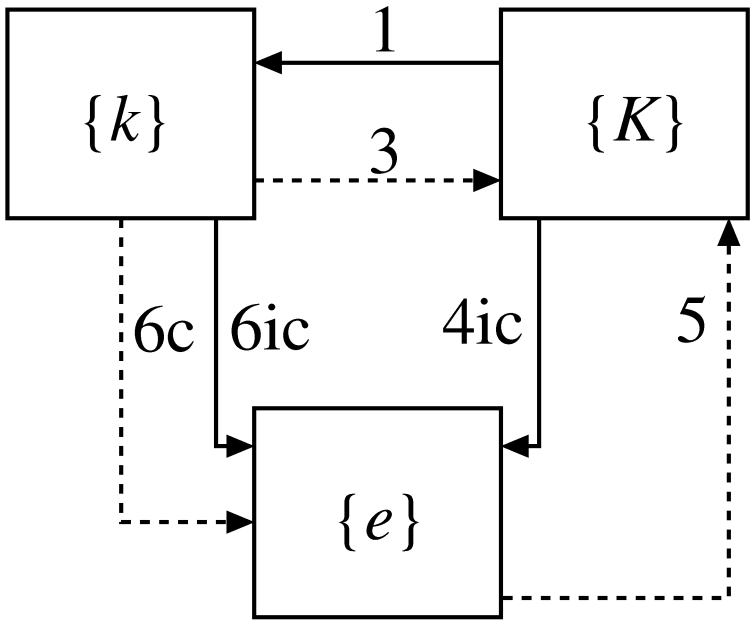

(a) near the isothermal wall (Case 1IW or 2IW)

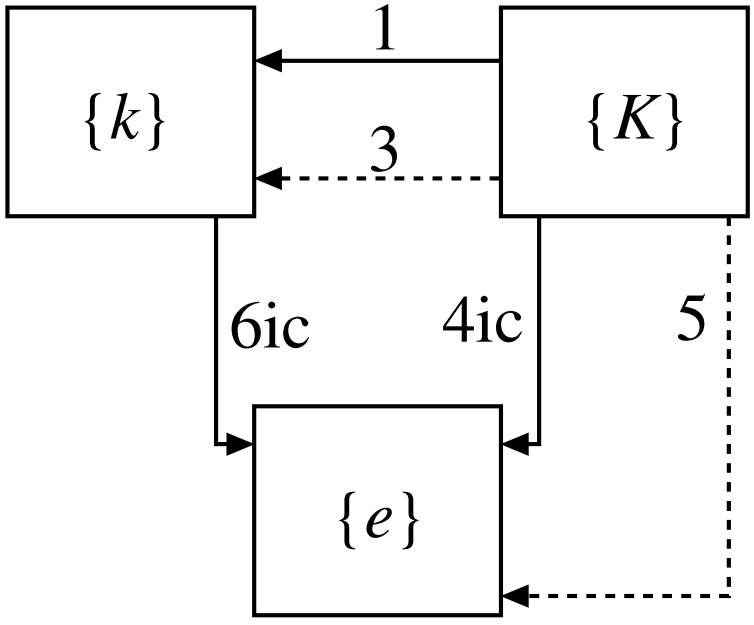

(b) near the adiabatic wall (Case 2AW)

FIGURE 5.13. Energy transfer of wall-bounded compressible turbulent flow: lines and numbers as figure 5.1.

5.7 Summary

In this chapter, the energy transfers near adiabatic and isothermal walls for the compressible turbulent flow are investigated. The results are summarized as follows.

(1) The additional compressibility term (term 3 in figure 5.1), C_{k2}, is dominant in the compressibility term C_k of the turbulent kinetic energy equation, although it has a slight contribution to the energy transfer. It transfers the turbulent kinetic energy to the mean flow near the isothermal wall and transfers the energy of the mean flow to the turbulent flow near the adiabatic wall. The direction of the energy transfer due to C_{k2} is determined by the sign of the correlation between density and streamwise velocity fluctuations. The pressure-dilatation correlation term is almost zero near adiabatic and isothermal walls for the compressible turbulent flow.

(2) The term relative to the pressure work (term 5 in figure 5.1), C_{K1}, is dominant in the compressibility term C_K of the mean kinetic energy equation. It exchanges internal energy for mean kinetic energy near the isothermal wall and exchanges mean kinetic energy for internal energy near the adiabatic wall. This difference can be explained by the result that the value of the mean dilatation $\langle d \rangle$ is positive and negative near adiabatic and isothermal walls, where the negative and positive values represent the compression and expansion of the fluid, respectively.

(3) Although the incompressible part of the turbulent energy dissipation is dominant, the compressible part is not negligible in the region very close to the isothermal wall. The thermodynamic dissipation term is dominant in the compressible part and increases the internal energy. On the other hand, the dilatational dissipation term is almost zero and does not depend on the thermal wall boundary condition. Note that the incompressible part dose not contribute the increase of the internal energy for incompressible turbulent flow. The energy transfer of the mean kinetic energy dissipation is mainly due to the incompressible

part, and that of the compressible part is negligible near isothermal and adiabatic walls in compressible turbulent flow.

Chapter 6.

Turbulence Structures

6.1 Outline

In this chapter, turbulence structures near isothermal and adiabatic walls are investigated for the compressible and incompressible turbulent flows. First, the velocity-streak structures on the (x_1–x_3)-plane normalized by the channel half-width are shown near adiabatic and isothermal walls for the compressible turbulent flow. Second, the semi-local viscous length scale is used. The streamwise and spanwise two-point correlations of streamwise velocity fluctuations are examined. Third, the temperature-streak structures near adiabatic and isothermal walls are investigated. Moreover, the correlation coefficient between streamwise velocity and temperature fluctuations is discussed in order to clarify the relationship between near-wall streak structures of velocity and temperature. Finally, the near-wall turbulence structures in the wall-normal direction are investigated for compressible and incompressible turbulent flows.

6.2 Near-wall Turbulence Structures

The near-wall streak structures have been investigated in the domain sizes normalized by channel half-width, H, or the viscous length scale, δ_v, in the previous studies. In this section, we introduce the semi-local length scale, δ_{v*}, to exclude Reynolds number effects due to the mean property variation. The values of the Reynolds number, Re_τ^*, and the computational domain sizes normalized

TABLE 6.1. Computational domain sizes normalized by semi-local viscous length.

Case	y/H	y^*	Re_τ^*	L_1^*	L_3^*
2IW	0.05	9.0	193	2425	808
2AW	0.13	12	94	1180	393
A (B)	0.08	11	150	1885	628

by semi-local viscous length, $L_1^* = L_1/\delta_{v*}$ and $L_3^* = L_3/\delta_{v*}$, at the wall-normal positions, y/H and y^*, where the near-wall streak structures are investigated, are summarized in table 6.1.

First, we investigate the near-wall streak structures on the (x_1–x_3)-plane normalized by the channel half-width. Figure 6.1 shows the contours of the streamwise velocity fluctuation on (x_1–x_3)-planes scaled by channel half-width for Cases 2AW and 2IW. The solid lines represent positive quantities which correspond to high-speed regions and the dashed lines represent negative quantities which correspond to low-speed streaks. The streak structures near the adiabatic wall are larger than those near the isothermal wall, when the normalization of the channel half-width is used.

Next, we investigate the near-wall streak structures in the computational domain sizes, L_1^* and L_3^*, in which those of Case 2AW are almost half those of Case 2IW (see table 6.1). Figure 6.2 shows the contours of the streamwise velocity fluctuation of Case 2AW on (x_1–x_3)-planes scaled by the semi-local viscous length of Case 2IW. Figures 6.1(b) and 6.2 show that the near-wall streak structures for Cases 2AW and 2IW are essentially comparable. Thus, the modification of the near-wall streak shown in figure 6.1 for the compressible turbulent flow is mainly due to the Reynolds number effect. This is confirmed by the two-point correlation of streamwise velocity fluctuation as described below.

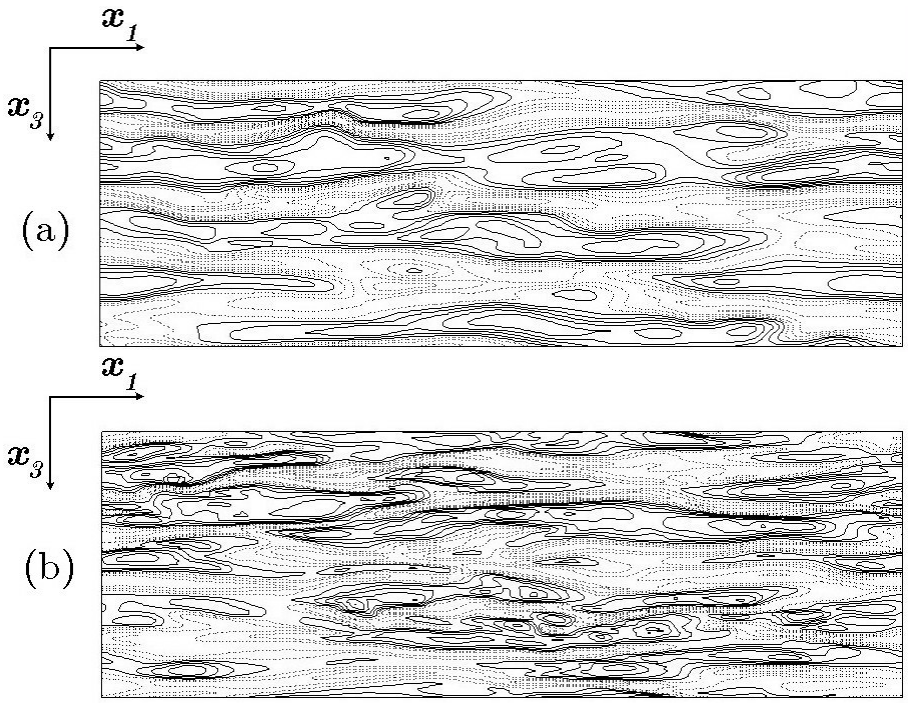

FIGURE 6.1. Contours of streamwise velocity fluctuation on (x_1–x_3)-planes scaled by channel half-width: (a) Case 2AW and (b) Case 2IW. Solid and dashed lines represent positive and negative quantities, respectively.

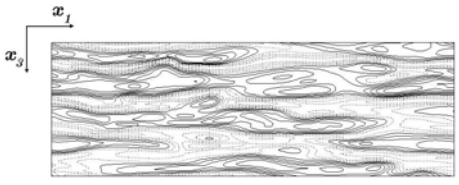

FIGURE 6.2. Contours of streamwise velocity fluctuation on (x_1–x_3)-planes scaled by semi-local viscous length for Case 2AW.

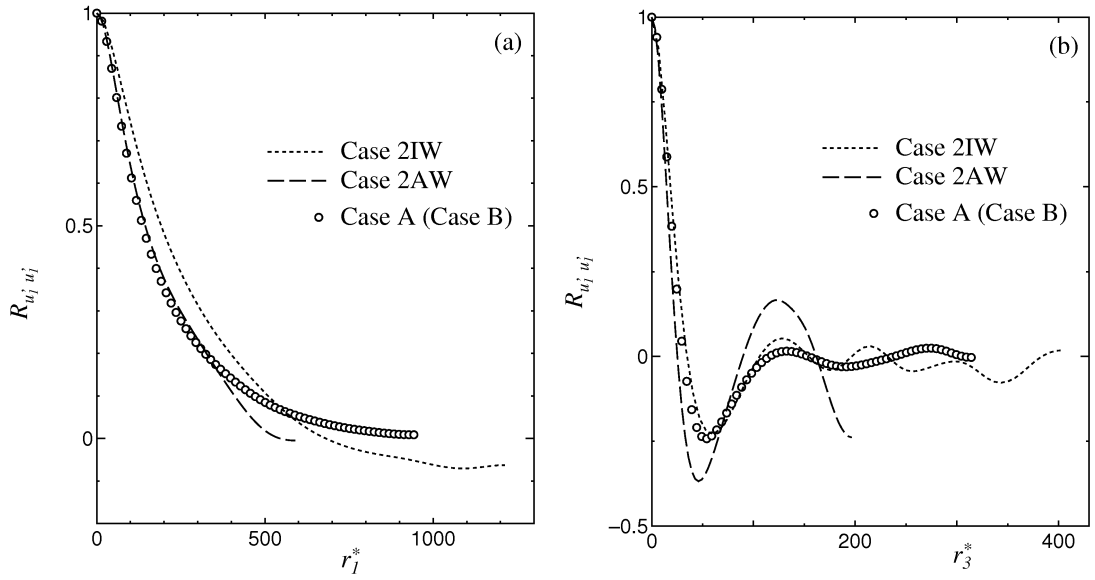

FIGURE 6.3. Two-point correlation of streamwise velocity fluctuation: (a) streamwise and (b) spanwise directions.

The streamwise and spanwise two-point correlations of streamwise velocity fluctuations, $R_{u_1' u_1'}(r_1)$ and $R_{u_1' u_1'}(r_3)$, are shown in figure 6.3. The two-point correlations are calculated at the same wall-normal positions shown in table 6.1, where r_1^* and r_3^* are defined as $r_1^* = r_1/\delta_{v*}$ and $r_3^* = r_3/\delta_{v*}$, respectively. The streamwise two-point correlations for compressible turbulent flow go to zero within $L_1^*/2$ and do not depend on the thermal wall boundary condition. It is found that the near-wall streaks of compressible turbulent flow do not become more coherent than those of incompressible turbulent flow. Hence, Morkovin's hypothesis is successful in the near-wall streak structures. Coleman *et al.* (1995) explained the modification of the streak using the ratio of turbulent and mean timescales used in the study of the homogeneous turbulent shear flow by Lee *et al.* (1990). However, we confirmed that the near-wall streak structures did not relate to the timescale ratio. To clarify the relationship between the streamwise two-point correlation and the near-wall streak structure, more detailed examination in terms of the variations in the time and space may be required. We

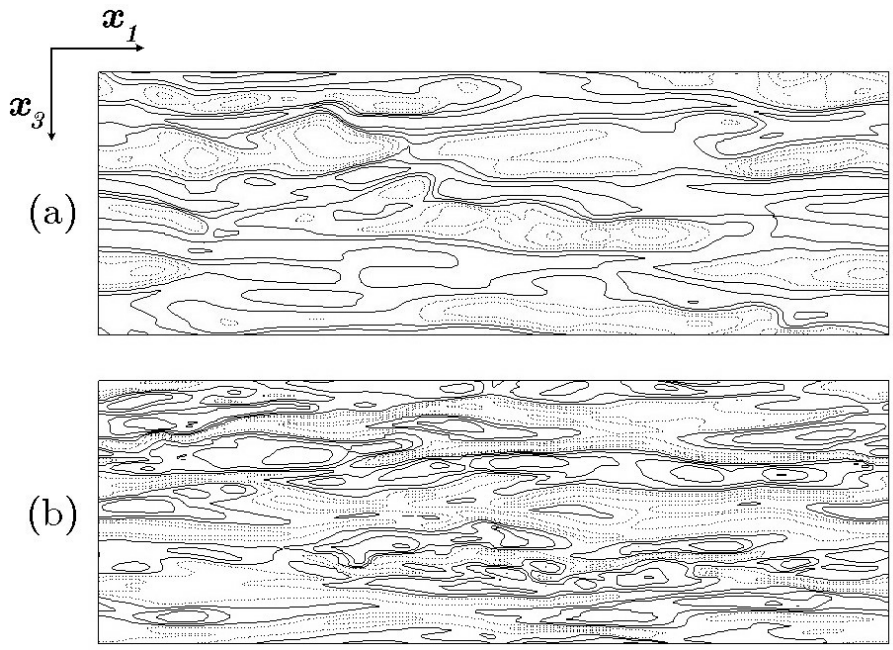

FIGURE 6.4. Contours of temperature fluctuation on (x_1–x_3)-planes scaled by channel half-width: (a) Case 2AW and (b) Case 2IW.

confirmed that the streamwise two-point correlations depended on the time and the wall-normal position for all cases in the present results. Smith & Metzler (1983) and Kim *et al.* (1987) reported experimentally and numerically that the near-wall streaks had a mean spacing of about 100 in wall units and increased with the distance from the wall for wall-bounded incompressible turbulent flow. Figure 6.3(b) shows that the streak spacing of compressible turbulent flow is about 100 in semi-local wall units and is almost the same as for incompressible turbulent flow. The dependence of the near-wall streaks on the Mach number will be considered in the near future.

Figure 6.4 shows the contours of the temperature fluctuation on (x_1–x_3)-planes scaled by channel half-width for Cases 2AW and 2IW. The solid and dashed lines represent high-temperature regions and low-temperature streaks, respectively. The comparison between figures 6.1 and 6.4 shows that the low-speed streaks coincide with the low-temperature streaks near the isothermal wall and exist in the high-temperature regions near the adiabatic wall for compressible

turbulent flow. This result is also explained by the correlation coefficient between streamwise velocity and temperature fluctuations as described later.

Figures 6.5 and 6.6 show the streak structures of velocity and temperature for Cases BAW and BIW, respectively. The low-speed streaks coincide with the low-temperature streaks near the isothermal wall for the incompressible turbulent flow. On the other hand, a corresponding relationship between streamwise velocity and temperature fluctuations is not observed near the adiabatic wall for incompressible turbulent flow, because the absolute values of temperature fluctuations near the adiabatic wall are very small. We confirmed that the production term in the equation of the temperature variance was almost zero near the adiabatic wall in incompressible flow.

To clarify the relationship between the near-wall streak structures of velocity and temperature, we investigate the correlation coefficient between streamwise velocity and temperature fluctuations, $R_{u_1'T'}$, which is defined by

$$R_{u_1'T'} = \frac{\langle u_1' T' \rangle}{\langle {u_1'}^2 \rangle^{1/2} \langle T'^2 \rangle^{1/2}}. \tag{6.1}$$

Guarini *et al.* (2000) reported that the velocity–temperature correlations agreed well with the experimental and computational data on incompressible boundary layer flows because of weak compressibility. On the other hand, Nicoud (1999) reported that the peak value of the absolute velocity–temperature correlation near a heated wall was larger than that of the correlation near a cold wall and larger than that of Kim & Moin for incompressible turbulent flow. The correlations $R_{u_1'T'}$ are shown for Cases 2 and B in figure 6.7. The present results on the velocity–temperature correlation in the region very close to the isothermal wall are almost unity, $R_{u_1'T'} \simeq 1.0$, for both compressible and incompressible turbulent flows, and their profiles are almost the same. The peak value of the absolute correlation near the adiabatic wall of Case 2 is approximately 0.9, which is smaller than that near the isothermal wall. On the other hand, the correlation $|R_{u_1'T'}|$ near the adiabatic wall for incompressible turbulent flow (Case B) is approximately 0.5–0.6 and is smaller than that for compressible turbulent flow (Case 2).

The difference between compressible and incompressible turbulent flows near the adiabatic wall is not attributable to the variable property effect. In other words, Morkovin's hypothesis is not applicable to the correlation coefficient between velocity and temperature fluctuations near the adiabatic wall.

Next, we investigate the near-wall turbulence structures in the wall-normal direction. Figures 6.8 and 6.9 show the contours of streamwise velocity and temperature fluctuations on (x_2–x_3)-planes for Cases 2 and B, respectively. Arrows indicate velocity vectors on the plane. The knowledge of the streak spacing and the correlation obtained in this section are also confirmed by figures 6.8 and 6.9. Lifting and bursting of the low-speed streaks, which are known in incompressible turbulent flow (see Robinson 1991), are also observed for compressible turbulent flow. In addition, it is found in the compressible turbulent flow that the oscillatory of the streak structures near the adiabatic wall is larger than that near the isothermal wall. This difference should be mainly due to the variable property effect.

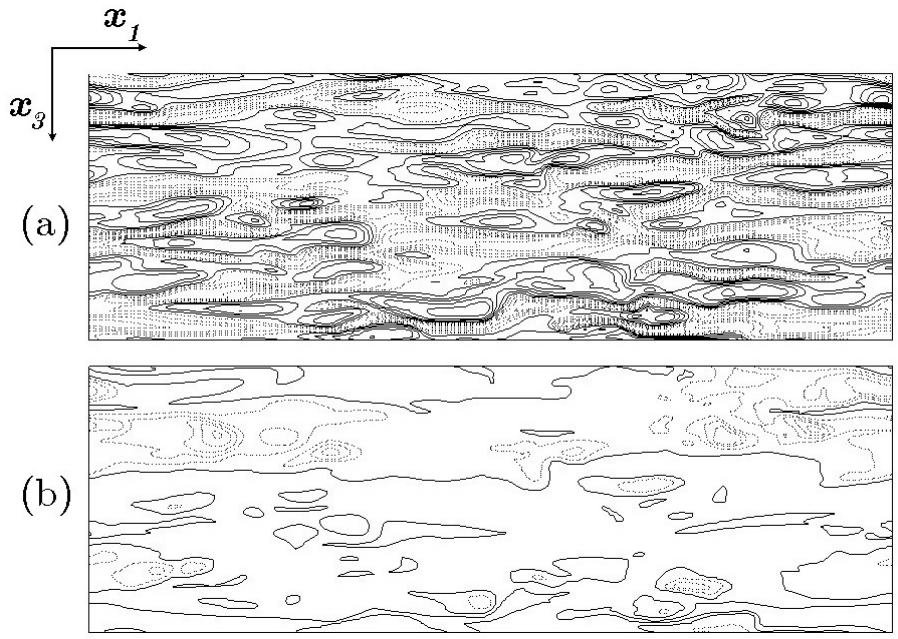

FIGURE 6.5. Contours on (x_1–x_3)-planes scaled by channel half-width for Case BAW: (a) streamwise velocity fluctuation and (b) temperature fluctuation.

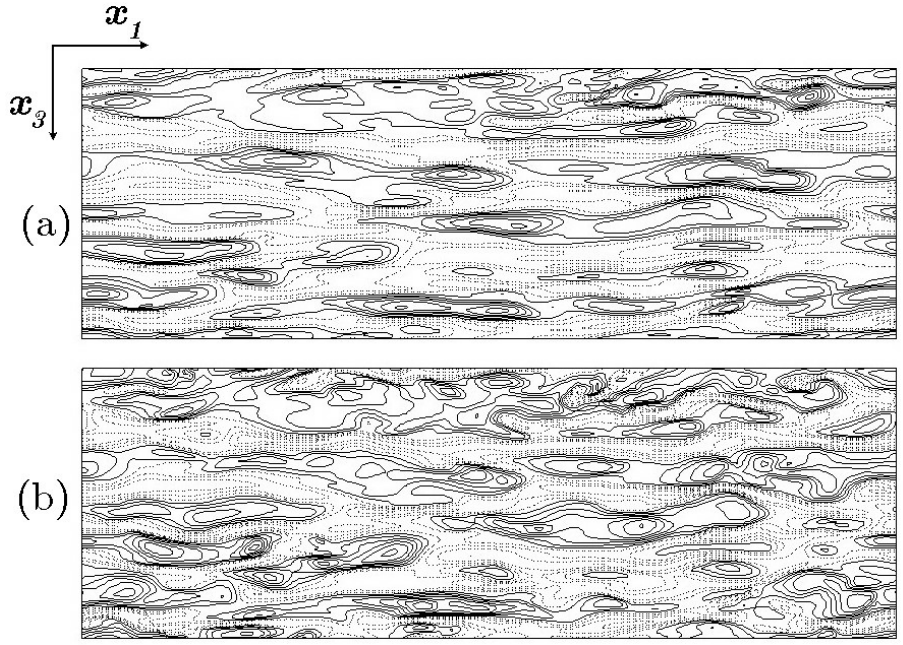

FIGURE 6.6. Contours on (x_1–x_3)-planes scaled by channel half-width for Case BIW: (a) streamwise velocity fluctuation and (b) temperature fluctuation.

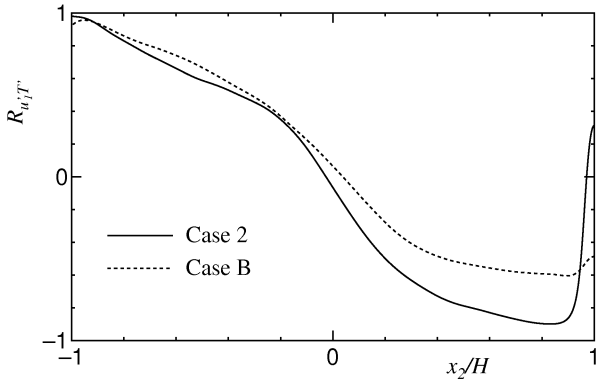

FIGURE 6.7. Correlation coefficients between u_1' and T' for Cases 2 and B.

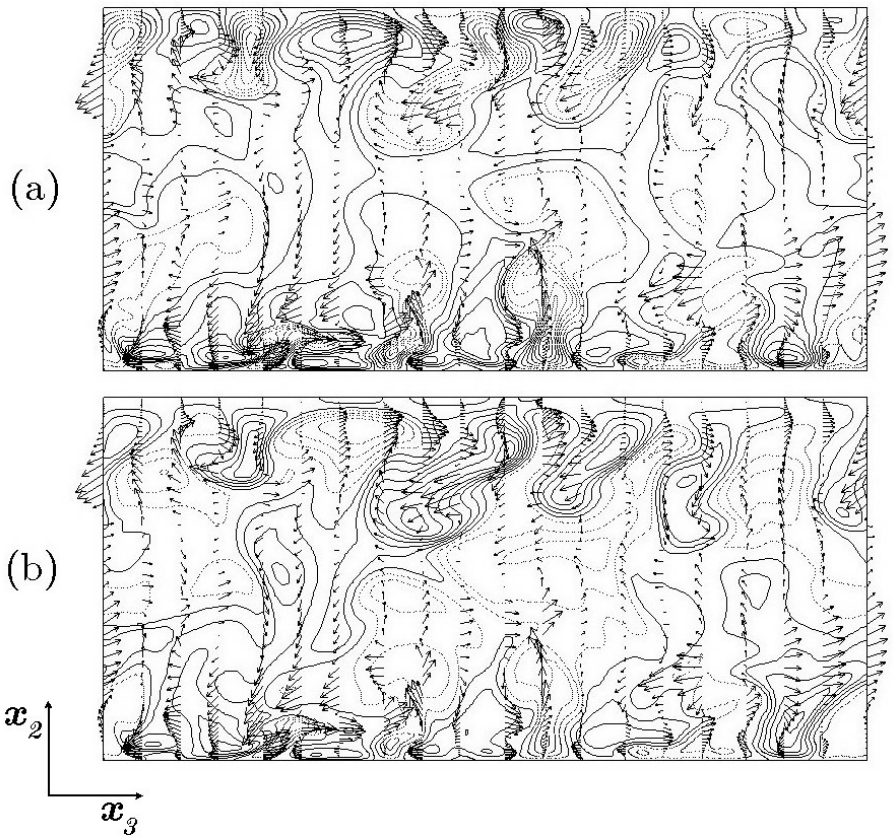

FIGURE 6.8. Contours on (x_2–x_3)-planes scaled by channel half-width for Case 2: (a) streamwise velocity fluctuations and (b) temperature fluctuations. Arrows indicate velocity vectors on the plane.

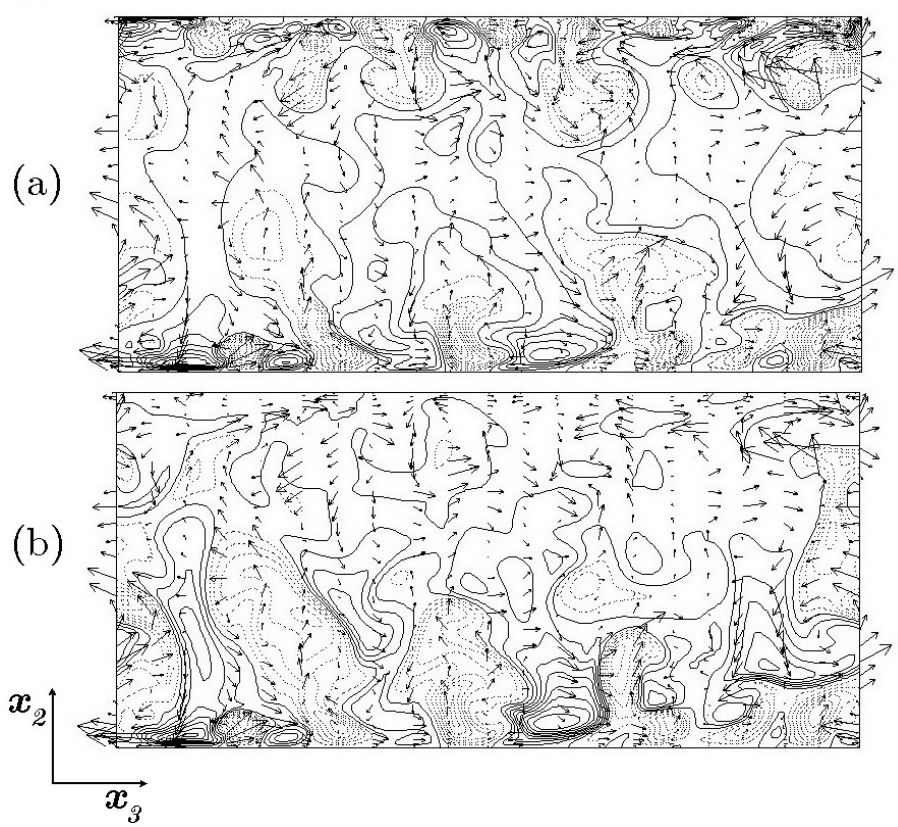

FIGURE 6.9. Contours on (x_2–x_3)-planes scaled by channel half-width for Case B: (a) streamwise velocity fluctuations and (b) temperature fluctuations.

6.3 Summary

In this chapter, the turbulence structures near adiabatic and isothermal walls for the compressible turbulent flow are investigated. The results are summarized as follows.

(1) The modification of the near-wall streak observed in the domain sizes normarized by the channel half-width for the compressible turbulent flow is mainly due to the variable property effect. This is also confirmed by the two-point correlation of streamwise velocity fluctuation. Thus, Morkovin's hypothesis is successful in the near-wall streak structures.

(2) The low-speed streaks coincide with the low-temperature streaks near the isothermal wall and exist in the high-temperature regions near the adiabatic wall

for the compressible turbulent flow. On the other hand, the low-speed streaks do not correspond to the high- or low-temperature region near the isothermal wall for the incompressible turbulent flow, while they coincide with the low-temperature streaks near the isothermal wall. This difference is confirmed by the correlation coefficient between velocity and temperature fluctuations and is not attributable to the variable property effect. In other words, Morkovin's hypothesis is not applicable to the correlation coefficient between velocity and temperature fluctuations near the adiabatic wall.

Chapter 7.

Conclusions

7.1 Summary of Results

The main results obtained in this study are presented as follows:

In Chapter 2, the new direct numerical simulation (DNS) algorithm which can simulate the compressible turbulent channel flow between adiabatic and isothermal walls accurately and efficiently is explained. The present DNS algorithm based on the B-spline collocation method has the following advantages. (1) The numerical boundary condition is uniquely and accurately determined corresponding to the physical boundary, in particular, at the adiabatic wall. (2) The construction of the algorithm is simple and the numerical cost is much cheaper than that of the B-spline Galerkin method. (3) The resolution at a high wave number is better than those of the central and Padé FDMs with the corresponding order. (4) The skew-symmetric form which is suitable for the wall-bounded compressible flow is used for the convection term to maintain numerical stability. The present skew-symmetric form works well even for simulations with poor grid resolutions. The reliability of the present DNS algorithm is confirmed by comparing our result with that of Coleman *et al.* (1995) for the compressible turbulent channel flow between isothermal walls. The applicability and usefulness of the present DNS algorithm is also confirmed by the stable implementation of DNS of the compressible turbulent channel flow between adiabatic and isothermal walls.

In Chapter 3, the mean velocity and temperature profiles are investigated

theoretically and numerically. The Van Driest transformed mean velocities near adiabatic and isothermal walls agree well with the data on incompressible turbulent flow. This can be explained by the theoretical analysis result, i.e., the Van Driest transformed velocity is independent of non-dimensional heat flux B_q and the friction Mach number M_τ, while the untransformed velocity increases with an increase of $-B_q$ and decreases with an increase of M_τ. The mean temperature profiles scaled by the wall and friction temperatures can be explained using the theoretical analysis result, i.e., the mean temperature increases with an increase of $-B_q$ and decreases with an increase of M_τ. And the difference of the mean temperature between compressible turbulent flows near isothermal and adiabatic walls is clarified. The logarithmic region of the mean temperature near the isothermal wall does not appear for compressible turbulent flow because of the effect of the viscous friction work, while the logarithmic region appears near the isothermal wall in incompressible turbulent flow.

In Chapter 4, turbulence statistics are discussed and the following conclusions are obtained. The velocity fluctuations normalized by the wall variables are larger and smaller near isothermal and adiabatic walls, respectively, compared with those of the incompressible turbulent channel flow. On the other hand, these profiles agree well with the data on incompressible turbulent channel flow, when such profiles are scaled by local mean variables. This means that Morkovin's hypothesis is applicable to velocity fluctuation profiles. The RMS temperature fluctuation profile scaled by the mean temperature is almost the same as that of the RMS density fluctuation profile scaled by the mean density, except that the RMS temperature fluctuation on the isothermal wall is zero. The wall variable scaling does not result in such a similarity between temperature and density fluctuations. The difference between Favre and Reynolds averages on the Reynolds shear stresses is negligible. The semi-local scaling provides universal profile of the Reynolds shear stress. On the other hand, the turbulent heat flux does not have a universal scaling in this study. The near-wall asymptotic behavior of the wall-normal RMS velocity fluctuation for the compressible turbulent flow is

not equal to that of the incompressible turbulent flow, even if the mean density variation is taken into account for the scaling. Thus, Morkovin's hypothesis is not applicable to near-wall asymptotic behavior. The existing modified Reynolds analogies do not agree well with the data on compressible turbulent flow between adiabatic and isothermal walls because of the influence of the opposite wall.

In Chapter 5, the mechanism of the energy transfer among the turbulent kinetic, mean kinetic and internal energies is investigated. Although the compressibility term C_k of the turbulent kinetic energy equation has a slight contribution to the energy transfer, the dominant term of C_k transfers the turbulent kinetic energy to the mean flow near the isothermal wall and transfers the energy of the mean flow to the turbulent flow near the adiabatic wall. This difference is due to the result that the correlation between the streamwise velocity and density fluctuations is positive and negative near isothermal and adiabatic walls. The pressure-dilatation correlation term is almost zero near adiabatic and isothermal walls in compressible turbulent flow. The term relative to the pressure work is dominant in the compressibility term C_K of the mean kinetic energy equation. It exchanges internal energy for mean kinetic energy near the isothermal wall and also exchanges mean kinetic energy for internal energy near the adiabatic wall. This difference can be explained by the result that the value of the mean dilatation is positive and negative near adiabatic and isothermal walls, where the negative and positive values represent the compression and expansion of the fluid, respectively. The compressible part of the turbulent energy dissipation is not negligible in the region very close to the isothermal wall, even if the incompressible part is dominant. It is found that the thermodynamic dissipation term is dominant in the compressible part and increases the internal energy. On the other hand, the dilatational dissipation near adiabatic and isothermal walls is almost zero. The energy transfer due to the mean kinetic energy dissipation is mainly composed of the incompressible part, and that of the compressible part is negligible in compressible turbulent flows near adiabatic and isothermal walls.

In Chapter 6, the near-wall streak structures of compressible and incom-

pressible turbulent flows are investigated. It is found that the near-wall streak structures of velocity are comparable and independent of the thermal wall boundary condition, when the variable property effect is taken into account. This is also confirmed by the two-point correlation of streamwise velocity fluctuation. Morkovin's hypothesis is thus successful in the near-wall streak structures. The low-speed streaks coincide with the low-temperature streaks near the isothermal wall and exist in the high-temperature regions near the adiabatic wall for compressible turbulent flow. On the other hand, the corresponding relationship between streamwise velocity and temperature fluctuations is not observed near the adiabatic wall for incompressible turbulent flow. This difference is confirmed by the correlation coefficient between velocity and temperature fluctuations, i.e., Morkovin's hypothesis is not applicable to the correlation coefficient between velocity and temperature fluctuations near the adiabatic wall.

7.2 Future Work

To make supersonic flight commercially attractive, the research to improve fuel efficiency, reduce pollution and minimize noise levels is required. Moreover, hypersonic flight will require the prediction of hypersonic combustion with sufficient accuracy. The following future works in terms of the wall-bounded compressible turbulent flow without strong discontinuities will be a key to meet these engineering challenges.

1. The Mach number chosen for the present supersonic simulation, $M = 1.5$, is in the middle of the region where Morkovin's hypothesis is applicable. The wall-bounded compressible turbulent flow at the Mach number range beyond $M = 5$ where Morkovin's hypothesis is not valid must be investigated.

2. The low Reynolds number, $Re = 3000$, is chosen in the present simulation because of the limitation of the computational resources. The simulation of the higher Reynolds number will be performed for understanding the

more practical compressible turbulent flow.

3. A reliable model, important from the viewpoint of practical demand, will be explored for wall-bounded compressible turbulent flow. Near-wall asymptotic behavior, variable property effect and so on will be taken into account in the turbulence model.

Appendix A.

Governing Equations

A.1 Compressible Flow

The continuity, momentum and energy equations are

$$\frac{\partial \rho}{\partial t} = -\frac{\partial(\rho u_j)}{\partial x_j}, \tag{A.1}$$

$$\frac{\partial u_i}{\partial t} = -u_j \frac{\partial u_i}{\partial x_j} - \frac{1}{\rho}\frac{\partial p}{\partial x_i} + \frac{1}{\rho}\frac{\partial \tau_{ij}}{\partial x_j} + f_i, \tag{A.2}$$

$$\frac{\partial T}{\partial t} = -u_j \frac{\partial T}{\partial x_j} + \frac{1}{\rho c_v}\left[-p\frac{\partial u_j}{\partial x_j} + \tau_{ij}\frac{\partial u_i}{\partial x_j} - \frac{\partial q_j}{\partial x_j}\right]. \tag{A.3}$$

The skew-symmetric forms for convection terms are used in (A.2) and (A.3). The viscous stress tensor τ_{ij} and the heat flux q_j are defined as

$$\tau_{ij} = \mu\left(\frac{\partial u_i}{\partial x_j} + \frac{\partial u_j}{\partial x_i}\right) - \frac{2}{3}\mu\frac{\partial u_k}{\partial x_k}\delta_{ij}, \tag{A.4}$$

$$q_j = -\kappa\frac{\partial T}{\partial x_j}. \tag{A.5}$$

The driving force f_i is given by

$$f_i = -\frac{\tau_{w_{av}}}{H\rho_m}\delta_{i1}, \tag{A.6}$$

where

$$\tau_{w_{av}} = \frac{\langle\tau_{12}\rangle_{x_1-x_3}\big|_{x_2=H} - \langle\tau_{12}\rangle_{x_1-x_3}\big|_{x_2=-H}}{2}. \tag{A.7}$$

Viscosity μ is given by Sutherland's law:

$$\frac{\mu}{\mu_{iw}} = \frac{1 + S_1/T_{iw}}{T/T_{iw} + S_1/T_{iw}}\left(\frac{T}{T_{iw}}\right)^{\frac{3}{2}}, \tag{A.8}$$

where S_1 is a constant. The state equation is

$$p = \frac{c_p\,(\gamma - 1)\,\rho T}{\gamma}. \tag{A.9}$$

A.2 Incompressible Flow

The continuity, Navior–Stokes and energy equations are

$$\frac{\partial u_j}{\partial x_j} = 0, \tag{A.10}$$

$$\frac{\partial u_i}{\partial t} + u_j \frac{\partial u_i}{\partial x_j} = -\frac{1}{\rho}\frac{\partial p}{\partial x_i} + \nu \frac{\partial^2 u_i}{\partial x_j \partial x_j}, \tag{A.11}$$

$$\frac{\partial T}{\partial t} + u_j \frac{\partial T}{\partial x_j} = -\frac{\kappa}{\rho c_p}\frac{\partial^2 T}{\partial x_j \partial x_j} + Q. \tag{A.12}$$

The heat source Q is given by

$$Q = -\frac{q_{w_{av}}}{\rho c_p H}, \tag{A.13}$$

where

$$q_{w_{av}} = \frac{\langle q_2 \rangle|_{x_2=H} - \langle q_2 \rangle|_{x_2=-H}}{2}. \tag{A.14}$$

Note that in the numerical simulation, the skew-symmetric forms for convection terms are used in (A.11) and (A.12) and the energy equation of scalar $\theta (= T_{iw} - T)$ is solved instead of (A.12).

Appendix B.

A Brief Description of B-spline

In the present Appendix we briefly introduce the B-spline function, the B-spline interpolation and the resolution of the B-spline collocation method. For further details of the B-spline method, see, for example, De Boor (1978) and Kravchenko & Moin (1998).

B.1 B-spline Properties

The B-spline is the piecewise polynomial function and is also a basic function of B-spline interpolation. The B-spline method has a high resolving power and makes it easy to treat the wall boundary condition, derivative and integration, and to change the order of B-spline. In this study, $B_j^k(x_2)$ $(j = 1, \cdots, N_2)$ is defined as follows. The B-spline of order zero is

$$B_j^0(x_2) = \begin{cases} 1 & q_{j-1} \leq x_2 < q_j \\ 0 & x_2 < q_{j-1},\ \ q_j \leq x_2. \end{cases} \tag{B.1}$$

The B-spline needs the knots points q_j $(j = -k, \cdots, N_2)$ in addition to the collocation points x_2^j $(j = 1, \cdots, N_2)$. The knots points should be satisfied by the Schoenberg–Whitney condition, and the virtual points are required for the wall boundary. In this study, all knots points [except the virtual one, q_j $(j = 1, \cdots, N_2 - k - 1)$] are defined for both uniform and non-uniform grids

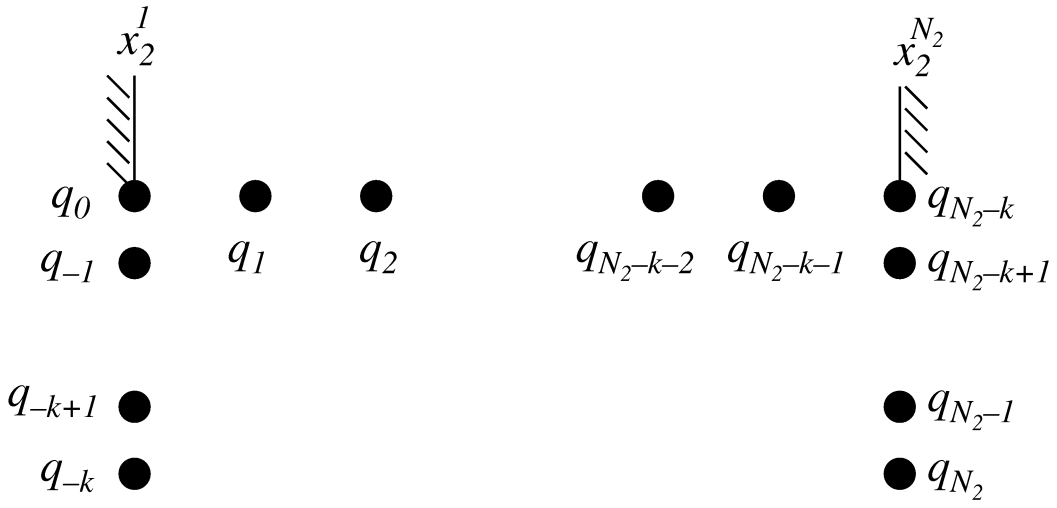

FIGURE B.1. Knot and virtual points.

as followings.

$$q_j = \begin{cases} (x_2^{j+k/2} + x_2^{j+k/2+1})/2 & (k : even) \\ x_2^{j+(k+1)/2} & (k : odd). \end{cases} \tag{B.2}$$

The configuration of the knots and virtual points is shown in figure B.1. There is an alternative method giving the relation between the knots and collocation points; the latter are given at the maximum of the B-spline (see Botella 2000). We attempted and confirmed for both configurations that their differences were negligible in the preset simulations. It is difficult to change the number and width of collocation points arbitrarily using the latter method. Therefore the relation of (B.2) is used in the present simulations.

The B-spline has the following important properties.

1. $B_j^k(x_2) = 0 \quad (x_2 < q_{j-k-1}, \quad x_2 > q_j)$
2. $B_j^k(x_2) > 0 \quad (q_{j-k-1} < x_2 < q_j \quad k \neq 0)$
3. $\sum_{j=1}^{s-r+k} B_{s+j-1}^k(x_2) = 1 \quad (q_r < x_2 < q_s, \quad k \leq r < s)$

The first and second properties represent the compact support of the B-spline. The third property guarantees the interpolation at the boundary. The B-spline

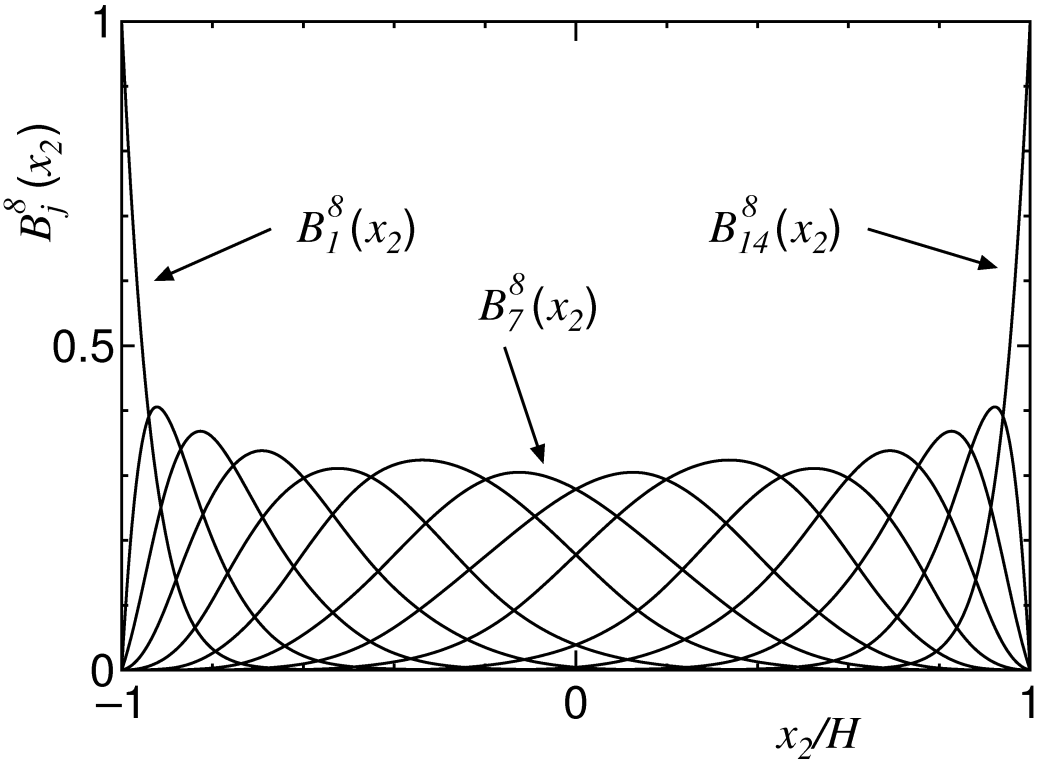

FIGURE B.2. B-splines of order 8 on non-uniform grids.

of order k , $B_j^k(x_2)$, is defined by the following recursive relation,

$$B_j^k(x_2) = \frac{(x_2 - q_{j-k-1})B_{j-1}^{k-1}(x_2)}{q_{j-1} - q_{j-k-1}} + \frac{(q_j - x_2)B_j^{k-1}(x_2)}{q_j - q_{j-k}}. \tag{B.3}$$

For instance, the profiles of $B_j^8(x_2)$ $(j = 1, \cdots, 14)$ on non-uniform grids are plotted in figure B.2. The grid points x_2^i $(i = 1, \cdots, 14)$ are given by the hyperbolic-tangent function (see figure B.2). The first derivative of $B_j^k(x_2)$,

$$\frac{dB_j^k(x_2)}{dx_2} = k\left[\frac{B_{j-1}^{k-1}(x_2)}{q_{j-1} - q_{j-k-1}} - \frac{B_j^{k-1}(x_2)}{q_j - q_{j-k}}\right], \tag{B.4}$$

is used for setting the adiabatic wall boundary condition.

B.2 Interpolation Based on B-spline

Define the interpolation function $\hat{\phi}(x_2)$ of the B-spline as,

$$\hat{\phi}(x_2) = \sum_{j=1}^{N_2} \phi_j^0 B_j^k(x_2), \tag{B.5}$$

where ϕ_j^0 is the expansion coefficient of the spline interpolation. The ℓ-th derivative of $\hat{\phi}(x_2)$ is

$$\frac{d^\ell \hat{\phi}(x_2)}{dx_2^\ell} = \sum_{j=1+\ell}^{N_2} \phi_j^\ell B_{j-\ell}^{k-\ell}(x_2), \tag{B.6}$$

where

$$\phi_j^\ell = (k-\ell+1)\frac{\phi_j^{\ell-1} - \phi_{j-1}^{\ell-1}}{q_{j-\ell} - q_{j-k-1}}. \tag{B.7}$$

On the other hand, the integration of $\hat{\phi}(x_2)$ is defined by the following equation.

$$\int_{-H}^{x_2} \hat{\phi}(x_2)dx_2 = \sum_{j=1}^{N_2} b_j B_j^k(x_2), \tag{B.8}$$

where

$$b_j = b_{j-1} + \phi_j^0 \frac{q_j - q_{j-k-1}}{k+1}, \quad (b_0 = 0). \tag{B.9}$$

B.3 Resolution of B-spline Collocation Method

The resolution of the B-spline collocation method is shown using the first derivative of the periodic function in the x_1 direction. The Fourier expansion of the function $\phi(x_1)$ is represented by

$$\phi\left(x_1\right) = \sum_{k_1=-N_1/2}^{N_1/2-1} \hat{\phi}_{k_1} e^{\mathrm{i}\alpha_{k_1}x_1}. \tag{B.10}$$

The first derivative in the x_1 direction is given by

$$\frac{d\phi\left(x_1\right)}{dx_1} = \sum_{k_1=-N_1/2}^{N_1/2-1} \mathrm{i}\alpha_{k_1}\hat{\phi}_{k_1} e^{\mathrm{i}\alpha_{k_1}x_1}. \tag{B.11}$$

When the discrete form of the first derivative is in general written by $\delta\phi/\delta x_1$, its Fourier expansion is represented as:

$$\frac{\delta\phi\left(x_1\right)}{\delta x_1} = \sum_{k_1=-N_1/2}^{N_1/2-1} \mathrm{i}\alpha'_{k_1}\hat{\phi}_{k_1} e^{\mathrm{i}\alpha_{k_1}x_1}, \tag{B.12}$$

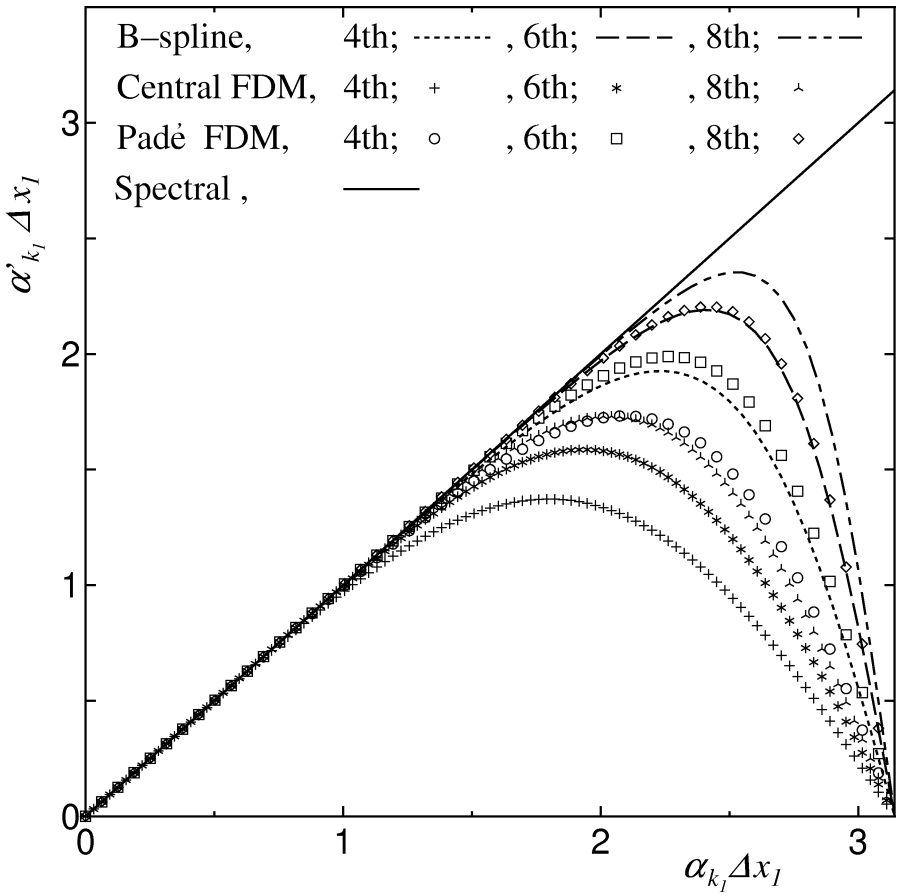

FIGURE B.3. Modified wave number of the first derivative with B-spline collocation method, central FDM and Padé FDM.

where α'_{k_1} is the modified wave number of the fisrt derivative. The modified wave numbers on uniform grids for the B-spline collocation method, central FDM and Padé FDM (see Lele 1992) are plotted in figure B.3. The periodic B-spline function is used to calculate that number for the B-spline collocation method. Figure B.3 shows that the resolution of the B-spline collocation method at the high wave number is better than those of the central and Padé FDMs with the corresponding order. In this study, the eighth order B-spline collocation method is used, and its resolution suffices for about 2/3 of the wave number.

References

Adams, N. A. & Shariff, K. 1996 A high-resolution hybrid compact-ENO scheme for shock-turbulence interaction problems. *J. Comput. Phys.* **127**, 27–51.

Adams, N. A. 2000 Direct simulation of the turbulent boundary layer along a compression ramp at $M = 3$ and $Re_\theta = 1685$. *J. Fluid Mech.* **420**, 47–83.

Antonia, R. A., Teitel, M., Kim, J. & Browne, L. W. 1992 Low-Reynolds-number effects in a fully developed turbulent channel flow. *J. Fluid Mech.* **236**, 579–605.

Blaisdell, G. A., Mansour, N.N. & Reynolds, W. C. 1993 Compressibility effects on the growth and structure of homogeneous turbulent shear flow. *J. Fluid Mech.* **256**, 443–485.

Blaisdell, G. A. & Spyropoulos, J. H. 1996 The effect of the formulation of nonlinear terms on aliasing errors in spectral methods. *Appl. Numer. Math.* **21** (3), 207–219.

Botella, O. 2000 A velocity-pressure Navier-Stokes solver using a B-spline collocation method. *CTR Annual Research Briefs - 1999, Stanford Univ./NASA Ames*, 403–421.

Botella, O. 2001 A high-order approximate-mass spline collocation scheme for incompressible flow simulations. *CTR Annual Research Briefs - 2000, Stanford Univ./NASA Ames*, 159–177.

Bradshaw, P. 1977 Compressible turbulent shear layers. *Ann. Rev. Fluid Mech.* **9**, 33–54.

Buell, J. C. 1990 Direct simulations of wall-bounded compressible tur-

bulence. *CTR Annual Research Briefs - 1989, Stanford Univ./NASA Ames*, 169–173.

Buell, J. C. 1991 Direct simulations of compressible wall-bounded turbulence. *CTR Annual Research Briefs - 1990, Stanford Univ./NASA Ames*, 347–356.

Canuto, C., Hussaini, M., Quarteroni, A. & Zang, T 1988 Spectral methods in fluid dynamics. *Springer, Berlin.*

Coleman, G. N., Kim, J. & Moser, R. D. 1995 A numerical study of turbulent supersonic isothermal-wall channel flow. *J. Fluid Mech.* **305**, 159–183.

De Boor, C. 1978 A practical guide to splines. *Springer, Berlin.*

Dailey, L. D. & Pletcher, R. H. 1999 Large eddy simulation of constant heat flux turbulent channel flow with property variations *AIAA Paper 98-0791.*

Fernholz, H. H. & Finley, P. J. 1977 A critical complication of compressible turbulent boundary layer data. *AGARD-AG* **223**.

Fernholz, H. H. & Finley, P. J. 1980 A critical commentary on mean flow data for two-dimensional compressible turbulent boundary layers. *AGARD-AG* **253**.

Friedrich, R. & Bertolotti, F. P. 1997 Compressibility effects due to turbulent fluctuations. *Appl. Sci. Res.* **57**, 165–194.

Gaviglio, J. 1987 Reynolds analogies and experimental study of heat transfer in the supersonic boundary layer. *Int. J. Heat Mass Transfer* **30** (5), 911–926.

Guarini, S. E. 1998 Direct numerical simulation of supersonic turbulent boundary layers. *PhD thesis*, Stanford University.

Guarini, S. E., Moser, R. D., Shariff, K. & Wray, A. 2000 Direct numerical simulation of a supersonic turbulent boundary layer at Mach 2.5. *J. Fluid Mech.* **414**, 1–33.

Guo, Y. & Adams, N. A. 1995 Numerical investigation of supersonic turbulent boundary layers with high wall temperature. *Proc. 5th Summer Prog. -1994, NASA/Stanford Center for Turbulence Research*, 245–267.

Horiuti, K. 1992 Assessment of two-equation models of turbulent passive-

scalar diffusion in channel flow. *J. Fluid Mech.* **238**, 405–433.

Huang, P. G., Bradshaw, P. & Coakley, T. J. 1994 Turbulence models for compressible boundary layers. *AIAA J.* **32** (4), 735–740.

Huang, P. G. & Coleman, G. N. 1994 Van Driest transformation and compressible wall-bounded flows. *AIAA J.* **32** (10), 2110–2113.

Huang, P. G., Coleman, G. N. & Bradshaw, P. 1995 Compressible turbulent channel flows: DNS results and modelling. *J. Fluid Mech.* **305**, 185–218.

Kim, J., Moin, P. & Moser, R. 1987 Turbulence statistics in fully developed channel flow at low Reynolds number. *J. Fluid Mech.* **177**, 133–166.

Kim, J. & Moin, P. 1989 Transport of passive scalars in a turbulent channel flow. *Turbulent Shear Flows* **6**, Springer, Berlin, 85–96.

Kleiser, L. & Schumann, U. 1980 Treatment of incompressibility and boundary conditions in 3-D numerical spectral simulations of plane channel flows. *Proc. 3rd GAMM Conference on Numerical Methods in Fluid Mechanics, edited by E. H. Hirschel*, Vieweg, Brauschweig, 165–173.

Kravchenko, A. G., Moin, P. & Moser, R. D. 1996 Zonal embedded grids for numerical simulations of wall-bounded turbulent flows. *J. Fluid Mech.* **127**, 412–423.

Kravchenko, A. G. & Moin, P. 1997 On the effect of numerical errors in large eddy simulations of turbulent flows. *J. Comput. Phys.* **131**, 310–322.

Kravchenko, A. G. & Moin, P. 1998 B-spline method and zonal grids for numerical simulations of turbulent flows. *Report TF-73, Dept. of Mech. Eng.*, Stanford University.

Kravchenko, A. G., Moin, P. & Shariff, K. 1999 B-spline method and zonal grids for simulations of complex turbulent flows. *J. Comput. Phys.* **151**, 757–789.

Lechner, R., Sesterhenn, J. & Friedrich, R. 2001 Turbulent supersonic channel flow. *J. Turbulence* **2**, 1–25.

Lee, M. J., Kim, J. & Moser, P. 1990 Structure of turbulence at high

shear rate. *J. Fluid Mech.* **216**, 561–583.

LELE, S. K. 1992 Compact finite difference schemes with spectral-like resolution. *J. Comput. Phys.* **103**, 16–42.

LELE, S. K. 1994 Compressibility effects on turbulence. *Ann. Rev. Fluid Mech.* **26**, 211–254.

LOULOU, P., MOSER, R. D., MANSOUR, N. N. & CANTWELL, B. J. 1997 Direct numerical simulation of incompressible pipe flow using a B-spline spectral method. *NASA-Ames Research Center, Moffett Field, CA 94035-1000.*

LENORMAND, E., SAGAUT, P. & TA PHUOC, L. 2000 Large eddy simulation of subsonic and supersonic channel flow at moderate Reynolds number. *Int. J. Numer. Meth. Fluids* **32**, 369–406.

MAEDER, T., ADAMS, N. A. & KLEISER, L. 2001 Direct simulation of turbulent supersonic boundary layers by an extended temporal approach. *J. Fluid Mech.* **429**, 187–216.

MORINISHI, Y., LUND, T., VASILYEV, O. & MOIN, P. 1998 Fully conservative higher order finite difference schemes for incompressible Flow. *J. Comput. Phys.* **143**, 90–124.

MORINISHI, Y., TAMANO, S. & NAKABAYASHI, K. 2001*a* A DNS algorithm using B-spline collocation method for compressible turbulent channel flow. Submitted to *Computers & Fluids.*

MORINISHI, Y., TAMANO, S. & NAKABAYASHI, K. 2001*b* DNS of compressible turbulent channel flow between adiabatic and isothermal walls. Submitted to *J. Fluid Mech.*

MORKOVIN, M. V. 1962 Effects of compressibility on turbulent flows. In *Mécanique de la Turbulence* (ed. A. Favre) CNRS, 367–380.

NICOUD, F. C. 1999 Numerical study of a channel flow with variable properties. *CTR Annual Research Briefs - 1998, Stanford Univ./NASA Ames*, 289–310.

ROBINSON, S. K. 1991 Coherent motions in the turbulent boundary layer *Annu. Rev. Fluid Mech.*, **23**, 601–639.

RUBESIN, M. W. 1990 Extra compressibility terms for Favre-averaged two-

equation models of inhomogeneous turbulent flows. *NASA Contractor Report 177556.*

Sarkar, S., Erlebacher, G., Hussaini, M. Y. & Kreiss, H. O. 1991 The analysis and modelling of dilatational terms in compressible turbulence. *J. Fluid Mech.* **227**, 473–493.

Sarkar, S. 1995 The stabilizing effect of compressibility in turbulent shear flow. *J. Fluid Mech.* **282**, 163–186.

Smith, C. R. & Metzler, S. P. 1983 The characteristics of low-speed streaks in the near-wall region of a turbulent boundary layer. *J. Fluid Mech.* **129**, 27–54.

Smits, A. J. & Dussauge, J. P. 1996 Turbulent Shear Layers in Supersonic Flow. *American Institute of Physics.*

So, R. M. C., Gatski, T. B. & Sommer, T. P. 1998 Morkovin hypothesis and the modeling of wall-bounded compressible turbulent flows. *AIAA J.* **36** (9), 1583–1592.

Spalart, P. R., Moser, R. D. & Rogers, M. M. 1991 Spectral methods for the Navier-Stokes equations with one infinite and two periodic directions. *J. Comput. Phys.* **96**, 297–324.

Spalding, D. B. 1961 On similarity solutions for free-convection flow past flat plates. *J. Applied Mech.* **23**, 455–458.

Spina, E. F., Smits, A. J. & Robinson, S. K. 1994 The physics of supersonic turbulent boundary layers. *Ann. Rev. Fluid Mech.* **26**, 287–319.

Teitel, M. & Antonia, R. A. 1993 Heat transfer in fully developed turbulent channel flow: comparison between experiment and direct numerical simulations. *Int. J. Heat Mass Transfer* **36** (6), 1701–1706.

Van Driest, E. R. 1951 Turbulent boundary layer in compressible fluids. *J. Aero. Sci.* **18** (3), 145–160.

Wang, W. P. & Pletcher, R. H. 1996 On the large eddy simulation of a turbulent channel flow with significant heat transfer. *Phys. Fluids* **8** (12), 3354–3366.

WERNE, J. 1995 Incompressibility and no-slip boundaries in the Chebyshev-tau approximation: Correction to Kleiserand Schumann's influence-matrix solution. *J. Comput. Phys.* **120**, 260–265

WHITE, F. M. 1991 Viscous fluid flow, 2nd ed., *McGraw-Hill, Inc.*

WRAY, A. A. 1986 Minimal storage time-advancement schemes for spectral methods. *NASA-Ames Research Center, Moffett Field, CA, Private Communication*

ZHANG, H. S., SO, R. M. C., SPEZIALE, C. G. & LAI, Y. G. 1993 Near-wall two-equation model for compressible turbulent flows. *AIAA J.* **31** (1), 196–199.